Applications of the random-state approach to quantum many-body dynamics

Zhao, Peiliang

Applications of the random-state approach to quantum many-body dynamics

Peiliang Zhao

PhD thesis
University of Groningen
The Netherlands

The work described in this thesis was performed in the Computational Physics group (part of the Zernike Institute of Advanced Materials) of the Rijksuniversiteit Groningen, The Netherlands. This research was mainly funded by the China Scholarship Council (Grant No. 201306890009).

Zernike Institute for Advanced Materials PhD thesis series 2017-13
ISSN: 1570-1530
ISBN: 978-90-367-9837-2 (electronic version)
ISBN: 978-90-367-9838-9 (printed version)

Cover design by Peiliang Zhao & Guus Slotman
Printed by PrintPartners Ipskamp, the Netherlands

university of groningen / faculty of science and engineering / zernike institute for advanced materials

university of groningen

Applications of the random-state approach to quantum many-body dynamics

PhD thesis

to obtain the degree of PhD at the
University of Groningen
on the authority of the
Rector Magnificus Prof. E. Sterken
and in accordance with
the decision by the College of Deans.

This thesis will be defended in public on

Friday 8 September 2017 at 11 : 00 hours

by

Peiliang Zhao

born on 20 August 1986
in Henan, China

Supervisor

Prof. H.A. De Raedt

Co-supervisor

Prof. P. Rudolf

Assessment committee

Prof. M. A. Novotny

Prof. J.Th.M. De Hosson

Prof. R.G.E. Timmermans

To my family

Contents

Chapter 1

Introduction

1.1 Motivation

This thesis focuses on numerical algorithms for solving the time-dependent Schrödinger equation of many-body quantum systems in combination with random state approach and on the applications of these algorithms to the study of transport properties of graphene with different types of disorders and the quantum dynamics of one spin-1/2 particle coupled to a thermal bath of spins-1/2 particles.

In the first application we address the question of the dominant source of disorder which limits the transport and optical properties of graphene, an issue that is still under debate. Different mechanisms have been proposed and investigated intensively, including charged impurities, random strain fluctuations and resonant scatterers (for reviews see Refs. [1, 2]). However, this mechanism does not explain the experimental observations well. Besides the transport properties, an important part of our knowledge about the electronic properties derives from the optical spectroscopy measurements [1, 3]. There are experimentally observed background contributions to the graphene optical spectroscopy for frequencies smaller than two times the chemical

potential [4, 5], which are due to the extra intraband excitations introduced by disorder or many-body effects [4, 6–16], opening up the possibility to identify the source of disorder via the optical measurements and to compare these experimental results with model calculations such as the ones presented in this thesis.

To illustrate the versatility of the simulation approach adopted in this thesis, our second application is very different from the first one and focuses on the dynamics of open quantum systems. Specifically, we study the quantum dynamics of a magnetic particle, represented by a spin-1/2 object, interacting with a heat bath via magnetic interactions. System-bath models are relevant for the description of relaxation processes in nuclear magnetic and electron spin resonance [17–19] but have also applications to, e.g. the field of quantum information processing, as most of the models used in this field are formulated in terms of qubits (spin-1/2 objects) [20, 21]. The aim of this part of the thesis work is to present a quantitative assessment of the quantum master equation approach by comparing the results with those obtained by an approximation-free, numerical solution of the time-dependent Schrödinger equation of the whole system.

1.2 Background

The *Liouville-von Neumann equation* is the basic framework unifying the quantum mechanical and statistical descriptions of matter. This framework permits a consistent treatment of the transition between pure state and mixture that is central in the description of the quantum mechanical measurement process and in the relaxation of a system to thermal equilibrium. In quantum statistical mechanics, the state of an ensemble of identical subsystems is completely specified by the density matrix $\hat{\rho}$, and expectation values of an observable are fully determined by the relation $\langle \hat{A} \rangle = \mathrm{Tr}\big[\hat{\rho}(t)\hat{A}\big]$. The latter expression is a pillar of the axiomatic description of quantum mechanics and the interpretation of measurements on quantum mechanical systems. The density matrix has also been extensively used in solid state physics, both for equilibrium and transport problems. The diamagnetism of many-electron systems, such as conducting or semiconducting solids, is a typical example of such an equilibrium problem. The study of transports processes, such as electrical conductivity, have received much attention in solid-state physics.

In recent years, it was realized that, given the exponentially large size of the quantum state of a many-particle system, many observable properties of such a systems can be computed by sampling one randomly chosen pure quantum state. The random state approach allows for the calculation of the linear response properties of many-body quantum systems using only the time evolution of a single pure random state, i.e. by solving the time-dependent Schrodinger equation for a pure state. It

relies on replacing the trace $\mathrm{Tr}\{\bullet\} = \sum_n \langle n| \bullet |n\rangle$ by a scalar product involving a single pure state $|\Phi\rangle$. More precisely, following the concept of quantum typicality, we draw $|\Phi\rangle$ at random according to a probability distribution that is invariant under all possible unitary transformations in *Hilbert space* (Haar measure) [22–31]. To solve the time-dependent Schrödinger equation of a pure state, we may use the Chebyshev polynomial algorithm [32–35]. This algorithm is known to yield results that are very accurate (close to machine precision), independent of the time step used [36]. A disadvantage of this algorithm is that, especially when the dimension of the Hilbert space is large, it consumes significantly more CPU and memory resources than a Suzuki-Trotter product-formula based algorithm [36]. Hence, once it has been verified that the numerical results of the latter are, for practical purposes, as good as the numerically exact results, we use the latter for the simulations of the large systems.

In practice, for most simulations there will not be enough memory to store the density matrix ρ, the dimension of which is the square of the dimension D of quantum state represented by complex numbers $\{c_n | n = 1, 2, ...D\}$. Due to the quadratic scaling of the Hilbert space dimension, storing the density matrix is only feasible for rather limited system sizes. Moreover, the CPU time required to advance the state by one time step is primarily determined by the numbers of operations to be performed on the state vector, that is, it also increases with the dimension of state vector. Considering, e.g., a collection of only 30 spin-1/2 particles, each of which could be identified by two complex amplitudes were it isolated, require a total of 2^{30} complex amplitudes for its state to be specified completely and the dimension of density operator ρ is $2^{60} \approx 10^{18}$. This scaling behavior limits our ability to calculate these quantum physics problems. Since it is obviously not possible to even describe the state of anything but the smallest quantum systems, one must resort to various approximation techniques to calculate properties of interest.

1.3 Outline

A common thread of the work presented in this thesis are algorithms for solving the time-dependent Schrödinger equation in combination with the so-called "random state approach". It is the use of the latter that allows us to simulate real-time quantum dynamics of many-body systems. The first three chapters are devoted to the theory that is behind the simulation algorithms.

Chapter 2 introduces a couple of explicit and stable algorithms, the Chebyshev polynomial algorithm and Suzuki-Trotter product formula algorithm, to solve the time-dependent Schrödinger equation. Chapter 3 and Chapter 4 discuss two different random state approaches in detail, and illustrate them by numerically computing the density of state of clean graphene and of two spin-1/2 models. Furthermore, it

is shown how the correlation function which determines the optical conductivity of graphene can be computed by these techniques.

In Chapter 5 we present a systematic study of the electronic transport and optical properties of a disordered graphene model, including the next-nearest-neighbor hopping. We show that this hopping has a non-negligible effect on resonant scattering but is of minor importance for long-range disorder such as charged impurities, random potentials or hoppings induced by strain fluctuations. Different types of disorders can be recognized by their fingerprints appearing in the profiles of dc conductivity, carrier mobility, optical spectroscopy and Landau level spectrum. The minimum conductivity $4e^2/h$ found in experiments is dominated by long-range disorder and the value of $4e^2/\pi h$ is due to resonant scatterers only.

In Chapter 6, we present an analyze data as obtained by the numerical solution of the time-dependent Schrödinger equation of a system containing one spin-1/2 particle interacting with a bath of up to 32 spin-1/2 particles. We numerically construct a Markovian quantum master equation describing the dynamics of the system spin. The procedure of obtaining this quantum master equation, which takes the form of a Bloch equation with time-independent coefficients, accounts for all non-Markovian effects in as much the general structure of the quantum master equation allows. Our simulation results show that, with a few rather exotic exceptions, the Bloch-type equation with time-independent coefficients provides a simple and accurate description of the dynamics of a spin-1/2 particle in contact with a thermal bath. A calculation of the coefficients that appear in the Redfield master equation in the Markovian limit shows that this perturbatively derived equation quantitatively differs from the numerically estimated Markovian master equation, the results of which agree very well with the solution of the time-dependent Schrödinger equation.

Chapter 2

The Time-Dependent Schrödinger Equation

Quantum systems are governed by the time-dependent Schrödinger equation (TDSE). In particular, the solution to the TDSE determines many physical properties of the system at hand. In this chapter, we give a detailed account of two powerful methods respectively, the Chebyshev polynomial algorithm and Suzuki-Trotter product formula algorithm, to simulate real time quantum many-body dynamics.

2.1 Basic Concepts

In quantum mechanics the physical state of a system is described by a state vector $|\Psi(t)\rangle$. This is a vector in a complex vector space which is the *Hilbert space* $\mathcal{H}$. For completeness, let us review the postulates of quantum mechanics [37]:

Postulate 1. For each physical observable A, there is a corresponding Hermitian operator $\hat{A}$. Measured values of the observable will be the eigenvalues a_n of the

operator where

$$\hat{A}|n\rangle = a_n|n\rangle \tag{2.1}$$

for the corresponding eigenvector $|n\rangle$.

Postulate 2. The observable properties of a physical system is at any time coded into a state vector $|\Psi(t)\rangle$ in the Hilbert space for the system. The expectation value of the observable A when the system is in this state, is given by

$$\langle\hat{A}\rangle(t) = \langle\Psi(t)|\hat{A}|\Psi(t)\rangle \tag{2.2}$$

when the state vector is normalized to have unit norm, i.e. $\langle\Psi(t)|\Psi(t)\rangle = 1$.

Postulate 3. The state vector $|\Psi(t)\rangle$ varies with time t according to the Schrödinger equation

$$i\hbar\frac{\partial}{\partial t}|\Psi(t)\rangle = \hat{H}|\Psi(t)\rangle \tag{2.3}$$

where $\hat{H}$ is the Hamiltonian operator[1].

A characteristic of an operator $\hat{A}$ is its *trace*, defined as

$$\mathrm{Tr}\hat{A} = \sum_j \langle n_j|\hat{A}|n_j\rangle, \tag{2.4}$$

where $|n_j\rangle$ is any orthonormal basis.

Let us express the state vector $|\Psi(t)\rangle$ by its components in the basis $|n\rangle$ formed by the eigenvectors of $\hat{A}$. Since these form a complete, orthonormal set of vectors, we have

$$|\Psi(t)\rangle = \sum_n c_n(t)|n\rangle \tag{2.5}$$

where the components $c_n(t) = \langle n|\Psi(t)\rangle$ and are confined to

$$\sum_n |c_n(t)|^2 = 1. \tag{2.6}$$

The expectation value of the quantum observable $\hat{A}$ is then

$$\langle\hat{A}\rangle(t) = \langle\Psi(t)|\hat{A}|\Psi(t)\rangle = \sum_{n,n'} c_n^*(t)c_{n'}(t)\langle n|\hat{A}|n'\rangle = \sum_n a_n|c_n(t)|^2. \tag{2.7}$$

So the average value of the measurement is the weighted average of all the eigenvalues of $\hat{A}$. The probability to measure eigenvalue a_n is $P_n = |c_n(t)|^2$.

In the above, we laid down the fundamental principles of quantum mechanics in terms of wave-functions and operators. In practice, however, we often do not know the

[1] $\hbar = h/2\pi$ is the reduced Planck constant.

precise quantum mechanical state of the system, but have some statistical knowledge about the probabilities for the system being in one of a set of states (note that these probabilities W_i are completely distinct from the probabilities P_n which according to measurements). For a fuller discussion of what follows, please see the book [38].

Suppose that there is a set of states $\{|\Psi_i\rangle\}$ for our quantum system, and that the probabilities that the system is in each of these states are $\{W_i\}$. The expectation value of an observable A is

$$\langle A\rangle_{stat} = \sum_i W_i \langle\Psi_i|A|\Psi_i\rangle, \tag{2.8}$$

which is a quantum and statistical average. Now, we re-express the expectation value of $\hat{A}$ in a different way using a basis $|K\rangle$

$$\begin{aligned}
\langle\hat{A}\rangle_{stat} &= \sum_i W_i \langle\Psi_i(t)|\hat{A}|\Psi_i(t)\rangle \\
&= \sum_i \sum_K W_i \langle\Psi_i(t)|\hat{A}|K\rangle\langle K|\Psi_i(t)\rangle \\
&= \sum_K \sum_i W_i \langle K|\Psi_i(t)\rangle\langle\Psi_i(t)|\hat{A}|K\rangle \\
&= \mathrm{Tr}\Big[\sum_i W_i |\Psi_i(t)\rangle\langle\Psi_i(t)|\hat{A}\Big] \\
&= \mathrm{Tr}\big[\rho(t)\hat{A}\big],
\end{aligned} \tag{2.9}$$

where ρ is the operator

$$\rho(t) \equiv \sum_i W_i |\Psi_i(t)\rangle\langle\Psi_i(t)|, \tag{2.10}$$

that named density operator. It provides a useful way to characterize the state of the ensemble of quantum systems.

As was shown above, The density operator ρ satisfy three conditions:

$$\mathrm{Tr}\rho = 1, \tag{2.11}$$

$$\mathrm{Tr}\rho^2 \leq 1, \tag{2.12}$$

$$\rho = \rho^\dagger, \tag{2.13}$$

$$\langle u|\rho|u\rangle \geq 0 \quad \text{for all} \quad |u\rangle. \tag{2.14}$$

IF we take as basis set the eigenvalues of Hamiltonian H $\{|\phi_j\rangle\}$ with energies $\{E_j\}$ we have that at the equilibrium the fractional population obeys the Boltzmann-Gbibs distribution i.e. $W_j \propto e^{-\beta E_j}$. Consequently

$$\rho_{eq} = \frac{\sum_j e^{-\beta E_j}|\phi_j\rangle\langle\phi_j|}{Z} = \frac{\sum_j e^{-\beta H}|\phi_j\rangle\langle\phi_j|}{Z}, \tag{2.15}$$

where β is $\left(k_B T\right)^{-1}$; with k_B being the Boltzmann constant and T the temperature of the system; Z is the partition function and can be written as

$$Z = \mathrm{Tr}\rho_{eq} = \sum_j e^{-\beta E_j}, \tag{2.16}$$

this is because the diagonal element $\rho_{jj} = \langle\phi_j|\rho|\phi_j\rangle$ indicates the fractional population for the state $\{|\phi_j\rangle\}$. So we can also express a thermally averaged expectation value as

$$\langle\hat{A}\rangle = \frac{1}{Z}\sum_j e^{-\beta E_j}\langle\phi_j|\hat{A}|\phi_j\rangle = \frac{1}{Z}\mathrm{Tr}\big[\rho\hat{A}\big]. \tag{2.17}$$

The equation of motion for the density operator follows naturally from the definition of ρ. According to **Postulate 3**, we get the quantum mechanical states is described by the Schrödinger equation

$$i\hbar\frac{\partial}{\partial t}|\Psi(t)\rangle = \hat{H}|\Psi(t)\rangle, \tag{2.18}$$

and the equation for adjoint state is

$$-i\hbar\frac{\partial\langle\Psi(t)|}{\partial t} = \langle\Psi(t)|\hat{H}. \tag{2.19}$$

If the initial state is given, then the solution can be expressed formally by means of a *time evolution operator*,

$$|\Psi(t)\rangle = U(t)|\Psi(0)\rangle, \tag{2.20}$$

and

$$\langle\Psi(t)| = \langle\Psi(0)|U(t)^\dagger. \tag{2.21}$$

It satisfies the same differential equation as does $|\Psi(t)\rangle$,

$$i\hbar\frac{\partial}{\partial t}U(t) = \hat{H}U(t), \tag{2.22}$$

and

$$-i\hbar\frac{\partial}{\partial t}U(t)^\dagger = U(t)^\dagger\hat{H}, \tag{2.23}$$

with the initial condition $U(0) = U(t=0) = 1$. Eq. (2.22) and Eq. (2.23) yield

$$i\hbar\left(U(t)^\dagger\frac{\partial U(t)}{\partial t} + \frac{U(t)^\dagger}{\partial t}U(t)\right) = i\hbar\frac{\partial\big(U(t)^\dagger U(t)\big)}{\partial t} = 0, \tag{2.24}$$

that follows the $U(t)^\dagger U(t)$ must be a constant operator and since it satisfies the initial condition $U(0) = 1$, we have $U(t)^\dagger U(t) = 1$ for all time.

If Hamiltonian H is independent on time, then

$$U(t) = e^{-(i/\hbar)Ht}. \tag{2.25}$$

If $H(t)$ is dependent on time,then,in general, there is no simple closed form for $U(t)$. So far, we can say the *time evolution operator* $U(t)$ contains all the information on the time evolution of any state$|\Psi(t)\rangle$ and hence also on the dynamics of the system.

The Eq. (2.10) gives

$$\rho(t) = U(t)\rho(0)U(t)^\dagger \tag{2.26}$$

Differentiating Eq. (2.26) with respect to t yields

$$\begin{aligned} i\hbar\frac{\partial\rho(t)}{\partial t} &= i\hbar\frac{\partial U(t)}{\partial t}\rho(0)u(t)^\dagger + i\hbar U(t)\rho(0)\frac{\partial U(t)^\dagger}{\partial t} \\ &= H(t)U(t)\rho(0)U(t)^\dagger - U(t)\rho(0)U(t)^\dagger H(t). \end{aligned} \tag{2.27}$$

Combining Eq. (2.26), we obtain

$$i\hbar\frac{\partial\rho(t)}{\partial t} = [H(t), \rho(t)] \tag{2.28}$$

with the commutator

$$[H(t), \rho(t)] = H(t)\rho(t) - \rho(t)H(t). \tag{2.29}$$

Thus the time development of a density operator can be determined either from Eq. (2.26) and Eq. (2.28), which have derived for pure states, but will be assumed to hold also for general (mixed) states. The differential (2.28) is often called the *Liouville-von Neumann equation*, because it assumes the same form as the equation of motion for the phase space probability distribution in classical mechanics [39].

2.2 Challenges

It is an important problem in quantum physics to calculate the equation (2.17) and equation (2.28). Due to the exponential scaling of the *Hilbert space* dimension, this is only feasible for rather limited system sizes. Considering, e.g., spin systems without any symmetries, numerical diagonalization using state-of-the-art computers and routines is feasible up to about 15 spins [27]. The size of the quantum systems that is able to be simulated, that is, the size for which Eq. (2.3) could actually be computed, is primarily limited by the memory required to store the pure state. Solving the TDSE requires storage of all the numbers $\{c_n|n = 1, 2, ...D\}$, D is the dimension of the complete set of orthonormal states for the *Hilbert space*. The CPU time required to advance the pure state by one time step τ is primarily determined by the

numbers of operations to be performed on the state vector, that is, it also increases with the dimension of pure state. The elementary operations performed by the computational kernel can symbolically be written as Equation(2.20), where the U's are sparse unitary matrices with a relatively complicated structure. A collection of only 30 spin-1/2 particles, each of which could be identified by two complex amplitudes were it isolated, requires a total of 2^{30} complex amplitudes for its state to be specified completely. This scaling behavior limits our ability to calculate these quantum physics problems. Since it is obviously not possible to even describe the state of anything but the smallest quantum systems, one must resort to various approximation techniques to calculate properties of interest.

Our numerical method relies on replacing the trace $\mathrm{Tr}\{\bullet\} = \sum_n \langle n| \bullet |n\rangle$ by a scalar product involving a single pure state $|\Phi\rangle$. More precisely, following the concept of quantum typicality, we draw $|\Phi\rangle$ at random according to a probability distribution that is invariant under all possible unitary transformations in *Hilbert space* (Haar measure) [22–31]. We can make use of the random state approach to reduce the computational cost to that of solving the TDSE for one pure state [22]. Using a so-constructed $|\Phi\rangle$ and abbreviating

$$|\Phi(\beta)\rangle = \frac{e^{-\beta H/2}|\Phi\rangle}{\langle\Phi|e^{-\beta H/2}|\Phi\rangle^{1/2}}, \tag{2.30}$$

the equation (2.17) can be rewritten as

$$\langle\hat{A}(t)\rangle = \frac{\mathrm{Tr}\; e^{-\beta H}\hat{A}(t)}{\mathrm{Tr}\; e^{-\beta H}} = \langle\Phi(\beta)|\hat{A}(t)|\Phi(\beta)\rangle \pm \mathcal{O}(D^{-1/2}), \tag{2.31}$$

we can use $\langle\Phi(\beta)|\hat{A}|\Phi(\beta)\rangle$ to estimate $\langle\hat{A}(t)\rangle$. As $e^{-\beta H}$ commutes with e^{-itH}, $\langle\hat{A}(t)\rangle = \langle\hat{A}(t=0)\rangle$ is time independent. Excluding the trivial case that $[H,\hat{A}(t)] = 0$, $\langle\Phi(\beta)|\hat{A}(t)|\Phi(\beta)\rangle = \langle\Phi(\beta)|e^{+itH}\hat{A}e^{-itH}|\Phi(\beta)\rangle$ depends on time. To solve the TDSE, we perform the real time propagation by $U(t)$ by means of the Chebyshev polynomial algorithm [32–35]. This algorithm is known to yield results that are very accurate (close to machine precision), independent of the time step used [36]. A disadvantage of this algorithm is that, especially when the number of spins exceeds 28, it consumes significantly more CPU and memory resources than a Suzuki-Trotter product-formula based algorithm [36]. Hence, once it has been verified that the numerical results of the latter are, for practical purposes, as good as the numerically exact results, we use the latter for the simulations of the large systems. Hence, for large quantum systems, these properties makes the problem amenable to numerical simulation, since it avoids $\mathcal{O}(D^3)$ computational efforts of matrix diagonalization, and reduce to $\mathcal{O}(D)$ computational efforts for sparse Hamiltonian matrices.

2.3 Theory

The time evolution of a state of a non-relativistic quantum-mechanical system is governed by the TDSE

$$i\frac{\partial\Psi(r,t)}{\partial t} = H\psi(r,t) \quad , \tag{2.32}$$

where H is the Hamiltonian of the model sysem, $\Psi(r,t)$ is the normalized, complex-valued wave function, $\Psi(r,0)$ is the initial state at time $t=0$, and units are such that $\hbar = 1$. The solution of the TDSE contains all dynamical information on the system. Although it is easy to see that the formal solution of Eq. (2.32) is

$$\Psi(r,t) = e^{-itH}\psi(r,0) \quad , \tag{2.33}$$

in general the explicit expression for the solution of such equations cannot be written down in closed form and one has to resort to numerical techniques to solve the initial value problem.

In analogy to ordinary differential equations, the formal solution of the matrix differential equation

$$\frac{\partial}{\partial x}U(x) = HU(x) \quad ; \quad U(0) = I \quad , \tag{2.34}$$

where I denotes the $K \times K$ unit matrix and H is a $K \times K$ matrix, is given by

$$U(x) = e^{xH} \quad , \tag{2.35}$$

and is called the exponential of the matrix H. In quantum physics and quantum statistical mechanics, the exponential of the Hamiltonian is a fundamental quantity. All methods for solving these problems compute, one way or another, (matrix elements of) the exponential of the matrix H. In the case of real-time quantum dynamics $x = -it/\hbar$ whereas for quantum statistical problems $x = -\beta = -1/k_B T$.

The matrix exponential is defined by the Taylor series

$$e^{xH} = \sum_{k=0}^{\infty} \frac{x^k H^k}{k!} \quad . \tag{2.36}$$

The above series always converges, so the exponential of the matrix H is well-defined. For most problems of interest, there won't be enough memory to store the matrix H (typical applications require matrices of dimension $10^5 \times 10^5$ or larger) and hence there also will be no memory to store the full matrix e^{xH}. Although from mathematical point of view, Eq. (2.36) is all that is really needed, it is quite useless, when it comes to computation, however. The reason is not so much that it is a Taylor series but rather that it contains powers of the matrix, indicating that simply summing the

terms in Eq. (2.36) may be very inefficient and indeed it is. So let us concentrate on the other extreme: The calculation of an arbitrary matrix element $\langle\psi|e^{xH}|\psi\prime\rangle$.

There is one particular case in which it is easy to compute the matrix element $\langle\psi|e^{xH}|\psi\prime\rangle$ namely if all eigenvalues and eigenvectors are known. Indeed, from Eq. (2.36), it follows that

$$e^{xH}|\Phi_j\rangle = \sum_{k=0}^{\infty} \frac{x^k H^k}{k!}|\Phi_j\rangle = \sum_{k=0}^{\infty} \frac{x^k}{k!} E_j^k |\Phi_j\rangle = e^{xE_j}|\Phi_j\rangle, \tag{2.37}$$

where (here and in the following) E_j denotes the $j-$th eigenvalue of the matrix H and $|\Phi_j\rangle$ is the corresponding eigenvector. We will label the eigenvalues such that $E_0 \leq E_1 \leq \cdots \leq E_{K-1}$ where K is the dimension of the matrix H. From Eq. (2.37), it is follows that

$$\langle\psi|e^{xH}|\psi\prime\rangle = \sum_{j=0}^{K-1} \langle\psi|\Phi_j\rangle\langle\Phi_j|\psi\prime\rangle e^{xE_j} \quad . \tag{2.38}$$

Of course, result of Eq. (2.38) is almost trivial but it is important to keep in mind that, except for some pathological cases, there seems to be no other practical way to compute the matrix element $\langle\psi|e^{xH}|\psi\prime\rangle$ without making approximations (assuming H is a large matrix). In general we don't know the solution of the eigenvalue problem of the matrix H, otherwise we would already have solved the most difficult part of the whole problem. Therefore Eq. (2.38) is not of practical use.

Solving the time-dependent Schrödinger equation for even a single particle moving in a non-trivial (electromagnetic) potential is not a simple matter. The main reason is that for most problem of interest, the dimension of the matrix representing H is quite large and although the dimension of the matrices involved is certainly not as large as in the case of typical many-body quantum systems, exact diagonalization techniques are quite useless. Indeed, a calculation of the time-development of the wave function by exact diagonalization techniques requires the knowledge of all eigenvectors and all eigenvalues (i.e. $\approx 10^{13}$ MB or more RAM to store these data). Thus, we need algorithms that do not use more than $\mathcal{O}(M)$ storage elements. Diagonalization methods that only require $\mathcal{O}(M)$ memory locations are of no use either because they can only compute a (small) part of the spectrum. Methods based on importance sampling concepts cannot be employed at all because there is no criterion to decide which state is important or which is not: The"weight" of a state $e^{-itE_j/\hbar}$ is a complex number of"size" one.

Although from numerical point of view the TDSE looks like any other diffierential equation which one should be able to solve by standard methods (Runge-Kutta, ...) this is not the case. Standard methods are based on (clever) truncations of the Taylor series expansion. It is easy to convince oneself that, for the TDSE, this implies that these numerical algorithms do not conserve the norm of the wave function [40].

This, from physical point of view, is unacceptable because it means that during the numerical solution of the TDSE, the number of particles will change. Moreover, it can be shown that this implies that these methods are not always stable with respect to rounding and other numerical errors. For completeness it should be mentioned that the Cranck-Nicholson algorithm does conserve the norm of the wave function and is unconditionally stable. However, except for one-dimensional problems, in terms of accuracy and efficiency it cannot compete with the algorithms to be discussed below.

A key concept in the construction of an algorithm for solving the TDSE is the socalled unconditional stability. An algorithm for solving the TDSE is unconditionally stable if the norm of the wavefunction is conserved exactly, at all times. From physical point of view, unconditional stability obviously is an essential requirement. If an algorithm is unconditionally stable the errors due to rounding, discretization etc. never run out of hand, irrespective of the choice of the grid, the time step, or the number of propagation steps. Recall that the formal solution of the TDSE is given by

$$|\Phi(m\tau)\rangle = e^{-im\tau H}|\Phi(t=0)\rangle \quad , \tag{2.39}$$

where $m = 0, 1, \ldots$ counts the number of time-steps τ. Here and in the following we absorb $\hbar$ in τ.

A simple, general recipe for constructing an unconditionally stable algorithm is to use unitary approximations to the (unitary) time-step operator $U(\tau) = e^{-i\tau H}$. The Suzuki-Trotter product formula and Chebyshev polynomial algorithms, to be discussed in the next sections, provide the necessary mathematical framework for constructing stable, accurate and efficient algorithms to solve the TDSE [40].

2.4 Numerical Methods

2.4.1 Chebyshev Polynomial Algorithm

In the following, we will introduce the Chebyshev Polynomial to reduce the exponential operation ($e^{-itH}|\phi\rangle$) to a few linear operations of the form ($\hat{H}|\phi\rangle$). The main idea is to use polynomial expansion of the exponential in the evolution operator

$$\hat{U}(t) = e^{-it\hat{H}} \approx \sum_{n=0}^{N} a_n J_n(-it\hat{H}). \tag{2.40}$$

The problem then becomes the choice of the optimal polynomial approximation.

The Chebyshev Polynomial algorithm [41] approaches this problem in analogy to the approximation of a scalar function. Consider a scalar function $f(x)$ in the interval $[-1, 1]$. In this case it is known that the Chebyshev polynomial approximations are

optimal, since the maximum error in the approximation is minimal compared to almost all possible polynomial approximations.

The algorithm is based on the numerically exact polynomial decomposition of the operator $U(t) = e^{-itH}$. Suppose real number x is in the range $[-1, 1]$. Let $x \equiv \cos\theta$, we have

$$\sin(zx) = 2\sum_{m=0}^{\infty}(-1)^m J_{2m+1}(z)\cos(2m+1)\theta, \tag{2.41}$$

$$\cos(zx) = J_0(z) + 2\sum_{m=1}^{\infty}(-1)^m J_{2m}(z)\cos(2m\theta), \tag{2.42}$$

where $J_m(z)$ is the Bessel function of integer order m, we have

$$\begin{aligned} e^{-izx} &= \cos(zx) - i\sin(zx) \\ &= J_0(z) - 2iJ_1(z)\cos\theta \\ &\quad + 2\sum_{m=1}^{\infty}(-1)^m\left[J_{2m}(z)\cos(2m\theta) - iJ_{2m+1}(z)\cos\{(2m+1)\theta\}\right] \\ &= J_0(z) - 2iJ_1(z)\cos\theta \\ &\quad + 2\sum_{m=1}^{\infty}\left[i^{2m}J_{2m}(z)\cos(2m\theta) - i^{2m+1}J_{2m+1}(z)\cos\{(2m+1)\theta\}\right] \\ &= J_0(z) + 2\sum_{m=1}^{\infty}(-i)^m J_m(z)\cos(m\theta) \\ &= J_0(z) + 2\sum_{m=1}^{\infty}(-i)^m J_m(z)T_m(x), \end{aligned} \tag{2.43}$$

where $T_m(x) = \cos[m\arccos(x)]$ is the Chebyshev polynomial of the first kind [42]. $T_m(x)$ obeys the following recurrence relation:

$$T_{m+1}(x) + T_{m-1}(x) = 2xT_m(x). \tag{2.44}$$

The Bessel function $\{J_m(z)\}$ can be numerically generated by using the following recurrence relation and associated series

$$J_{m-1}(z) = \frac{2m}{z}J_m(z) + J_{m+1}(z), \tag{2.45}$$

$$J_0(z) + 2J_2(z) + 2J_4(z) + 2J_6(z) + \cdots = 1. \tag{2.46}$$

The recurrence relation Eq.(2.45) should only be used in the decreasing direction, otherwise the result will not converge. $|J_m(z)|$ vanishes very rapidly if m becomes lager than z, and therefore we can find an M such that for all $m \geq M$, we have $|J_m(z)| < \epsilon$. Here ϵ is a small positive number, for example 10^{-15}, which determines

the accuracy of the approximation of the generated $\{J_m(z)\}$. We will derive an expression of M in the following.

From [42], the Bessel functions $J_m(mz)$ have upper bounds [43]

$$|J_m(mz)| \leq \left| \frac{z^m \exp\left[m\sqrt{1-z^2}\right]}{\left[1+\sqrt{1-z^2}\right]^m} \right|, \tag{2.47a}$$

and similarly we have

$$|J_m(z)| \leq \left| \frac{\left(\frac{z}{m}\right)^m \exp\left[m\sqrt{1-\left(\frac{z}{m}\right)^2}\right]}{\left[1+\sqrt{1-\left(\frac{z}{m}\right)^2}\right]^m} \right|, \quad \text{for} m \geq |z|. \tag{2.48}$$

Since for $z>0$, $1+\sqrt{1-(z/m)^2}<2$ and therefore from Eq.(2.48) we get

$$\ln|J_m(z)| < m\ln(\frac{z}{2m}) + \sqrt{m^2-z^2} < m\left[\ln(\frac{z}{2m})+1\right], \tag{2.49}$$

which implies that

$$|J_m(z)| < e^{m\left[\ln(\frac{z}{2m})+1\right]}. \tag{2.50}$$

The inequality $|J_m(z)|<\epsilon$ holds when $\exp\left\{m\left[\ln(\frac{z}{2m})+1\right]\right\} \leq \epsilon$, which is equivalent to

$$m\left[\ln(\frac{z}{2m})+1\right] \leq \ln\epsilon, \tag{2.51}$$

where ϵ is a small positive number and can be denoted as $\epsilon \equiv \exp(-\alpha)$, where $\alpha>1$. Equation (2.51) becomes

$$\ln(\frac{z}{2m})+1 \leq -\frac{\alpha}{m}, \tag{2.52}$$

since $m \geq z$, Eq.(2.52) also holds if

$$\ln(\frac{z}{2m})+1 \leq -\frac{\alpha}{z}, \tag{2.53}$$

or

$$m \geq \frac{1}{2}ze^{\left(1+\frac{\alpha}{z}\right)} = \frac{1}{2}ze^{\left(1-\frac{\ln\epsilon}{z}\right)}. \tag{2.54}$$

Therefore, we can introduce

$$M \equiv z\exp\left[1-(\ln\epsilon)/z\right]/2, \tag{2.55}$$

then, for all $m \geq M$, we have $|J_m(z)|<\epsilon$. Now Eq.(2.43) can be written as:

$$e^{-izx} \simeq J_0(z) + 2\sum_{m=1}^{M}(-i)^m J_m(z) T_m(x). \tag{2.56}$$

In practice, the generation of $\{J_m(z)\}$ is very fast, even if ϵ equals the numerical precision of the computer.

We can now derive the polynomial decomposition of the operator $U(t) = e^{-itH}$. In the approximation of the evolution operator, the complex Chebyshev polynomials are replaced by a function of an operator. In making this change, one has to examine the domain of the operator and adjust it to the range of definition of the Chebyshev polynomials. The range of definition of theses polynomials is from $-i$ to i. Which implies that the Hamiltonian operator has to be renormalized and the eigenvalues are in the interval $[-1, 1]$.

Since the Hamiltonian H has a complete set of eigenvectors $|E_j\rangle$ with real valued eigenvalues E_j, we can expand the wave function $|\psi(0)\rangle$ as a superposition of the $|E_j\rangle$

$$|\psi(0)\rangle = \sum_{j=0}^{K-1} |E_j\rangle \langle E_j|\psi(0)\rangle , \tag{2.57}$$

and therefore

$$|\psi(t)\rangle = e^{-itH} |\psi(0)\rangle = \sum_{j=0}^{K-1} e^{-itE_j} |E_j\rangle \langle E_j|\psi(0)\rangle . \tag{2.58}$$

Now we introduce $\|H\|_b$ as a positive number which is not smaller than the maximum of the eigenvalues E_j, that is

$$\|H\|_b \geq \|H\|_{max} \equiv \max\{|E_j|\}, \tag{2.59}$$

and introduce new variables $\hat{t} \equiv t \|H\|_b$ and $\hat{E}_j \equiv E_j / \|H\|_b$, where $\hat{E}_j$ are the eigenvalues of a modified Hamiltonian $\hat{H} \equiv H / \|H\|_b$, that is

$$\hat{H} |E_j\rangle = \hat{E}_j |E_j\rangle . \tag{2.60}$$

Now we can rewrite Eq.(2.58) as

$$|\psi(t)\rangle = \sum_{j=0}^{K-1} e^{-i\hat{t}\hat{E}_j} |E_j\rangle \langle E_j|\psi(0)\rangle . \tag{2.61}$$

Here $\left|\hat{E}_j\right| \leq 1$, which means that $\hat{E}_j$ has the same value interval of x in Eq.(2.43). Then we can use Eq.(2.43) to decompose the operator $e^{-i\hat{t}\hat{E}_j}$.

Now we use Eq.(2.56) to rewrite Eq.(2.61) as

$$\begin{aligned}|\psi(t)\rangle &\simeq \sum_{j=0}^{K-1}\left[J_0(\hat{t})+2\sum_{m=1}^{M_j}(-i)^m J_m\left(\hat{t}\right)T_m\left(\hat{E}_j\right)\right]|E_j\rangle\langle E_n|\psi(0)\rangle \\ &= J_0(\hat{t})\,|\psi(0)\rangle+2\sum_{m=1}^{M}(-i)^m J_m\left(\hat{t}\right)\sum_{j=0}^{K-1}T_m\left(\hat{E}_j\right)|E_j\rangle\langle E_j|\psi(0)\rangle \\ &= \left[J_0(\hat{t})\hat{T}_0\left(\hat{H}\right)+2\sum_{m=1}^{M}J_m\left(\hat{t}\right)\hat{T}_m\left(\hat{H}\right)\right]|\psi(0)\rangle\,, \end{aligned} \tag{2.62}$$

where

$$M_j \equiv \hat{E}_j \exp\left[1-(\ln\epsilon)/\hat{E}_j\right]/2, M \equiv \max\{M_j\}, \tag{2.63}$$

and

$$\hat{T}_m\left(\hat{H}\right)=(-i)^m T_m\left(\hat{H}\right)=(-i)^m\sum_{j=0}^{K-1}T_m\left(\hat{E}_n\right)|E_j\rangle\langle E_j|\,, \tag{2.64}$$

is a K-dimensional matrix, with diagonal elements $\hat{T}_m(\hat{E}_j)$, the modified Chebyshev polynomial, which is related to the Chebyshev polynomial $T_m(\hat{E}_j)$ by

$$\hat{T}_m\left(\hat{E}_j\right)=(-i)^m T_m\left(\hat{E}_j\right). \tag{2.65}$$

The first two matrices $\hat{T}_m$ are given by

$$\hat{T}_0\left(\hat{H}\right)|\psi\rangle = I\,|\psi\rangle\,, \hat{T}_1\left(\hat{H}\right)|\psi\rangle = -i\hat{H}\,|\psi\rangle\,. \tag{2.66}$$

From Eq.(2.44), we have the recurrence relation of the Chebyshev polynomial $T_m\left(\hat{E}_j\right)$

$$T_{m+1}\left(\hat{E}_j\right)+T_{m-1}\left(\hat{E}_j\right)=2\hat{E}_j T_m\left(\hat{E}_j\right), \tag{2.67}$$

and therefore we can get the following recurrence relation for the matrix $\hat{T}_m\left(\hat{H}\right)$

$$\begin{aligned}\hat{T}_{m+1}\left(\hat{H}\right)|\psi\rangle &= (-i)^{m+1}\sum_{j=0}^{K-1}\left[2\hat{E}_j T_m\left(\hat{E}_j\right)-T_{m-1}\left(\hat{E}_j\right)\right]|E_j\rangle\langle E_j|\psi\rangle \\ &= (-i)^{m+1}\left[2\hat{H}T_m\left(\hat{H}\right)-T_{m-1}\left(\hat{H}\right)\right]|\psi\rangle \\ &= -2i\hat{H}\hat{T}_m\left(\hat{H}\right)|\psi\rangle+\hat{T}_{m-1}\left(\hat{H}\right)|\psi\rangle\,, \end{aligned} \tag{2.68}$$

for $m \geq 1$.

By using the recurrence relation Eq.(2.68) together with Eq.(2.66), we can get $\{\hat{T}_m\left(\hat{H}\right)|\psi(0)\rangle,\ m=0,1,...,M\}$, and performing the sum in Eq.(2.62), the wave function at time t can be obtained.

The Chebyshev polynomial algorithm approaches this problem in analogy to the approximation of a scalar function. The Chebyshev polynomial algorithm is optimal in scalar case, since the maximum error in the approximation is minimal compared to almost all possible polynomial approximations. One of the most important aspects of this algorithm is that the error is uniformly distributed over the entire range of eigenvalues. This scheme can be used as an accuracy check due to its extreme accuracy, even though this method is not unitary [44].

2.4.2 Suzuki-Trotter Product Formula Algorithm

The following fundamental result is the basis for the Suzuki-Trotter method for solving quantum problems [40, 45–48]. It expresses the exponential of a sum of two matrices as infinite ordered product of the exponentials of the two individual matrices:

$$e^{x(A+B)} = \lim_{m\to\infty} (e^{xA/m} e^{xB/m})^m \quad , \tag{2.69}$$

where, for our purposes, A and B are $M \times M$ matrices. Equation (2.69) is called the Trotter formula [49]. Note that $e^{A+B} = e^A e^B$ if and only if the matrices A and B commute, i.e. $[A, B] = AB - BA = 0$.

A first hint for understanding why Eq. (2.69) holds comes from computing the two Taylor series

$$\begin{aligned} e^{x(A+B)/m} &= I + \frac{x}{m}(A+B) + \frac{1}{2}\frac{x^2}{m^2}(A+B)^2 + \mathcal{O}(x^3/m^3) \\ &= I + \frac{x}{m}(A+B) + \frac{1}{2}\frac{x^2}{m^2}(A^2 + AB + BA + B^2) + \mathcal{O}(x^3/m^3) \quad , \end{aligned} \tag{2.70}$$

and

$$e^{xA/m} e^{xB/m} = I + \frac{x}{m}(A+B) + \frac{1}{2}\frac{x^2}{m^2}(A^2 + 2AB + B^2) + \mathcal{O}(x^3/m^3) \quad . \tag{2.71}$$

It is clear that for sufficiently large m, both expansions will agree up to terms of $\mathcal{O}(x^2\|[A,B]\|/m^2)$. [2]. Thus, for sufficiently large m (how large depends on x and $\|[A,B]\|$),

$$e^{x(A+B)/m} \approx e^{xA/m} e^{xB/m} \quad . \tag{2.72}$$

A mathematically rigorous treatment shows that [50, 51]

$$\|e^{x(A+B)/m} - e^{xA/m} e^{xB/m}\| \leq \frac{x^2}{2m^2}\|[A,B]\| e^{|x|(\|A\|+\|B\|)/m} \quad , \tag{2.73}$$

demonstrating that for finite m, the difference between the exponential of a sum of two matrices and the ordered product of the individual exponentials vanishes as x^2/m.

[2] The norm of a matrix $\mathbb{X}$ is defined as $\|\mathbb{X}\| = M^{-1/2}(\mathrm{Tr}\ \mathbb{X}^\dagger \mathbb{X})^{1/2}$.

As expected, Eq. (2.73) also reveals that this difference is zero if A and B commute:If $[A, B] = 0$ then $e^{x(A+B)=e^{xA}e^{xB}}$, as already mentioned above. For the case at hand $x = -im\tau$ and then the upperbound in Eq. (2.73) can be improved considerably to read [40]

$$\|e^{-i\tau(A+B)/m} - e^{-i\tau A/m}e^{-i\tau B/m}\| \leq \frac{\tau^2}{2}\|[A, B]\| \quad . \tag{2.74}$$

Except for the fact that we assumed that $H = A + B$, the above discussion has been extremely general. This suggests that one can apply the Suzuki-Trotter approach to a wide variety of problems and indeed one can. We have only discussed the most simple form of the Trotter formula.

The Trotter formula is readily generalized to the case of more than two contributions to H. Writing $H = \sum_{i=1}^{p} A_i$ it can be shown that [40, 50, 51]

$$\|e^{-i\tau(A_1+\cdots+A_p)} - e^{-i\tau A_1}\ldots e^{-i\tau A_p}\| \leq \frac{\tau^2}{2}\sum_{1\leq i\leq j\leq p}\|[A_i, A_j]\| \quad , \tag{2.75}$$

showing that any decomposition of the Hamiltonian qualifies as a candidate for applying the Suzuki-Trotter approach. This is an important conclusion because the flexibility of choosing the decomposition of H can be exploited to construct efficient algorithms. From the above discussion it is also clear that at no point, an assumption was made about the "importance" of a particular contribution to H. This is the reason why the Suzuki-Trotter approach can be used where perturbation methods break down.

The product formula Eq. (2.73) is the simplest one can think of. We use it to define an approximate time-step operator

$$U_1(\tau) = e^{-i\tau A_1}\ldots e^{-i\tau A_p} \quad . \tag{2.76}$$

The hermitian conjugate of this operator is given by

$$U_1^\dagger(\tau) = e^{-i\tau A_p}\ldots e^{-i\tau A_1} \quad , \tag{2.77}$$

from which it follows that

$$U_1(\tau)U_1^\dagger(\tau) = I \quad . \tag{2.78}$$

For simplicity we have assumed that H has be written as a sum of hermitian contributions, i.e. $A_i = A_i^\dagger$ for $i = 1, \cdots, p$. Eq. (2.78) implies that $(U_1(\tau))^{-1} = U_1^\dagger(\tau)$ hence $U_1(\tau)$ is a unitary approximation to the time-step operator $e^{-i\tau H}$. Thus, if we succeed in implementing $U_1(\tau)$, the resulting algorithm will be unconditionally stable by construction. The upperbound in Eq. (2.75) shows that the error made by replacing $e^{-i\tau H}$ by $U_1(\tau)$ will, in the worst case, never exceed a constant multiplied by τ^2. Therefore $U_1(\tau)$ could be a good approximation to $U(\tau)$ if we use a small time step τ such that $\tau(A_1 + \cdots + A_p) \ll 1$. Also, it shows from Eq.(2.75) that the Taylor

series of $U(\tau)$ and $U_1(\tau)$ are identical up to first order of τ and we name $U_1(\tau)$ the first-order approximant to the time-step operator $U(t)$.

The Suzuki-Trotter product formula approach provides a simple, systematic procedure to improve the accuracy of the approximation of $U(t)$ without changing its fundamental properties. The higher-order approximations of the unitary matrix are also introduced.

$$U_2(\tau) = U_1^T(\tau/2)U_1(\tau/2) \quad , \tag{2.79}$$

is the second-order approximation of $U(\tau)$ [46, 50, 52], where the U_1^T is the transpose of U_1. The upperbound for the error of this approximation is [40]

$$\|U(\tau) - U_2(\tau)\| \leq c_2\tau^3 \quad , \tag{2.80}$$

with a positive constant c_2.

Suzuki-Trotter formula-based procedures to construct algorithms that are correct up to fourth-order in the time step are given in ref.[40]. From practical point of view, a disadvantage of the fourth-order methods introduced in ref.[40] is that they involve commutators of various contributions to the Hamiltonian. Suzuki proposed a symmetrized fractal decomposition of the time evolution operator. Using this formula, a fourth-order algorithm is easily from a second-order algorithm by applying [46, 50, 52]

$$U_4(\tau) = U_2(p\tau)U_2(p\tau)U_2((1-4p)\tau)U_2(p\tau)U_2(p\tau) \quad , \tag{2.81}$$

where $p = 1/(4 - 4^{1/3})$ and $U_n(\tau)$ is the n-th order approximation to $U(\tau)$, i.e. $U(\tau) = U_n(\tau) + \mathcal{O}(\tau^{n+1})$.

$$\|U(\tau) - U_4(\tau)\| \leq c_4\tau^5 \quad , \tag{2.82}$$

where c_4 is a positive constant as c_2. It is trivial to show that all of the above approximations are unitary operators, hence the corresponding algorithms will be unconditionally stable. Note that once we have programmed a frst-order algorithm, writing the code to implement the second- and fourth-order algorithms will normally only take a few seconds. Finally we would like to emphasize that there are many different ways to construct and use higher-order Suzuki-formulae and that it is by no means clear that the ones used above lead to the most efficient algorithms for other kinds of TDSE problems. A systematic comparison of various schemes is given in Ref.[53].

2.5 Implementation

In this section, we introduce Suzuki-Trotter Product formula to compute the exponential of the Hamiltonian. In all cases of practical interest, the Hamiltonian can be

written as a sum of operators $H = \sum_{i=1}^{p} H_i$ in such a manner that each H_i is sufficiently simple so that it can be diagonalized easily, i.e. analytically. The time-step operator $U(t)$ is then approximated by some ordered product of exponents of $e^{-i\tau H_i}$. Such approximate time-step operators are unitary and therefore algorithms based on them are unconditionally stable. Since the eigenvalues and eigenvectors of H_i are known, calculation of $H = \sum_{i=1}^{p} H_i$ is straightforward.

2.5.1 Spin-1/2 Model

Quantum spin systems are rather complicated many-body systems and except for some special cases their time evolution cannot be calculated analytically. However, a lot of information can be extracted from quantum simulations with efficient algorithms, if we are able to simulate the dynamics of the system directly by solving the time-dependent Schrödinger equation.

The Hamiltonian of a spin 1/2 system of N coupled spins that we will study is given by

$$H(t) = -\sum_{i,j=1}^{N} \sum_{\alpha=x,y,z} h_i^{\alpha}(t) S_i^{\alpha} - \sum_{i,j=1}^{N} \sum_{\alpha=x,y,z} J_{i,j}^{\alpha}(t) S_i^{\alpha} S_j^{\alpha}, \tag{2.83}$$

where $h_i^{\alpha}(t)$ is the external magnetic field applied on the $i-th$ spin, and $J_{i,j}^{\alpha}(t)$ correspond to the exchange parameters that determine the strength of interactions between the α-components of spins i and j.

The three components of the spin-1/2 operator S acting on the Hilbert space spanned by the states $|\uparrow\rangle$ and $|\downarrow\rangle$ are defined by [54–56]

$$S^x = \frac{1}{2}\begin{pmatrix} 0 & 1 \\ 1 & 0 \end{pmatrix}, \qquad S^y = \frac{1}{2}\begin{pmatrix} 0 & i \\ -i & 0 \end{pmatrix}, \qquad S^z = \frac{1}{2}\begin{pmatrix} 1 & 0 \\ 0 & -1 \end{pmatrix}. \tag{2.84}$$

in units such that $\hbar = 1$.

The wave function that describes the spin of these objects can be written as a linear combination of the spin-up and spin-down states [54–56],

$$|\Phi\rangle = a_0|\uparrow\rangle + a_1|\downarrow\rangle, \tag{2.85}$$

where a_0 and a_1 are complex numbers. It is convenient to normalize the length of the vector $|\Phi\rangle$ to one, then $|a_0|^2 + |a_1|^2 = 1$. Similarly, the quantum state of the spin 1/2 system with N spins can be represented by

$$\begin{aligned} |\phi\rangle = {} & a(\uparrow\uparrow \ldots \uparrow\uparrow)\,|\uparrow\uparrow \ldots \uparrow\uparrow\rangle + a(\uparrow\uparrow \ldots \uparrow\downarrow)\,|\uparrow\uparrow \ldots \uparrow\downarrow\rangle + \ldots \\ & + a\,(\downarrow\downarrow \ldots \downarrow\uparrow)\,|\downarrow\downarrow \ldots \downarrow\uparrow\rangle + a\,(\downarrow\downarrow \ldots \downarrow\downarrow)\,|\downarrow\downarrow \ldots \downarrow\downarrow\rangle\,. \end{aligned} \tag{2.86}$$

Let spin up (down) corresponds to the state 0 (1), then

$$\begin{aligned}|\phi\rangle &= a(00...00)\,|00...00\rangle + a(00...01)\,|00...01\rangle + ... \\ &\quad + a\,(11...10)\,|11...10\rangle + a\,(11...11)\,|11...11\rangle \\ &= \sum_{k=0}^{2^N-1} a_k\,|k\rangle\,. \end{aligned} \tag{2.87}$$

Here we denote the spins from right to left, which means in the translations between notations, from spin up (down) to a binary number, the first bit in the binary number corresponds to the $1st$ spin, and the last bit to the N-th spin. The coefficients a_k are complex numbers, and it is convenient to normalize $\langle\phi|\phi\rangle = 1$:

$$\sum_{k=0}^{2^N-1} |a_k|^2 = 1. \tag{2.88}$$

The time evolution of the quantum state can be given by

$$|\phi(t+\tau)\rangle = U\,(\tau)\,|\phi(t)\rangle \simeq e^{-i\tau H(t)}\,|\phi(t)\rangle\,. \tag{2.89}$$

We adopt Suzuki-Trotter Product formula algorithm for solving the time evolution problems. First, the Hamiltonian H in Eq.(2.83) is decomposed into two parts:

$$H_a\,(t) = -\sum_{j=1}^{N}\sum_{\alpha=x,y,z} h_j^\alpha(t) S_j^\alpha, \tag{2.90}$$

$$H_b\,(t) = -\sum_{j,k=1}^{N}\sum_{\alpha=x,y,z} J_{j,k}^\alpha(t) S_j^\alpha S_k^\alpha, \tag{2.91}$$

where $H_a\,(t)$ contains the external time-dependent fields and $H_b\,(t)$ contains the exchange coupling of the spins.

For $H_a\,(t)$, we consider the case when the external field changes slowly such that in each small time step τ the external field can be regarded as a constant. Since the spin operators with different spin labels commute, that is $[S_i^\alpha, S_j^\alpha] = 0$, if $i \neq j$, and using the fact that

$$e^{A+B} = e^A e^B \quad \text{if } [A,B] = 0, \tag{2.92}$$

we have

$$\begin{aligned} U_a\,(\tau) &= e^{-i\tau H_a(t)} = \exp\left[i\tau \sum_{j=1}^{N}\sum_{\alpha=x,y,z} h_j^\alpha(t) S_j^\alpha\right] \\ &= \prod_{j=1}^{N} \exp\left[i\tau \sum_{\alpha=x,y,z} h_j^\alpha(t) S_j^\alpha\right] = \prod_{j=1}^{N} \exp\left[i\tau \mathbf{S}_j \cdot \mathbf{h}_j(t)\right]. \end{aligned} \tag{2.93}$$

We introduce $\widehat{\mathbf{h}}_j(t) \equiv \mathbf{h}_j(t)/h_j(t)$, where $h_j(t) = \|\mathbf{h}_j(t)\|$. Then $\mathbf{S}_j \cdot \widehat{\mathbf{h}}_j(t)$ is the projection of $\mathbf{S}_j$ on the direction $\widehat{\mathbf{h}}_j(t)$ and it is easy to prove that

$$\begin{aligned}
& \exp\left[i\tau \mathbf{S}_j \cdot \mathbf{h}_j(t)\right] \\
= & \cos\left(\frac{\tau h_j(t)}{2}\right) + 2i\mathbf{S}_j \cdot \widehat{\mathbf{h}}_j(t) \sin\left(\frac{\tau h_j(t)}{2}\right) \\
= & \begin{pmatrix} \cos\left(\frac{\tau h_j(t)}{2}\right) + \frac{ih_j^z(t)}{h_j(t)} \sin\left(\frac{\tau h_j(t)}{2}\right) & \frac{ih_j^x(t)+h_j^y(t)}{h_j(t)} \sin\left(\frac{\tau h_j(t)}{2}\right) \\ \frac{ih_j^x(t)-h_j^y(t)}{h_j(t)} \sin\left(\frac{\tau h_j(t)}{2}\right) & \cos\left(\frac{\tau h_j(t)}{2}\right) - \frac{ih_j^z(t)}{h_j(t)} \sin\left(\frac{\tau h_j(t)}{2}\right) \end{pmatrix}.
\end{aligned} \tag{2.94}$$

For $H_b(t)$, the pair-product decomposition is defined by [57, 58]

$$\begin{aligned}
U_b(\tau) &= e^{-i\tau H_b(t)} = \exp\left[i\tau \sum_{j,k=1}^{N} \sum_{\alpha=x,y,z} J_{j,k}^{\alpha}(t) S_j^{\alpha} S_k^{\alpha}\right] \\
&= \prod_{j,k=1}^{N} \exp\left[i\tau \sum_{\alpha=x,y,z} J_{j,k}^{\alpha}(t) S_j^{\alpha} S_k^{\alpha}\right],
\end{aligned} \tag{2.95}$$

and each factor can be calculated analytically as

$$\begin{aligned}
& \exp\left[i\tau \sum_{\alpha=x,y,z} J_{j,k}^{\alpha}(t) S_j^{\alpha} S_k^{\alpha}\right] \\
= & \begin{pmatrix} e^{ia\tau}\cos b\tau & 0 & 0 & ie^{ia\tau}\sin b\tau \\ 0 & e^{-ia\tau}\cos c\tau & ie^{-ia\tau}\sin c\tau & 0 \\ 0 & ie^{-ia\tau}\sin c\tau & e^{-ia\tau}\cos c\tau & 0 \\ ie^{ia\tau}\sin b\tau & 0 & 0 & e^{ia\tau}\cos b\tau \end{pmatrix}_{jk},
\end{aligned} \tag{2.96}$$

where $a = J_{j,k}^z(t)/4$, $b = \left[J_{j,k}^x(t) - J_{j,k}^y(t)\right]/4$ and $c = \left[J_{j,k}^x(t) + J_{j,k}^y(t)\right]/4$.

The matrix in Eq.(2.94) is just a single spin 1/2 operation. Equation (2.96) is more complicated but can be performed in a similar manner as a two-spin 1/2 operation, therefore we will not give a more detailed description.

2.5.2 Tight-Binding Model

Here, we give a general tight-bind Hamiltonian as a example,

$$H = T \sum_{l=1}^{K-1} (c_l^+ c_{l+1} + c_{l+1}^+ c_l) + V \sum_{l=1}^{K} \epsilon_l n_l \quad , \tag{2.97}$$

where $c_l^+(c_l)$ creates (annihilates) a particle at the site l, $n_l = c_l^+ c_l$ counts the number of particles at site l, T sets the kinetic energy scale and $V\epsilon_l$ is the potential at site l felt by the particle. the time evolution dynamical state $|\psi(t)\rangle$ of this single particle system can be written as $|\psi(t)\rangle = \sum_{l=1}^{K} \psi_l(t) c_l^+ |0\rangle$ in which $|0\rangle$ denotes the vacuum state. Substituting this representation in the TDSE with H given by Eq.(2.97) yields

$$\frac{\partial}{\partial t}\psi_l(t) = -i\{T[\psi_{l+1}(t) + \psi_{l-1}(t)] + V\epsilon_l\psi_l(t)\}; \quad l = 1, 2, \ldots, K-1, K. \tag{2.98}$$

Because of the free boundary conditions $\psi_l(t) = 0$,if $l \leq 0$ or $l > K$. Also,

$$H = \begin{bmatrix} V\epsilon_1 & T & 0 & & & 0 \\ T & V\epsilon_2 & T & & & \\ 0 & T & V\epsilon_3 & & & \\ & & & \ddots & & 0 \\ & & & T & V\epsilon_{K-1} & T \\ 0 & & & 0 & T & V\epsilon_K \end{bmatrix} \tag{2.99}$$

is a tri-diagonal $K \times K$ matrix representing the Hamiltonian. For simplicity of notation it has been assumed that K is odd. Here, we decompose hamiltonian H into a diagonal matrix and two block-diagonal matrices as follows $H = H_V + H_{HO} + H_{HE}$,

$$H_V = \begin{bmatrix} V\epsilon_1 & 0 & 0 & & & 0 \\ 0 & V\epsilon_2 & 0 & & & \\ 0 & 0 & V\epsilon_3 & & & \\ & & & \ddots & & 0 \\ & & & 0 & V\epsilon_{K-1} & 0 \\ 0 & & & 0 & 0 & V\epsilon_K \end{bmatrix}, \tag{2.100}$$

$$H_{TO} = \begin{bmatrix} 0 & T & 0 & 0 & & & 0 \\ T & 0 & 0 & 0 & & & \\ 0 & 0 & 0 & T & & & \\ 0 & 0 & T & 0 & & & 0 \\ & & & \ddots & & 0 & \\ & & & & 0 & T & 0 \\ & & & & T & 0 & 0 \\ 0 & & & & 0 & 0 & 0 \end{bmatrix}, \qquad H_{TE} = \begin{bmatrix} 0 & 0 & 0 & 0 & & & 0 \\ 0 & 0 & T & 0 & & & \\ 0 & T & 0 & 0 & & & \\ 0 & 0 & 0 & 0 & & & 0 \\ & & & \ddots & & 0 & \\ & & & & 0 & 0 & 0 \\ & & & & 0 & 0 & T \\ 0 & & & & 0 & T & 0 \end{bmatrix}. \tag{2.101}$$

The second-order product-formula are obtained by symmetrizing first-order formula as follows

$$U(\tau) = e^{-i\tau H} \approx e^{-i\tau/2H_{TO}} e^{-i\tau/2H_{TE}} e^{-i\tau H_V} e^{-i\tau/2H_{TE}} e^{-i\tau/2H_{TO}} \quad . \tag{2.102}$$

The block-diagonal structure of H_{TO} and H_{TE} simplifies the calculation of $e^{-i\tau H_{TO}/2}$ and $e^{-i\tau H_{TE}/2}$ tremendously, since the problem has essentially been reduced to the exponentiation of 2×2 matrices of the form

$$W_T = \begin{bmatrix} 0 & T \\ T & 0 \end{bmatrix}; \qquad W_V = \begin{bmatrix} V_l & 0 \\ 0 & V_{l+1} \end{bmatrix}, \quad l = 1, 2, \ldots, k-2, K-1, \tag{2.103}$$

with $V_l = V\epsilon_l$. Denoting the matrix $T_l(\tau) \equiv e^{-i\tau W_T}$ and $W_l(\tau) \equiv e^{-i\tau W_V}$, we have

$$T_l(\tau) = \exp\left(-i\tau T \begin{bmatrix} 0 & 1 \\ 1 & 0 \end{bmatrix}\right) = \begin{bmatrix} \cos(\tau T) & -i\sin(\tau T) \\ -i\sin(\tau T) & \cos(\tau T) \end{bmatrix}, \tag{2.104}$$

$$\begin{aligned} W_l(\tau) &= \exp\left(-i\tau \begin{bmatrix} V_l & 0 \\ 0 & V_{l+1} \end{bmatrix}\right) \\ &= \begin{bmatrix} \cos(\tau V_l) - i\sin(\tau V_l) & 0 \\ 0 & \cos(\tau V_{l+1}) - i\sin(\tau V_{l+1}) \end{bmatrix}. \end{aligned} \tag{2.105}$$

Then the second-order approximant $U_2(\tau)$ can be easily calculate straightforward.

2.6 Conclusion

In conclusion, the Chebyshev polynomial algorithm and Suzuki-Trotter product formula algorithm have been explained in detail to solve the TDSE in different quantum dynamic models. Each method has its merits and limits. In fact, specific problems will of course have difference requirements for the method used to solve the TDSE. We should exercise discretion with regard to the different model.

Chapter 3

Random State Approach: I

Here and in the following chapter we treat two different random state approaches to explore the properties of quantum systems. In this chapter, we show that it is a good approximation to replace the trace of large matrix by its average with respect to a random state. Then we introduce the thermal random state and analyze its properties.

3.1 Theory

The underlying idea of the random-state approach is replacing Tr X by $\langle\Phi|X|\Phi\rangle$ where $X = X^\dagger$ is a $D \times D$ Hermitian matrix. It will be proved to be a good approximation to replace the Tr X with the random random state $|\Phi\rangle = \sum_{a=1}^{D} \xi_a |a\rangle$ where the ξ_a's are complex-valued Gaussian random variables and the set $\{|a\rangle\}$ can be any complete set of orthonormal states in the Hilbert space. The demonstration that this approximation is indeed useful requires a proof that by averaging over the ξ_a. We recover the correct answer Tr X and that the variance of $\langle\Phi|X|\Phi\rangle$ is bounded.

To simplify the mathematics, we will work with independent complex-valued Gaus-

sian random variables unlike in Ref. [22], and assume the identical Gaussian distributions with mean zero and variance σ^2 for all the real and imaginary parts of the variables. Thus, we will not normalize the state $\sum_a \xi_a|a\rangle$. It will be clear that this makes the calculations simpler without affecting the final results in an essential way.

We denote the expectation by E[.] with respect to the multivariate Gaussian probability distribution by ξ's. Then we have

$$\begin{aligned} P(\xi_1,\ldots,\xi_D) &= \prod_{a=1}^{D}\left[\frac{1}{2\pi\sigma^2}e^{-|\xi_a|^2/2\sigma^2}\right] d(\mathrm{Re}\ \xi_a)\, d(\mathrm{Im}\ \xi_a) \\ \mathrm{E}[\xi_a] &= \mathrm{E}[\xi_p] = \mathrm{E}[\xi_a\xi_b] = 0 \\ \mathrm{E}[\xi_a^*\xi_p] &= 2\sigma^2\delta_{a,p} \\ \mathrm{E}[\xi_a^*\xi_b^*\xi_p\xi_q] &= \mathrm{E}[\xi_a^*\xi_p]\mathrm{E}[\xi_b^*\xi_q] + \mathrm{E}[\xi_a^*\xi_q]\mathrm{E}[\xi_b^*\xi_p] = 4\sigma^4\left(\delta_{a,p}\delta_{b,q} + \delta_{a,q}\delta_{b,p}\right) \end{aligned} \tag{3.1}$$

where D denotes the dimension of the Hilbert space.

For any matrix X, there is

$$\begin{aligned} \mathrm{E}[\langle\Phi|X|\Phi\rangle] &= \sum_{\{a,p\}=1}^{D}\mathrm{E}[\xi_a^*\xi_p]\langle a|X|p\rangle = \sum_{a=1}^{D}\mathrm{E}[\xi_a^*\xi_a]\langle a|X|a\rangle \\ &= \sum_{a=1}^{D}\mathrm{E}[\xi_a^*\xi_a]\langle a|X|a\rangle = 2\sigma^2\mathrm{Tr}\ X, \end{aligned} \tag{3.2}$$

and because $\langle\Phi|X|\Phi\rangle = \langle\Phi|X|\Phi\rangle^*$, the corresponding variance is given by

$$\begin{aligned} \mathrm{Var}\left(\langle\Phi|X|\Phi\rangle\right) &= \mathrm{E}[|\langle\Phi|X|\Phi\rangle|^2] - |\mathrm{E}[\langle\Phi|X|\Phi\rangle]|^2 \\ &= \sum_{a,p,b,q=1}^{D}\mathrm{E}[\xi_a^*\xi_p\xi_b\,\xi_q^*]\langle a|X|p\rangle\langle b|X|q\rangle^* - 4\sigma^4\left|\mathrm{Tr}\ X\right|^2 \\ &= 4\sigma^4\sum_{a,b=1}^{D}\left(\langle a|X|a\rangle\langle b|X|b\rangle^* + \langle a|X|b\rangle\langle a|X|b\rangle^*\right) - 4\sigma^4\left|\mathrm{Tr}\ X\right|^2 \\ &= 4\sigma^4\mathrm{Tr}\ XX^\dagger. \end{aligned} \tag{3.3}$$

In general, both $\mathrm{E}[\langle\Phi|X|\Phi\rangle]$ and $\mathrm{Var}\left(\langle\Phi|X|\Phi\rangle\right)$ can take almost arbitrary values, because σ can be chosen at will. Therefore, if $|\langle\Phi|X|\Phi\rangle| > 0$ it makes sense to consider the relative standard deviation defined by

$$\mathrm{RSD}^2(\langle\Phi|X|\Phi\rangle) \equiv \frac{\mathrm{Var}(\langle\Phi|X|\Phi\rangle)}{|\mathrm{E}[\langle\Phi|X|\Phi\rangle]|^2} = \frac{\mathrm{Tr}\ XX^\dagger}{\left|\mathrm{Tr}\ X\right|^2} = \frac{\mathrm{Tr}\ XX^\dagger}{(\mathrm{Tr}\ X)(\mathrm{Tr}\ X^\dagger)}. \tag{3.4}$$

As $\mathrm{Tr}\, X^\dagger Y \equiv (X,Y)$ defines a scalar product, by the Schwarz inequality we have in general

$$|\mathrm{Tr}\, X|^2 = |(\mathbb{1},X)|^2 \leq (\mathbb{1},\mathbb{1})(X,X) = D\mathrm{Tr}X^\dagger X, \tag{3.5}$$

and hence

$$\mathrm{RSD}(\langle\Phi|X|\Phi\rangle) \quad \geq \quad \frac{1}{\sqrt{D}}, \tag{3.6}$$

but to prove that the approach is useful in actual applications, we have to show that the variance and/or relative standard deviation is finite and, idealy, also vanishes with the system size. This may be accomplished by deriving an upper bound to the variance and the relative standard deviation.

Let us put $X = e^{-\beta H/2} Y e^{-\beta H/2}$ where $H = H^\dagger$ and $Y = Y^\dagger$ which implies $X = X^\dagger$. Using Eqs. (3.2)– (3.4) we have

$$\mathrm{E}[\langle\Phi|X|\Phi\rangle] \quad = \quad 2\sigma^2 \mathrm{Tr}\; X = 2\sigma^2 \mathrm{Tr}\; e^{-\beta H} Y, \tag{3.7}$$

and

$$\begin{aligned} \mathrm{Var}\left(\langle\Phi|X|\Phi\rangle\right) &= 4\sigma^4 \mathrm{Tr}\; e^{-\beta H/2} Y e^{-\beta H/2} e^{-\beta H/2} Y e^{-\beta H/2} \\ &= 4\sigma^4 \mathrm{Tr}\; \left(e^{-\beta H} Y\right)\left(e^{-\beta H} Y\right) = 4\sigma^4 \mathrm{Tr}\; \left(e^{-\beta H} Y\right)^2. \end{aligned} \tag{3.8}$$

With $A = e^{-\beta H}$ and $B = Y$ we can write

$$\begin{aligned} \mathrm{Var}^2\left(\langle\Phi|X|\Phi\rangle\right) &= 16\sigma^8 \left|\mathrm{Tr}\; (AB)^2\right|^2 = \left|((AB)^\dagger, AB)\right|^2 \\ &\leq 16\sigma^8 (AB, AB)((AB)^\dagger, (AB)^\dagger) \\ &= 16\sigma^8 \left(\mathrm{Tr}\; (AB)^\dagger AB\right)^2 \\ &= 16\sigma^8 \left(\mathrm{Tr}\; A^2 B^2\right)^2. \end{aligned} \tag{3.9}$$

As $\mathrm{Tr}\; (AB)^2 = \mathrm{Tr}\; (e^{-\beta H/2} Y e^{-\beta H/2})(e^{-\beta H/2} Y e^{-\beta H/2})^\dagger \geq 0$, it follows that

$$\mathrm{Var}\left(\langle\Phi|X|\Phi\rangle\right) \quad = \quad 4\sigma^4 \mathrm{Tr}\; \left(e^{-\beta H} Y\right)^2 \leq 4\sigma^4 \mathrm{Tr}\; e^{-2\beta H} Y^2 \tag{3.10}$$

$$\mathrm{RSD}^2(\langle\Phi|X|\Phi\rangle) \quad \leq \quad \frac{\mathrm{Tr}\; e^{-2\beta H} Y^2}{\left(\mathrm{Tr}\; e^{-\beta H} Y\right)^2}. \tag{3.11}$$

3.2 Application

3.2.1 Thermal Random State

In our simulations, we use the thermal random state defined by

$$|\Phi_\beta\rangle \quad = \quad e^{-\beta H/2} |\Phi\rangle, \tag{3.12}$$

to compute estimates of thermal equilibrium expectation values. We can use the inequality Eqs. (3.11) to prove that the statistical error on the estimate of the partition

function vanishes exponentionally with the system size. Specializing to $Y = \mathbb{1}$ and noting that $\langle\Phi|e^{-\beta H}|\Phi\rangle > 0$, we have

$$\begin{aligned} \mathrm{E}[\langle\Phi|e^{-\beta H}|\Phi\rangle] &= 2\sigma^2 \mathrm{Tr}\, e^{-\beta H} = 2\sigma^2 Z(\beta) = 2\sigma^2 e^{-\beta F(\beta)} && (3.13)\\ \mathrm{Var}\left(\langle\Phi|e^{-\beta H}|\Phi\rangle\right) &= 4\sigma^4 \mathrm{Tr}\, e^{-2\beta H} = 4\sigma^4 Z(2\beta) = 4\sigma^4 e^{-2\beta F(2\beta)} && (3.14)\\ \mathrm{RSD}(\langle\Phi|e^{-\beta H}|\Phi\rangle) &\leq e^{-\beta(F(2\beta)-F(\beta))}, && (3.15) \end{aligned}$$

where $F(\beta)$ denotes the free energy of the system at the inverse temperature β.

As the free energy is an extensive quantity, i.e. it is proportional to the number of particles, and $F(2\beta) - F(\beta) > 0$ for $\beta > 0$, we have $e^{-\beta(F(2\beta)-F(\beta))} = \mathcal{O}(e^{-N})$ and we obtain

$$\mathrm{RSD}(\langle\Phi|e^{-\beta H}|\Phi\rangle) \leq e^{-\beta(F(2\beta)-F(\beta))} = \mathcal{O}(e^{-N}). \quad (3.16)$$

Using

$$\lim_{\beta\to 0} e^{-\beta F(\beta)} = \mathrm{Tr}\,\mathbb{1} = D, \quad (3.17)$$

and Eq. (3.6) we find that

$$\lim_{\beta\to 0} \mathrm{RSD}\left(\langle\Phi_\beta|\Phi_\beta\rangle\right) \leq \frac{1}{\sqrt{D}}. \quad (3.18)$$

Moreover, from Eq. (3.6) and Eq. (3.18) it follows that

$$\lim_{\beta\to 0} \mathrm{RSD}\left(\langle\Phi_\beta|\Phi_\beta\rangle\right) = \frac{1}{\sqrt{D}}. \quad (3.19)$$

From Eqs. (3.16) and (3.19) it follows that $\mathrm{RSD}\left(\langle\Phi_\beta|\Phi_\beta\rangle\right)$ vanishes exponentially with the system size N.

Recall that we can choose σ as we like. From Eq. (3.13), it is clear that if we choose $\sigma = 1/\sqrt{2}$ we have $\mathrm{E}[\langle\Phi|e^{-\beta H}|\Phi\rangle] = \mathrm{Tr}\, e^{-\beta H} = e^{-\beta F(\beta)}$ that is, the norm of the thermal state is, up to statistical fluctuations which vanish as $1/D$, equal to the partition function.

3.2.2 Thermal Averages

In this subsection we set $X = e^{-\beta H/2} Y e^{-\beta H/2}$ where $H = H^\dagger$ and $Y = Y^\dagger$, write $Z = e^{-\beta H}$ and to simplify the writing (but without loss of generality), we also choose $\sigma = 1/\sqrt{2}$.

The general idea of the approach is that it suffices to generate one Gaussian random state $|\Phi\rangle$ to find good estimates for $\langle Y\rangle = \mathrm{Tr}\, e^{-\beta H} Y / \mathrm{Tr}\, e^{-\beta H} = \mathrm{Tr}\, X / \mathrm{Tr}\, Z$. The question is if we can prove that the statistical fluctuations are small in some

sense. The problem is the following: In the simulation we generate a random state $|\Phi\rangle$ and compute $\langle\Phi|X|\Phi\rangle/\langle\Phi|Z|\Phi\rangle$. Although from Eq. (3.10) we know that variances of these two quantities is bounded from above, we do not yet have a bound on the variance of the ratio of them. The purpose of this subsection is to address this point.

We define the error $\mathcal{E}(X)$ by

$$\mathcal{E}(X) \quad = \quad \frac{\langle\Phi|X|\Phi\rangle}{\mathrm{Tr}\ Z} - \frac{\langle\Phi|Z|\Phi\rangle}{\mathrm{Tr}\ Z}\frac{\mathrm{Tr}\ X}{\mathrm{Tr}\ Z}. \tag{3.20}$$

Obviously, because of $E[\langle\Phi|Z|\Phi\rangle] = \mathrm{Tr}\ Z$ and $E[\langle\Phi|X|\Phi\rangle] = \mathrm{Tr}\ X = \mathrm{Tr}\ ZY$ we have

$$\mathrm{E}[\mathcal{E}(X)] \quad = \quad 0. \tag{3.21}$$

As in the case of the variance of the thermal state, each quantity that appears in Eq. (3.20) can take almost arbitrary values (depending on β and the dimension D). Therefore, we have to compare the variance $\mathrm{Var}(\mathcal{E}(X))$ with the order-of-magnitude of the terms that appear in Eq. (3.20).

The mean difference, that is, the average absolute difference, between the two terms in Eq. (3.20) is bounded by

$$\begin{aligned}\mathrm{MD}(\mathcal{E}(X)) \equiv \mathrm{E}[|\mathcal{E}(X)|] \quad &\leq \quad \frac{\mathrm{E}[\langle\Phi|X|\Phi\rangle]}{\mathrm{Tr}\ Z} + \frac{\mathrm{E}[\langle\Phi|Z|\Phi\rangle]}{\mathrm{Tr}\ Z}\frac{\mathrm{Tr}\ X}{\mathrm{Tr}\ Z} \\ &= \quad 2\frac{\mathrm{Tr}\ ZY}{\mathrm{Tr}\ Z} = 2\langle Y\rangle \leq 2\|Y\|,\end{aligned} \tag{3.22}$$

where $\|Y\| = \max_\psi |\langle\psi|Y|\psi\rangle|$ is the largest (in absolute value) eigenvalue of Y. From Eq. (3.22) it follows that if $\langle Y\rangle = 0$, the mean difference of $\mathcal{E}(X) = 0$. In general, Eq. (3.22) shows that the "scale" of the error $\mathcal{E}(X)$ is set by $\|Y\|$ which is independent of β and, for most applications, a linear function of the system size N.

The variance of the error $\mathcal{E}(X)$ is given by

$$\begin{aligned}\mathrm{Var}(\mathcal{E}(X)) =& \frac{\mathrm{E}[\langle\Phi|X|\Phi\rangle^2]}{(\mathrm{Tr}\ Z)^2} + \frac{\mathrm{E}[\langle\Phi|Z|\Phi\rangle^2]}{(\mathrm{Tr}\ Z)^2}\left(\frac{\mathrm{Tr}\ ZY}{\mathrm{Tr}\ Z}\right)^2 \\ &- 2\frac{\mathrm{E}[\langle\Phi|X|\Phi\rangle\langle\Phi|Z|\Phi\rangle]}{(\mathrm{Tr}\ Z)^2}\frac{\mathrm{Tr}\ ZY}{\mathrm{Tr}\ Z} \\ =& \frac{\mathrm{Var}(\langle\Phi|X|\Phi\rangle)}{(\mathrm{Tr}\ Z)^2} + \frac{\mathrm{Var}(\langle\Phi|Z|\Phi\rangle)}{(\mathrm{Tr}\ Z)^2}\left(\frac{\mathrm{Tr}\ ZY}{\mathrm{Tr}\ Z}\right)^2 \\ &+ 2\frac{(\mathrm{Tr}\ ZY)\,(\mathrm{Tr}\ Z) - \mathrm{E}[\langle\Phi|X|\Phi\rangle\langle\Phi|Z|\Phi\rangle]}{(\mathrm{Tr}\ Z)^2}\frac{\mathrm{Tr}\ ZY}{\mathrm{Tr}\ Z},\end{aligned} \tag{3.23}$$

which upon using the result

$$\begin{aligned}\mathrm{E}[\langle\Phi|X|\Phi\rangle\langle\Phi|Z|\Phi\rangle] &= \sum_{a,p,b,q=1}^{D}\mathrm{E}[\xi_a^*\xi_p\xi_b^*\xi_q]\langle a|X|p\rangle\langle b|Z|q\rangle \\ &= (\mathrm{Tr}\ X)\,(\mathrm{Tr}\ Z)+\mathrm{Tr}\ XZ \\ &= (\mathrm{Tr}\ ZY)\,(\mathrm{Tr}\ Z)+\mathrm{Tr}\ e^{-2\beta H}Y \\ &= (\mathrm{Tr}\ ZY)\,(\mathrm{Tr}\ Z)+\mathrm{Tr}\ Z^2Y, \end{aligned} \tag{3.24}$$

and using Eq. (3.13) and Eq. (3.14) simplifies to

$$\begin{aligned}\mathrm{Var}(\mathcal{E}(X)) &= \frac{\mathrm{Tr}\ (ZY)^2}{(\mathrm{Tr}\ Z)^2}+\frac{(\mathrm{Tr}\ Z^2)}{(\mathrm{Tr}\ Z)^2}\left(\frac{\mathrm{Tr}\ ZY}{\mathrm{Tr}\ Z}\right)^2-2\frac{\mathrm{Tr}\ ZY}{\mathrm{Tr}\ Z}\frac{\mathrm{Tr}\ Z^2Y}{\mathrm{Tr}\ Z} \\ &= \frac{\mathrm{Tr}\ Z^2}{(\mathrm{Tr}\ Z)^2}\left\{\frac{\mathrm{Tr}\ (ZY)^2}{\mathrm{Tr}\ Z^2}+\left(\frac{\mathrm{Tr}\ ZY}{\mathrm{Tr}\ Z}\right)^2-2\frac{\mathrm{Tr}\ ZY}{\mathrm{Tr}\ Z}\frac{\mathrm{Tr}\ Z^2Y}{\mathrm{Tr}\ Z^2}\right\}. \end{aligned} \tag{3.25}$$

It is easy to find an upper bound for the terms in the curly brackets. We have

$$\left|\frac{\mathrm{Tr}\ (ZY)^2}{\mathrm{Tr}\ Z^2}+\left(\frac{\mathrm{Tr}\ ZY}{\mathrm{Tr}\ Z}\right)^2-2\frac{\mathrm{Tr}\ ZY}{\mathrm{Tr}\ Z}\frac{\mathrm{Tr}\ Z^2Y}{\mathrm{Tr}\ Z^2}\right|\leq 4\|Y\|^2, \tag{3.26}$$

and hence we find

$$\mathrm{Var}(\mathcal{E}(X)) \leq 4\|Y\|^2e^{-2\beta(F(2\beta)-F(\beta))}, \tag{3.27}$$

showing that the error $\mathcal{E}(X)$ vanishes exponentially with the system size N.

3.2.3 Approximate Estimates

A simple but less rigorous method to estimate averages and variances is to make use of the multivariate Taylor expansion for the average

$$\mathrm{E}\left[\frac{x}{y}\right]\approx\frac{\mathrm{E}[x]}{\mathrm{E}[y]}-\frac{\mathrm{Cov}[x,y]}{\mathrm{E}^2[y]}+\frac{\mathrm{E}[x]\mathrm{Var}[y]}{\mathrm{E}^3[y]}, \tag{3.28}$$

where $\mathrm{Cov}[x,y]=\mathrm{E}[xy]-\mathrm{E}[x]\mathrm{E}[y]$ and a similar approximation for the variance

$$\mathrm{Var}\left[\frac{x}{y}\right]\approx\frac{\mathrm{Var}[x]}{\mathrm{E}^2[y]}-2\frac{\mathrm{E}[x]\mathrm{Cov}[x,y]}{\mathrm{E}^3[y]}+\frac{\mathrm{E}^2[x]\mathrm{Var}[y]}{\mathrm{E}^4[y]}. \tag{3.29}$$

The advantage of this method is that it directly connects to what is done in the simulation: we generate a Gaussian random state $|\Phi>$ and compute ratios

$$R(Y,Z)\equiv\frac{\langle\Phi|Z^{1/2}YZ^{1/2}|\Phi\rangle}{\langle\Phi|Z^{1/2}Z^{1/2}|\Phi\rangle}, \tag{3.30}$$

where $Z = e^{-\beta H}$ and $Y = Y^\dagger$ is a physical quantity of interest. From Eq. (3.24) we have $\mathrm{Cov}[\langle\Phi|X|\Phi\rangle, \langle\Phi|Z|\Phi\rangle] = \mathrm{Tr}\ Z^2Y$ and hence it follows that

$$\begin{aligned} \mathrm{E}\left[\frac{\langle\Phi|X|\Phi\rangle}{\langle\Phi|Z|\Phi\rangle}\right] &\approx \frac{\mathrm{Tr}\ ZY}{\mathrm{Tr}\ Z} - \frac{\mathrm{Tr}\ Z^2Y}{(\mathrm{Tr}\ Z)^2} + \frac{\mathrm{Tr}\ ZY}{\mathrm{Tr}\ Z}\frac{\mathrm{Var}[\langle\Phi|Z|\Phi\rangle]}{(\mathrm{Tr}\ Z)^2} \\ &= \frac{\mathrm{Tr}\ ZY}{\mathrm{Tr}\ Z} - \frac{\mathrm{Tr}\ Z^2Y}{(\mathrm{Tr}\ Z)^2} + \frac{\mathrm{Tr}\ ZY}{\mathrm{Tr}\ Z}\frac{\mathrm{Tr}\ Z^2}{(\mathrm{Tr}\ Z)^2}. \end{aligned} \tag{3.31}$$

Previously, we have already shown that the second and third term in Eq. (3.31) vanish exponentially with the system size, hence for large D we have

$$\mathrm{E}\left[\frac{\langle\Phi|X|\Phi\rangle}{\langle\Phi|Z|\Phi\rangle}\right] \approx \frac{\mathrm{Tr}\ ZY}{\mathrm{Tr}\ Z} = \langle Y\rangle, \tag{3.32}$$

as expected. Similarly, for the variance we have

$$\begin{aligned} \mathrm{Var}\left[\frac{\langle\Phi|X|\Phi\rangle}{\langle\Phi|Z|\Phi\rangle}\right] &\approx \frac{\mathrm{Var}[\langle\Phi|X|\Phi\rangle]}{(\mathrm{Tr}\ Z)^2} - 2\frac{\mathrm{Tr}\ ZY}{\mathrm{Tr}\ Z}\frac{\mathrm{Tr}\ Z^2Y}{(\mathrm{Tr}\ Z)^2} + \left(\frac{\mathrm{Tr}\ ZY}{\mathrm{Tr}\ Z}\right)^2\frac{\mathrm{Var}[\langle\Phi|Z|\Phi\rangle]}{(\mathrm{Tr}\ Z)^2} \\ &= \frac{\mathrm{Tr}\ (ZY)^2}{(\mathrm{Tr}\ Z)^2} - 2\frac{\mathrm{Tr}\ ZY}{\mathrm{Tr}\ Z}\frac{\mathrm{Tr}\ Z^2Y}{(\mathrm{Tr}\ Z)^2} + \left(\frac{\mathrm{Tr}\ ZY}{\mathrm{Tr}\ Z}\right)^2\frac{\mathrm{Tr}\ Z^2}{(\mathrm{Tr}\ Z)^2} \\ &= \frac{\mathrm{Tr}\ Z^2}{(\mathrm{Tr}\ Z)^2}\left\{\frac{\mathrm{Tr}\ (ZY)^2}{\mathrm{Tr}\ Z^2} - 2\frac{\mathrm{Tr}\ ZY}{\mathrm{Tr}\ Z}\frac{\mathrm{Tr}\ Z^2Y}{\mathrm{Tr}\ Z^2} + \left(\frac{\mathrm{Tr}\ ZY}{\mathrm{Tr}\ Z}\right)^2\right\}, \end{aligned} \tag{3.33}$$

which is identical to Eq. (3.25). By the same arguments as those used in Section 3.2.2, we can argue that the the approximate expression Eq. (3.33) vanishes exponentially with the system size D. Summarizing, our rigorous and approximate treatment lead to the same conclusions.

3.2.4 Autocorrelation Function

As an illustrative example, we consider here the signal recorded in electron spin resonance (ESR), primarily because it is a standard example of linear response theory. According to linear response theory, the ESR signal is related to the Fourier transform of the autocorrelation correlation function [59]. The ESR signal averaged over a period $2T$ is proportional to [see Ref. [59], Eq. (7.16)]

$$C^T(\omega) \equiv \frac{1}{2T}\int_{-T}^{T}\frac{\mathrm{Tr}\, e^{-\beta H}C(t)}{\mathrm{Tr}\, e^{-\beta H}}\cos\omega t\, dt, \tag{3.34}$$

where

$$C(t) = \frac{1}{2}\{e^{itH}M^x e^{-itH}, M^x\}. \tag{3.35}$$

We set

$$X(\omega) = e^{-\beta H/2} Y(\omega) e^{-\beta H/2},$$

and

$$Y(\omega) = \frac{1}{2T} \int_{-T}^{T} C(t) \cos \omega t \, dt. \tag{3.36}$$

Because $Y(\omega) = Y^{\dagger}(\omega)$ and $X(\omega) = X^{\dagger}(\omega)$, we can use Eq. (3.27) and find

$$\mathrm{Var}(\mathcal{E}(X(\omega))) \leq 4 \|Y(\omega)\|^2 e^{-2\beta(F(2\beta)-F(\beta))}, \tag{3.37}$$

showing that the variance of $\mathcal{E}(X(\omega))$ vanishes exponentially with the system size N.

Chapter 4

Random State Approach: II

In the previous chapter, we have discussed the use of the random Gaussian state to calculate the expectation value of hermitian operator X. In this chapter, we introduce a different but related random state approach to approximate Tr X. The main material of this chapter is based on the Ref. [22].

4.1 Theory

The trace of a matrix A acting on a D-dimensional Hilbert space spanned by an orthonormal set of states $\{|\phi_n\rangle\}$ is given by

$$\mathrm{Tr}A = \sum_{n=1}^{D} \langle\phi_n|A|\phi_n\rangle \,. \tag{4.1}$$

Note that according to Eq. (4.1) we have $\mathrm{Tr}1 = D$. If D is very large ,one might think of approximating Eq. (4.1) by sampling over a subset of $K (K \ll D)$ "important" basis vector. The problem with this approach is that the notion "important" may be

very model dependent. Therefore, it is better to sample in a different manner. We construct a random vector $|\Psi\rangle$ by choosing D complex random numbers, so

$$|\Psi\rangle = \sum_{n=1}^{D} c_n |\phi_n\rangle , \tag{4.2}$$

and we calculate

$$\langle\Psi|A|\Psi\rangle = \sum_{n,\ m=1}^{D} c_m^* c_n \langle\phi_m|A|\phi_n\rangle . \tag{4.3}$$

If we sample over S realization of the random vectors $\{\Psi\}$ and calculate the average, we obtain

$$\frac{1}{S}\sum_{p\ =1}^{S} \langle\Psi_p|A|\Psi_p\rangle = \frac{1}{S}\sum_{p\ =1}^{S}\sum_{n,\ m=1}^{D} c_{m,p}^* c_{n,p} \langle\phi_m|A|\phi_n\rangle . \tag{4.4}$$

Assuming that there is no correlation between the random numbers in different realizations, and that the random numbers are drawn from an even and symmetric probability distribution, we have [22]

$$\lim_{S\to\infty} \frac{1}{S}\sum_{p\ =1}^{S} c_{m,p}^* c_{n,p} = E(|c|^2)\delta_{m,n}, \tag{4.5}$$

where $E(|c|^2)$ denote the expectation value with respect to the probalility distribution used to generate the $c_{n,p}$'s. It follows immediately that

$$\lim_{S\to\infty} \frac{1}{S}\sum_{p\ =1}^{S} \langle\Psi_p|A|\Psi_p\rangle = E(|c|^2)\sum_{n\ =1}^{D} \langle\phi_n|A|\phi_n\rangle = E(|c|^2)\mathbf{Tr}A, \tag{4.6}$$

showing that we can compute the trace of A by sampling over random states $\{\Psi_p\}$.

According to the central limit theorem, for a large but finite S, we have

$$\frac{1}{S}\sum_{p\ =1}^{S} c_{m,p}^* c_{n,p} = E(|c|^2)\delta_{m,n} + O(\frac{1}{\sqrt{S}}), \tag{4.7}$$

meaning that the statistical error on the trace vanishes like $1/\sqrt{S}$, which is not surprising. What is surprising is that one can prove a much stronger result as follow. Let us first normalize the $c_{n,p}$'s so that, for all p

$$\sum_{n=1}^{D} |c_{n,p}|^2 = 1. \tag{4.8}$$

This innocent looking step has far reaching consequences. First we note that the normalization renders the method exact in the (rather trivial) case when the matrix

A is proportional to the unit matrix. The price we pay for this is that for fixed p, the $c_{n,p}$ are now correlated, but that does not cause problems [22]. Second it follows that $E(|c^2|) = 1/D$.

Obviously the error can be written as

$$\mathrm{Tr}A - \frac{D}{S}\sum_{p=1}^{S}\langle\psi_p|A|\psi_p\rangle = \mathrm{Tr}RA, \tag{4.9}$$

where

$$R_{m,n} \equiv \delta_{m,n} - \frac{D}{S}\sum_{p=1}^{S} c^*_{m,p}c_{n,p}, \tag{4.10}$$

is a traceless (due to Eq. (4.8)) Hermitian matrix of random numbers. We put $X = \mathrm{Tr}RA$ and compute $E(|X|^2)$. For a uniform distribution of the $c_{n,p}$'s on the hypersphere defined by $\sum_{n=1}^{D}|c_{n,p}|^2 = 1$ the expression simplifies considerably and we find

$$E\left(|\mathrm{Tr}RA|^2\right) = \frac{D\mathrm{Tr}A^\dagger A - |\mathrm{Tr}A|^2}{S(D+1)}, \tag{4.11}$$

an exact expression for the variance in terms of the sample size S, the dimension D of the matrix A and the (unknown) constants $\mathrm{Tr}A^\dagger A$ and $|\mathrm{Tr}A|$ [22].

Invoking a generalization of Markov's inequality [60]

$$\mathrm{P}(|X|^2 \geq a) \leq \frac{E(|X|^2)}{a} \quad ; \quad \forall\, a > 0, \tag{4.12}$$

where $\mathrm{P}(Q)$ denotes the probability for the statement Q to be true. We find that the probability that $|\mathrm{Tr}RA|^2$ exceeds a fraction a of $|\mathrm{Tr}A|^2$ is bounded by

$$\mathrm{P}\left(\frac{|\mathrm{Tr}RA|^2}{|\mathrm{Tr}A|^2} \geq a\right) \leq \frac{1}{a\,S\,(D+1)}\frac{D\mathrm{Tr}A^\dagger A - |\mathrm{Tr}A|^2}{|\mathrm{Tr}A|^2} \quad ; \quad \forall\, a > 0, \tag{4.13}$$

or, in other words, the relative statistical error e_A on the estimator of the trace of A is given by

$$e_A \equiv \sqrt{\frac{D\mathrm{Tr}A^\dagger A - |\mathrm{Tr}A|^2}{S(D+1)|\mathrm{Tr}A|^2}}, \tag{4.14}$$

if $|\mathrm{Tr}A| > 0$. We see that $e_A = 0$ if A is proportional to a unit matrix. From (4.14) it follows that, in general, we may expect e_A to vanish with the square root of SD. The prefactor is a measure for the relative spread of the eigenvalues of A and is obviously model dependent. The dependence of e_A on S, D and the spectrum of A is corroborated by the numerical results presented below.

It is also of interest to examine the effect of not normalizing the $c_{n,p}$'s. A calculation similar to the one that lead to the above results yields

$$e_A = \sqrt{\frac{\mathrm{Tr}A^\dagger A}{S|\mathrm{Tr}A|^2}}. \tag{4.15}$$

Clearly this bound is less sharp and does not vanish if A is proportional to a unit matrix.

4.2 Application

It is an important problem in quantum physics to calculate the distribution of eigenvalues of large matrices. This distribution determines the thermodynamics properties of system and is related to the single-particle density of states (DOS) or Green's function. The most direct method to compute DOS, i.e., all the eigenvalues, is to diagonalize the Hamiltonian of the system. However, the dimension of Hamiltonian grows exponentially with the number of particles in a Hilbert space. A collection of only 50 spin-1/2 particles, each of which could be identified by two complex amplitudes were it isolated, requires a total of 2^{50} complex amplitudes for its state to be specified completely. This scaling behavior limits our ability to study these quantum physics problems. Since it is obviously not possible to even describe the state of anything but the smallest quantum systems, one must resort to various approximation techniques to calculate properties of interest.

There has been considerable interest in developing "fast" algorithms to compute the DOS and other similar quantities [22, 29, 58, 61–72]. A common feature of these fast algorithms is that they solve the TDSE for a sample of randomly chosen initial states. The efficiency of this approach as a whole relies on the hypothesis, suggested by the central limit theorem, that satisfactory accuracy can be achieved by using a small sample of initial states.

The distribution of eigenvalues or density of states (DOS) of a quantum system is defined as

$$\mathcal{D}(\epsilon) = \sum_{n=1}^{D} \delta(\epsilon - E_n) = \frac{1}{2\pi} \int_{-\infty}^{\infty} e^{it\epsilon}\, \mathrm{Tr}\, e^{-itH}\, dt, \tag{4.16}$$

where H is the hamiltonian of the system and n runs over all the eigenvalues of H. The DOS contain important information about the equilibrium properties of the system. For instance the partition function, the energy, and the heat capacity *etc.*.

As explained in Sections 4.1, the trace in integral (4.16) can be estimated by sampling over random vectors. For the discussion below it is convenient to define a

DOS per sample by

$$d_p(\epsilon) \equiv \frac{1}{2\pi} \int_{-\infty}^{\infty} e^{it\epsilon} \left\langle \Psi_p | e^{-itH} \Psi_p \right\rangle dt, \tag{4.17}$$

where the subscript p labels the particular realization of the random state $|\Psi_p\rangle$. The DOS is then given by

$$\mathcal{D}(\epsilon) = \lim_{S\to\infty} \frac{1}{S} \sum_{p=1}^{S} d_p(\epsilon). \tag{4.18}$$

Schematically the algorithm to compute $d_p(\epsilon)$ consists of the following steps:

1. Generate a random state $|\Psi_p(0)\rangle$, and set $t = 0$.
2. Copy this state to $|\Psi_p(t)\rangle$.
3. Calculate $\langle\Psi_p(0)|\Psi_p(t)\rangle$ and store the result.
4. Solve the TDSE for a small time step τ, replacing $|\Psi_p(t)\rangle$ by $|\Psi_p(t+\tau)\rangle$.
5. Repeat N times from Step 3.
6. Perform a Fourier transform on the tabulated result and store $d_p(\epsilon)$.

4.2.1 DOS of Clean Graphene

We consider clean graphene described by the tight-binding Hamiltonian

$$H = -\sum_{i,j} t_{i,j} c_i^\dagger c_j + \sum_i v_i c_i^\dagger c_i, \tag{4.19}$$

where the first sum is taken over nearest neighbors and the second one is over the on-site potential.

The analytical expression of the density of states of a clean graphene (ignoring the next-nearest neighbor interaction t' and the on-site energy) was given in Ref. [73] as

$$\rho(E) = \begin{cases} \frac{2E}{t^2\pi^2} \frac{1}{\sqrt{F(E/t)}} \mathbf{K}\left(\frac{4E/t}{F(E/t)}\right), & 0 < E < t, \\ \\ \frac{2E}{t^2\pi^2} \frac{1}{\sqrt{4E/t}} \mathbf{K}\left(\frac{F(E/t)}{4E/t}\right), & t < E < 3t, \end{cases} \tag{4.20}$$

where $F(x)$ is given by

$$F(x) = (1+x)^2 - \frac{\left(x^2-1\right)^2}{4}, \tag{4.21}$$

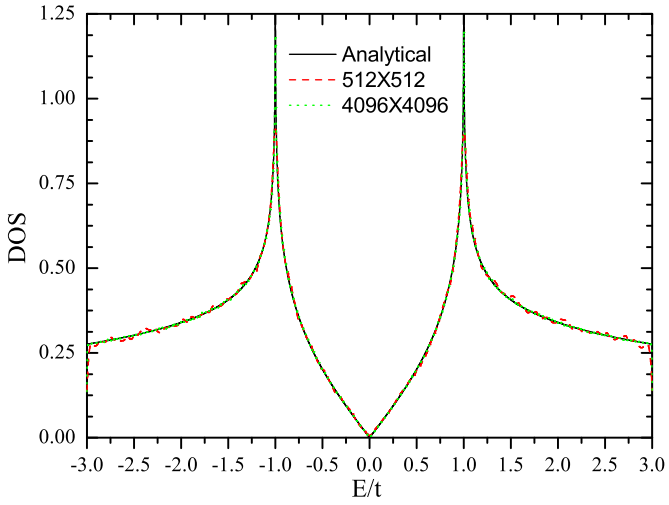

Figure 4.1: (Color online) Comparison of the analytical DOS (in units of $1/t$, black solid) with the numerical results of a sample contains 512×512 (red dash) or 4096×4096 (green dot) carbon atoms.

and $\mathbf{K}(m)$ is the elliptic integral of first kind:

$$\mathbf{K}(m) = \int_0^1 dx \left[\left(1-x^2\right)\left(1-mx^2\right)\right]^{-1/2}. \tag{4.22}$$

In Fig. 4.1, we compare the analytical expression Eq. (4.20) with the numerical results of the density of states for clean graphene. One can clearly see that these numerical results fit very well the analytical expression, and the difference between the numerical and analytical results becomes smaller when using larger sample size (see the difference of a sample with 512×512 or 4096×4096 in Fig. 4.1). In fact, the local density of states of a sample containing 4096×4096 is approximately the same as the density of states of infinite clean graphene, which indicates the high accuracy of the algorithm.

4.2.2 DOS of Spin $1/2$ Chains

Open spin chains of L sites described by the Hamiltonian

$$H = -J\sum_{i=1}^{L-1}(\sigma_i^x\sigma_{i+1}^x + \Delta\sigma_i^y\sigma_{i+1}^y) - h\sum_{i=1}^{L}\sigma_i^z, \tag{4.23}$$

where σ_i^x, σ_i^y, and σ_i^z denote the Pauli matrices and J, Δ and h are model parameters, can be solved exactly. They can be reduced to diagonal form by means of the Jordan-Wigner transformation [74]. We have

$$H = \sum_{i,j=1}^{L} \left[c_i^+ A_{i,j} c_j \; + \frac{1}{2} \left(c_i^+ B_{i,j} c_j^+ + c_j \; B_{j,i}^* c_i \; \right) \right] + hL, \tag{4.24}$$

where c_i^+ and c_i are spin-less fermion operators and

$$A_{i,j} = -J(1+\Delta)(\delta_{i,j-1} + \delta_{i-1,j}) - 2h\delta_{i,j}, \tag{4.25}$$

$$B_{i,j} = -J(1-\Delta)(\delta_{i,j-1} - \delta_{i-1,j}), \tag{4.26}$$

are $L \times L$ matrices. By further canonical transformation this Hamiltonian can be written as

$$H = \sum_{k=1}^{L} \Lambda_k \left(n_k - \frac{1}{2} \right) + \frac{1}{2} \mathrm{Tr} A + hL, \tag{4.27}$$

where n_k is the number operator of state k and the Λ_k's are given by the solution of the eigenvalue equation

$$(A-B)(A+B)\phi_k = \Lambda_k^2 \, \phi_k. \tag{4.28}$$

In the general case this eigenvalue problem of the $L \times L$ Hermitian matrix $(A-B)(A+B)$ is most easily solved numerically. We confine ourselves to two limiting cases: The XY model ($\Delta = 1$) and the Ising model in a transverse field ($\Delta = 0$).

Our results are in unit of J and take $h = 0$, except for the Ising model in a transverse field, where $h = 0.75J$. In Fig. 4.2, we show a typical result for the density of states of the XY model and the Ising model in a transverse field with $L = 15$ spins and using $S = 20$ samples. The results agree very well with those obtained by solving Eq. (4.28).

4.2.3 Optical Conductivity of Graphene

Now, we are using the random state approach to investigate the optical conductivity of Graphene. It is known to us that Kubo's formula for the optical conductivity can be expressed as [59]

$$\begin{aligned} \sigma_{\alpha\beta}(\omega) \;\; &= \;\; \lim_{\varepsilon \to 0^+} \frac{1}{(\omega + i\varepsilon)\,\Omega} \{ -i \langle [P_\alpha, J_\beta] \rangle \\ &\quad + \int_0^\infty e^{i(\omega + i\varepsilon)t} dt \;\; \langle [J_\alpha(t), J_\beta] \rangle \}, \end{aligned} \tag{4.29}$$

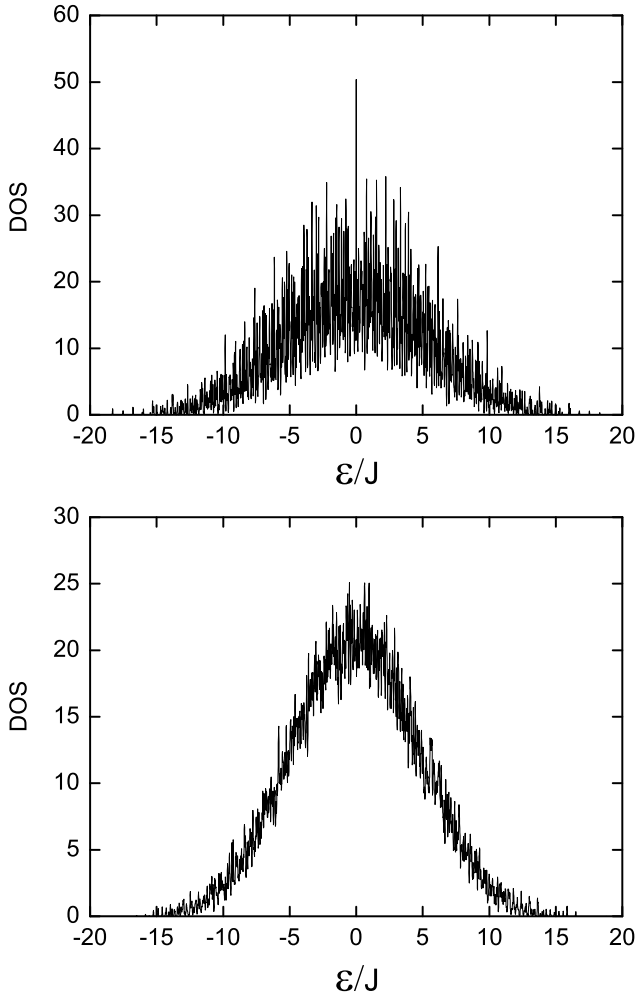

Figure 4.2: The density of states (DOS) as obtained from the real-time algorithm for spin chains of length $L = 15$ and for $S = 20$ random initial states. TOP: XY model with $h = 0.0J$, Bottom: Ising model in a transverse field with $h = 0.75J$.

where P is the polarization operator

$$P = e\sum_i \mathbf{r}_i c_i^+ c_i, \tag{4.30}$$

and J is the current operator

$$J = \dot{P} = e\sum_i \dot{\mathbf{r}}_i c_i^+ c_i = \frac{i}{\hbar}\left[H, P\right]. \tag{4.31}$$

For a generic tight binding Hamiltonian, the current operator can be written as

$$J = -\frac{ie}{\hbar}\sum_{i,j} t_{ij}\left(\mathbf{r}_j - \mathbf{r}_i\right) c_i^+ c_j, \tag{4.32}$$

and

$$[P_\alpha, J_\beta] = -\frac{ie^2}{\hbar}\sum_{i,j} t_{ij}\left[\left(\mathbf{r}_i - \mathbf{r}_j\right)_\alpha \left(\mathbf{r}_j - \mathbf{r}_i\right)_\beta\right] c_i^+ c_j. \tag{4.33}$$

The ensemble average in Eq. (4.29) is over the Gibbs distribution, and the electric field is given by $\mathbf{E}(t) = \mathbf{E}_0 \exp(i\omega + \varepsilon)t$ (ε is a small parameter introduced in order that $\mathbf{E}(t) \to 0$ for $t \to -\infty$). In graphene, P and J are two-dimensional vectors, and Ω is replaced by the area of the sample S.

In general, the real part of the optical conductivity contains two parts, the Drude weight D ($\omega = 0$) and the regular part ($\omega \neq 0$). We omit the calculation of the Drude weight, and focus on the regular part. For non-interacting electrons, the regular part is [75, 76]

$$\begin{aligned} \mathrm{Re}\sigma_{\alpha\beta}(\omega) &= \lim_{\varepsilon\to 0^+} \frac{e^{-\beta\hbar\omega} - 1}{\hbar\omega\Omega} \int_0^\infty e^{-\varepsilon t} \sin\omega t \\ &\quad \times 2\mathrm{Im}\left\langle f(H) J_\alpha(t) \left[1 - f(H)\right] J_\beta \right\rangle dt, \end{aligned} \tag{4.34}$$

where $\beta = 1/k_B T$. $f(H)$ is the Fermi-Dirac distribution operator

$$f(H) = \frac{1}{e^{\beta(H-\mu)} + 1}, \tag{4.35}$$

with chemical potential μ.

In the numerical calculations, the average in Eq. (4.34) is performed over a random phase superposition of all the basis states in the real space, i.e., the same initial state $|\varphi(0)\rangle$ in calculation of DOS. The Fermi distribution operator $f(H)$ and $1 - f(H)$ can be obtained by the standard Chebyshev polynomial decomposition.

In general, a function $f(x)$ whose values are in the range $[-1, 1]$ can be expressed as

$$f(x) = \frac{1}{2}c_0 T_0(x) + \sum_{k=1}^{\infty} c_k T_k(x), \tag{4.36}$$

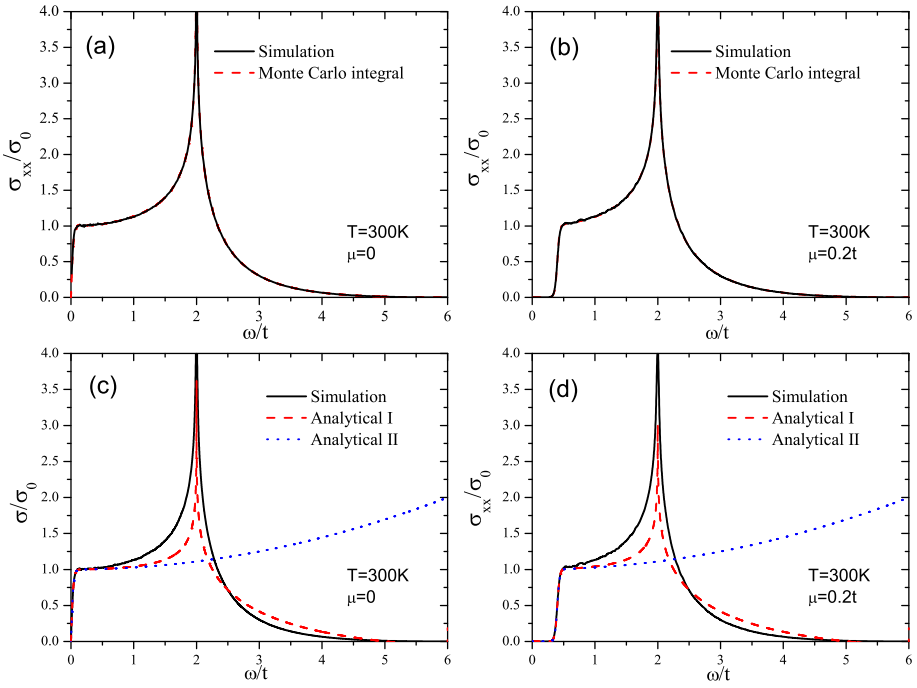

Figure 4.3: (Color online) Comparison of the numerically calculated optical conductivity. The parameters are $\mu = 0$ or 0.2t, T=300K with Eq. (4.47) (Monte carlo integral), Eq. (4.49) (analytical I), and Eq. (4.50) (analytical II). The size of the system is M=N=8192.

where $T_k(x) = \cos(k \arccos x)$ and the coefficients c_k are

$$c_k = \frac{2}{\pi} \int_{-1}^{1} \frac{dx}{\sqrt{1-x^2}} f(x) T_k(x). \tag{4.37}$$

Let $x = \cos\theta$, then $T_k(x) = T_k(\cos\theta) = \cos k\theta$, and

$$\begin{aligned} c_k &= \frac{2}{\pi} \int_0^{\pi} f(\cos\theta) \cos k\theta d\theta \\ &= \mathrm{Re}\left[\frac{2}{N} \sum_{n=0}^{N-1} f\left(\cos\frac{2\pi n}{N}\right) e^{\frac{2\pi i n k}{N}} \right], \end{aligned} \tag{4.38}$$

which can be calculated by the fast Fourier transform.

For the operators $f = ze^{-\beta H}/\left(1 + ze^{-\beta H}\right)$, where $z = \exp(\beta\mu)$ is the fugacity, we normalize H such that $\widetilde{H} = H/||H||$ has eigenvalues in the range $[-1, 1]$ and put $\widetilde{\beta} = \beta ||H||$. Then

$$f\left(\widetilde{H}\right) = \frac{ze^{-\widetilde{\beta}\widetilde{H}}}{1 + ze^{-\widetilde{\beta}\widetilde{H}}} = \sum_{k=0}^{\infty} c_k T_k\left(\widetilde{H}\right), \tag{4.39}$$

where c_k are the Chebyshev expansion coefficients of

$$f(x) = \frac{ze^{-\widetilde{\beta}x}}{1 + ze^{-\widetilde{\beta}x}}, \tag{4.40}$$

and the Chebyshev polynomial $T_k\left(\widetilde{H}\right)$ can be obtained by the recursion relations

$$T_{k+1}\left(\widetilde{H}\right) - 2\widetilde{H} T_k\left(\widetilde{H}\right) + T_{k-1}\left(\widetilde{H}\right) = 0, \tag{4.41}$$

with

$$T_0\left(\widetilde{H}\right) = 1, T_1\left(\widetilde{H}\right) = \widetilde{H}. \tag{4.42}$$

By introducing the three wave functions [29]

$$|\varphi_1(t)\rangle_x = e^{-\frac{iHt}{\hbar}} [1 - f(H)] J_x |\varphi\rangle, \tag{4.43}$$

$$|\varphi_1(t)\rangle_y = e^{-\frac{iHt}{\hbar}} [1 - f(H)] J_y |\varphi\rangle, \tag{4.44}$$

$$|\varphi_2(t)\rangle = e^{-\frac{iHt}{\hbar}} f(H) |\varphi\rangle, \tag{4.45}$$

we get all elements of the regular part of $\mathrm{Re}\sigma_{\alpha\beta}(\omega)$:

$$\begin{aligned} \mathrm{Re}\sigma_{\alpha\beta}(\omega) &= \lim_{\varepsilon \to 0^+} \frac{e^{-\beta\hbar\omega} - 1}{\hbar\omega\Omega} \int_0^{\infty} e^{-\varepsilon t} \sin\omega t \\ &\quad \times \left[2\mathrm{Im}\ \langle \varphi_2(t) | J_\alpha | \varphi_1(t) \rangle_\beta \right] dt. \end{aligned} \tag{4.46}$$

Figs. 4.3 (a) and (b) show numerical results of Eq. (4.46) and the Monte carlo integral of the optical conductivity over the first Brillouin zone [77]

$$\begin{aligned}
&\sigma_{\alpha\beta}(\omega) \\
&= \frac{1}{(\omega+i\varepsilon)}\frac{ig_s}{(2\pi)^2}\int_{1BZ} d^2k \sum_{s,s'=\pm} f_{s\cdot s'}(\mathbf{k})_{\alpha\beta}\frac{n_F\left[E^s(\mathbf{k})\right]-n_F\left[E^{s'}(\mathbf{k})\right]}{E^s(\mathbf{k})-E^{s'}(\mathbf{k})+\omega+i\delta} \\
&= \frac{1}{(\omega+i\varepsilon)}\frac{i}{2\pi^2}\int_{1BZ} d^2k \sum_{s,s'=\pm} f_{s\cdot s'}(\mathbf{k})_{\alpha\beta}\frac{n_F\left[E^s(\mathbf{k})\right]-n_F\left[E^{s'}(\mathbf{k})\right]}{\left[E^s(\mathbf{k})-E^{s'}(\mathbf{k})+\omega\right]^2+\delta^2} \\
&\times\left[E^s(\mathbf{k})-E^{s'}(\mathbf{k})+\omega-i\delta\right],
\end{aligned} \tag{4.47}$$

where

$$f_{ss'}(\mathbf{k})_{\alpha\beta} = \left|<\mathbf{k};s\left|\mathbf{j}_{\alpha\beta}\right|\mathbf{k};s'>\right|^2, \tag{4.48}$$

$s, s' = \pm$ correspond to the conduction and valence bands respectively.

In Figs. 4.3 (c) and (d), we compare our numerical results to the analytical results obtained in Refs. [12, 78, 79], where the real part of the conductivity in the visible region has the form [12]

$$\begin{aligned}
\mathrm{Re}\sigma_{xx} &= \sigma_0\left[\frac{\pi t^2a^2}{8A_c\hbar\omega}\rho\left(\frac{\hbar\omega}{2}\right)\left(18-\frac{\hbar^2\omega^2}{t^2}\right)+\frac{\hbar^2\omega^2}{4!2^4t^2}\right] \\
&\left(\tanh\frac{\hbar\omega+2\mu}{4k_BT}+\tanh\frac{\hbar\omega-2\mu}{4k_BT}\right),
\end{aligned} \tag{4.49}$$

with the minimum conductivity $\sigma_0 = \pi e^2/2h$. Around $\omega = 0$ the real part of the conductivity can be simplified as [12, 78, 79]

$$\begin{aligned}
\mathrm{Re}\sigma_{xx} &= \sigma_0\left(\frac{1}{2}+\frac{1}{72}\frac{\hbar^2\omega^2}{t^2}\right) \\
&\left(\tanh\frac{\hbar\omega+2\mu}{4k_BT}+\tanh\frac{\hbar\omega-2\mu}{4k_BT}\right).
\end{aligned} \tag{4.50}$$

As we can see from Fig. 4.3, the numerical and analytical results match very well in the low frequency region, but not in the high frequence region. This is because the analytical expressions are partially based on the Dirac-cone approximation, i.e., the graphene energy bands are linearly dependent on the amplitude of the wave vector. It is exact for the calculations of the low-frequence optical conductivity, but not for high-frequence. Our numerical method does not use such an approximation and has

the same accuracy in the whole spectrum. Furthermore, our numerical results also show that the conductivity of $\mathrm{Re}\sigma_{xx}$ with $\mu = 0$ in the limit of $\omega = 0$ converges to the minimum conductivity σ_0 when the temperature $T \to 0$ [76].

4.3 Discussion and Conclusion

In the last two chapters, we used two different techniques to generate random number state.

(1) The $c_{n,p}$'s are obtained from a two-variable (real and imaginary part) Gaussian random number generator.

(2) A uniform random number generator produces $\{f_{n,p}\}$ and $\{g_{n,p}\}$ with $-1 \leq f_{n,p}, g_{n,p} \leq 1$. We then normalize the vector [22].

Both methods satisfy the basic requirements: $\S_1$ The random numbers are independent in different realizations. $\S_2$ The random numbers are drawn from an even and symmetric probability distribution. The first method is known to generate numbers which are distributed uniformly over the hyper-surface. But the second sample points out of a $2D$-dimensional hypercube and subsequently projects the vector onto a sphere, the points are not distributed uniformly over the surface of the unit hypersphere. Although the second method does not satisfy all the mathematical conditions that lead to the error (4.14), our numerical experiments with both generators give identical results, within statistical errors of course.

Chapter 5

Fingerprints of Disorder in Graphene

We present a systematic study of the electronic, transport and optical properties of disordered graphene including the next-nearest-neighbor hopping. We show that this hopping has a non-negligible effect on resonant scattering but is of minor importance for long-range disorder such as charged impurities, random potentials or hoppings induced by strain fluctuations. Different types of disorders can be recognized by their fingerprints appearing in the profiles of dc conductivity, carrier mobility, optical spectroscopy and Landau level spectrum. The minimum conductivity $4e^2/h$ found in the experiments is dominated by long-range disorder and the value of $4e^2/\pi h$ is due to resonant scatterers only.

This chapter was previously published as
P. Zhao, S. Yuan, M. I. Katsnelson, and H. De Raedt, Phys. Rev. B **92**, 045437 (2015).

5.1 Introduction

The dominant source of disorder which limits the transport and optical properties of graphene is still under debate. Different mechanisms have been proposed and investigated intensively, including charged impurities, random strain fluctuations and resonant scatterers (for reviews see Refs. [1, 2]). Early on, charged impurities (CI) have been recognized as the dominate disorders due to graphene's unusual linear carrier-density-dependent conductivity. However, this mechanism does not explain the experimental observations that the transport properties of certain samples are not sensitive to the substrate screening [80, 81]. On the other hand, strain fluctuations (SF) induced e.g. ripples can be alternative scattering mechanism [82]; they can be also responsible for charge inhomogeneities, that is, electron-hole puddles [83, 84]. There is experimental evidence, based on the correlation between the carrier mobility and the width of the resistance peak around charge neutrality, that the long-range disorder potential (LRDP) due to SF could be the dominant source of disorder in high-quality graphene on a substrate [85]. In addition, the SF modulate the electron hopping energies between different atomic sites, inducing the long-range disorder hopping (LRDH), leading to the appearance of the (pseudo) vector potential [2, 86]. Another common source of disorder are resonant scatterers (RS) such as chemical species like hydrogen or organic groups, which also lead to a sublinear carrier-density-dependent conductivity and a minimum conductivity plateau around the neutrality point [87, 88].

Besides the transport properties, an important part of our knowledge about the electronic properties derives from the optical spectroscopy measurements [1, 3]. Infrared spectroscopy experiments allow for the control of interband excitations by means of electrical gating [4, 89]. For doped pristine graphene with nonzero chemical potential μ_F, the optical conductivity is a step function $\sigma(\omega) = \sigma_0 \Theta(\omega - 2\mu_F)$ at zero temperature due to Pauli's exclusion principle. However, there are experimentally observed background contributions to the optical spectroscopy between $0 < \omega < 2\mu_F$ [4, 5], which are due to the extra intraband excitations introduced by disorder or many-body effects [4, 6–16].This opens the possibility to identify the source of disorder via the optical measurements.

Previous theoretical investigation of disorders are mainly based on models without considering the next-nearest-neighbor (NNN) hopping t'. The breakdown of electron-hole symmetry resulting from $t' \neq 0$ shifts the position of Dirac point from zero to $3t'$ [2, 90]. Recent quantum capacitance measurements indicate that the value of t' is about $0.3eV$ [91], consistent with the values obtained from the density functional calculations. It is generally thought that t' has relatively weak effects on the physical properties of graphene at low energies [2, 12, 90, 91]. In the present chapter, we study the electronic, transport and optical properties of graphene with different types of disorders including NNN. We show that t' has a negligible effect in combina-

tion with long-range disorder such as CI, LRDP and LRDH, but changes the physics dramatically when RS are present. Different sources of disorder can be identified via their fingerprints in the common measurable quantities, such as dc conductivity, carrier mobility, optical spectroscopy and Landau level spectrum *etc.* We will use these fingerprints to demonstrate the dominant disorder source in several well-known experimental measurements. This chapter is organized as follows. In section 5.2 we gives a description of the tight-binding Hamiltonian of single layer graphene including different types of disorders and NNN. In section 5.3 and 5.4, we discuss the effect of different disorders on the transport and optical properties of graphene. Then, we study the Landau level spectrum and quantum capacitance in the presence of perpendicular magnetic field in section 5.5. Finally, a brief discussion and conclusion, including a list of dominant disorder sources in several experiments, is given in section 5.6.

5.2 Model and Method

We consider disordered graphene described by the tight-binding (TB) Hamiltonian

$$H = -\sum_{i,j} t_{i,j} c_i^\dagger c_j - \sum_{i,j} t'_{i,j} c_i^\dagger c_j + \sum_i v_i c_i^\dagger c_i, \tag{5.1}$$

where the first sum is taken over nearest neighbors and the second one is over next-nearest neighbors.

For CI, we consider randomly distributed point-like charges at the center of a hexagon of the honeycomb lattice ($\mathbf{r}_k$)[92], which introduce the Coulomb energy at each site i

$$v_i = \sum_k \mathrm{sign}\,(k)\, e^2 / \left(\kappa |\mathbf{r}_i - \mathbf{r}_k|\right), \tag{5.2}$$

and the screening effect due to the substrate is taken into account by using the dielectric constant κ of the substrate. Here, according the values of sign (k) we consider three types of CI: (1) CI^0 for randomly distributed positive or negative potential caused by charges that the whole sample holds the electric neutrality, (2) CI^+ for only positive potential and (3) CI^- for only negative ones.

For LRDP, the on-site potential v_i follows a corrected Gaussian profile which varies smoothly on the scale of lattice constant as[16]

$$v_i = \sum_k U_k \exp[-|\mathbf{r}_i - \mathbf{r}_k|^2 / (2d^2)], \tag{5.3}$$

where $\mathbf{r}_k$ is the $k-th$ Gaussian centers which are randomly distributed on the lattice with probability p_v, U_k represents the strength of the local potential and is uniformly random in the range $[-\Delta_v, \Delta_v]$, and d is interpreted as the effective radius. We use

$\Delta_v = t$ and $d = 5a$ to represent the long-range Gaussian potential. Here $a \approx 1.42$Å is the carbon-carbon distance in the single-layer graphene.

The LRDH is introduced in a similar way as LRDP except that the nearest-neighbor hopping parameters are modified according a correlated Gaussian form via

$$t_{ij} = t + \sum_k T_k \exp[-|\mathbf{r}_i + \mathbf{r}_j - 2\mathbf{r}_k|^2 / \left(8d_t^2\right)], \tag{5.4}$$

where T_k, d_t and p_t have similar meanings as in LRDP, and we choose $\Delta_t = 0.25t$ and $d_t = 5a$[16]. We want to emphasis that, although the amplitude (Δ) and radius (d) of the Gaussian profile in the LRDH and LRDP are free parameters that can be turned in the tight-binding model, the numerical results show little quantitative difference as long as these parameters are of the same order as the chosen values. In general, an increase (decrease) of the amplitude or radius is equivalent to an increase (decrease) of the disorder concentration.

The hydrogen-like RS is described by the Hamiltonian [88, 93, 94]

$$H_{RS} = V \sum_i \left(d_i^\dagger c_i + \text{h.c}\right), \tag{5.5}$$

where V is the hopping between carbon and adatom. We consider the limiting case with $V \to \infty$, i.e., the electron at the impurity site is completely localized such that the resonant scatterer behaves like vacancy [88]. In our calculations, we use $t \approx 2.7$ eV and $t' = t/10$ for the nearest and next-nearest neighbor hopping parameters, respectively. The spin degree of freedom contributes only through a degeneracy factor and, for simplicity, has been omitted in Eq. (5.1).

The calculations of the electronic and optical properties are performed by the tight-binding propagation method (TBPM) [22, 88, 94, 95], which is based on the numerical solution of the time-dependent Schrödinger equation and Kubo's formula. The advantage of this method is that all the calculated quantities are extracted from the real-space wave propagation without any knowledge of the energy eigenstates. Furthermore one can introduce different kinds of (random) disorder by constructing the corresponding TB model for a sample scaling up to micrometers. For more details about the numerical methods we refer to Refs [16, 94]. The simulated graphene sample contains up to 8192×8192 atoms subject to periodic boundary conditions.

5.3 Transport Properties

We first consider the carrier-density-dependence of the microscopic conductivity $\sigma\,(n_e)$ for disordered graphene. The microscopic (or semi-classic) conductivity is calculated from the diffusive region of the charge transport, i.e., when the time-dependent dif-

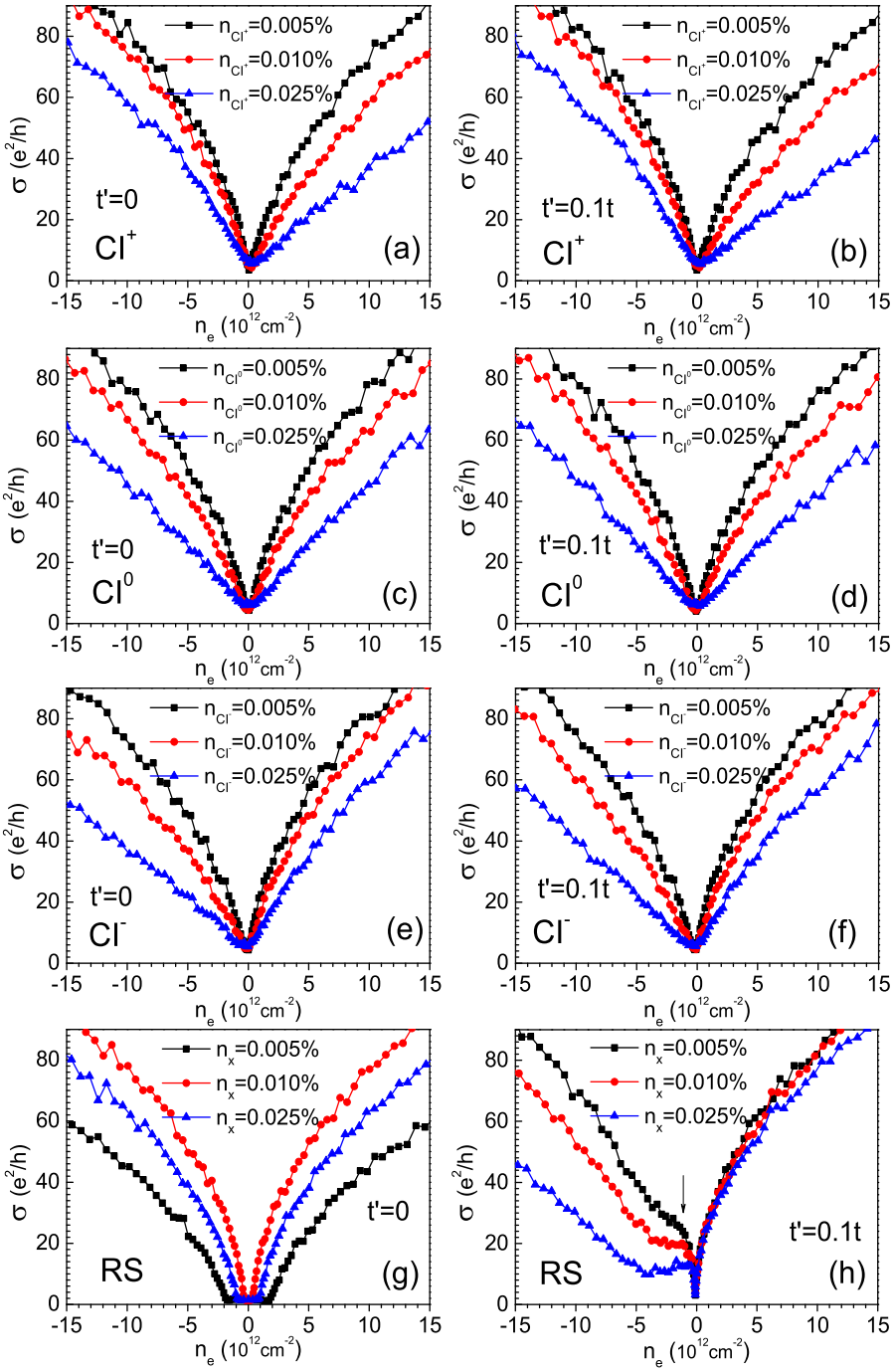
n_Cl+=0.005%
n_Cl+=0.010%
n_Cl+=0.025%
t'=0
Cl+
(a)
t'=0.1t
Cl+
(b)
n_Cl0=0.005%
n_Cl0=0.010%
n_Cl0=0.025%
t'=0
Cl0
(c)
t'=0.1t
Cl0
(d)
n_Cl-=0.005%
n_Cl-=0.010%
n_Cl-=0.025%
t'=0
Cl-
(e)
t'=0.1t
Cl-
(f)
n_x=0.005%
n_x=0.010%
n_x=0.025%
t'=0
RS
(g)
t'=0.1t
RS
(h)
σ (e²/h)
n_e (10¹²cm⁻²)

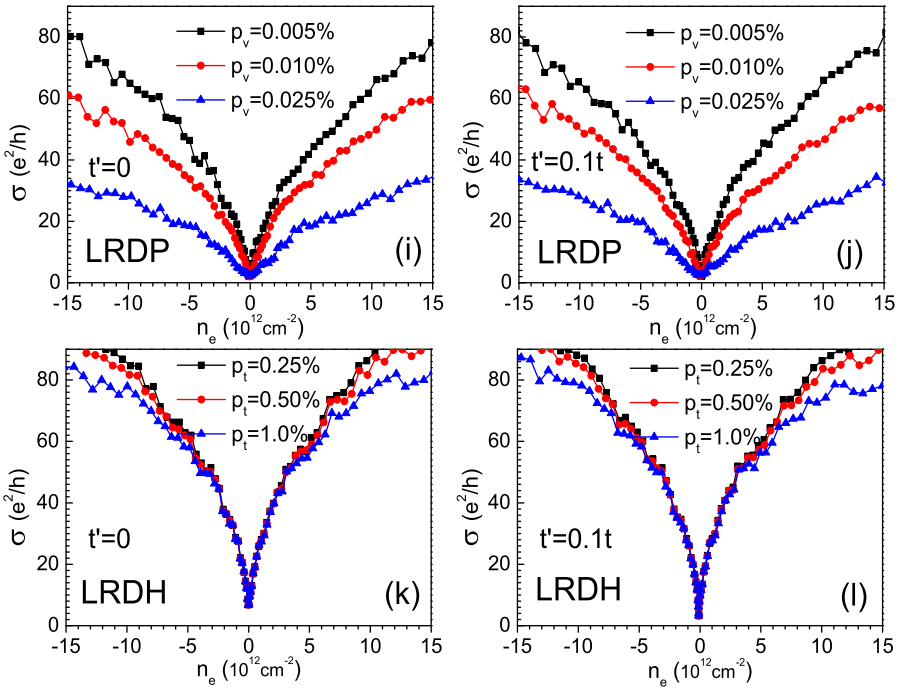

Figure 5.1: (Color online) The dc conductivity as a function of carrier density n_e for disordered graphene. Left panels show the results without the NNN hopping t', and right panels with $t' = 0.1t$. For CI, we use $\kappa = 6$ of hexagonal-boron nitride as a typical value of dielectric constant for graphene on a substrate. The use of other κ for different substrate such as SiO_2 does not change the results quantitatively. Here 0.01% disorder corresponds to a concentration of $3.82 \times 10^{11} cm^{-2}$.

fusion coefficient reaches its the maximum [96–98], and it is comparable to the conductivity extracted from the field-effect measurements. In TBPM, the microscopic conductivity at an energy E is calculated by using the Kubo formula [94, 95]

$$\sigma(E) = \max_{\tau} \frac{\rho(E)}{\Omega} \int_0^{\tau} dt \ \mathrm{Re}\left[e^{-iEt} \langle\varphi| J e^{i\mathcal{H}t} J |E\rangle\right], \tag{5.6}$$

where $|\varphi\rangle$ is a normalized random state, $|E\rangle$ is the *normalized* quasi-eigenstate[94], J is the current operator, Ω is the sample area, and $\rho(E)$ is the density of states (DOS) calculated via[22, 94]

$$\rho(E) = \frac{1}{2\pi} \int_{-\infty}^{\infty} e^{iEt} \langle\varphi|\varphi(t)\rangle \, dt. \tag{5.7}$$

The measured field-effect carrier mobility is related to the microscopic conductivity as $\mu(E) = \sigma(E)/en_e(E)$, where the carrier density n_e is obtained from the integral of DOS via $n_e(E) = \int_0^E \rho(\varepsilon)\, d\varepsilon$.

From the results shown in Fig. 5.1, we see that (1) including t' has negligible effects for CI, LRDP and LRDH, but the results for RS change dramatically. In the presence of RS, there is a strong electron-hole asymmetry in the carrier-density-dependence of dc conductivity. This is due to the fact that the impurity band created by RS is shifted from the Dirac point to the hole side[99], introducing strong electron-hole asymmetry at low energies; (2) as a consequence of this shift the conductivity plateau around the neutrality point is also shifted to the hole side, with an impurity-concentration dependent height and width (for very small concentration of RS, there is just as a kink instead of a plateau, see the point indicated by an arrow in Fig. 5.1(h)) ; These features can be observed in graphene if the concentration of generic RS is increased by exposing the material to atomic hydrogen [87]. (3) $\sigma(n_e)$ exhibits a sublinear dependence for small concentration for all types of disorders, except for the hole side in the presence of RS; (4) For LRDH, $\sigma(n_e)$ is insensitive to the changes of the disorder concentration (p_t); (5) No matter whether t' is nonzero or not, linear-dependent $\sigma(n_e)$ appears only in CI with large concentration of n_C [100], indicating that CI is the dominant source of disorder in the experimental samples which show clearly the linear carrier-density-dependent conductivity (such as K151 in Ref. [101], and Potassium doped samples in Ref. [102], etc.), agree with the theoretical prediction that $\sigma(n_e) \propto n_e$; (6) The electron-hole asymmetry appears also for larger concentration of CI if there is only one types of charge resource (CI^+ and CI^-). However, this asymmetry is different from the one due to RS in two aspects: first, for CI there is no kink or plateau in the profile; second, the conductivities on both electron and hole sides decrease significantly with larger concentration of CI; (7) Only in the case of CI^+ the conductivity on the electron side is smaller than on the hole side with the same concentration of carrier density, which is a unique signature of CI^+. This is in concert with experiment results [5, 101].

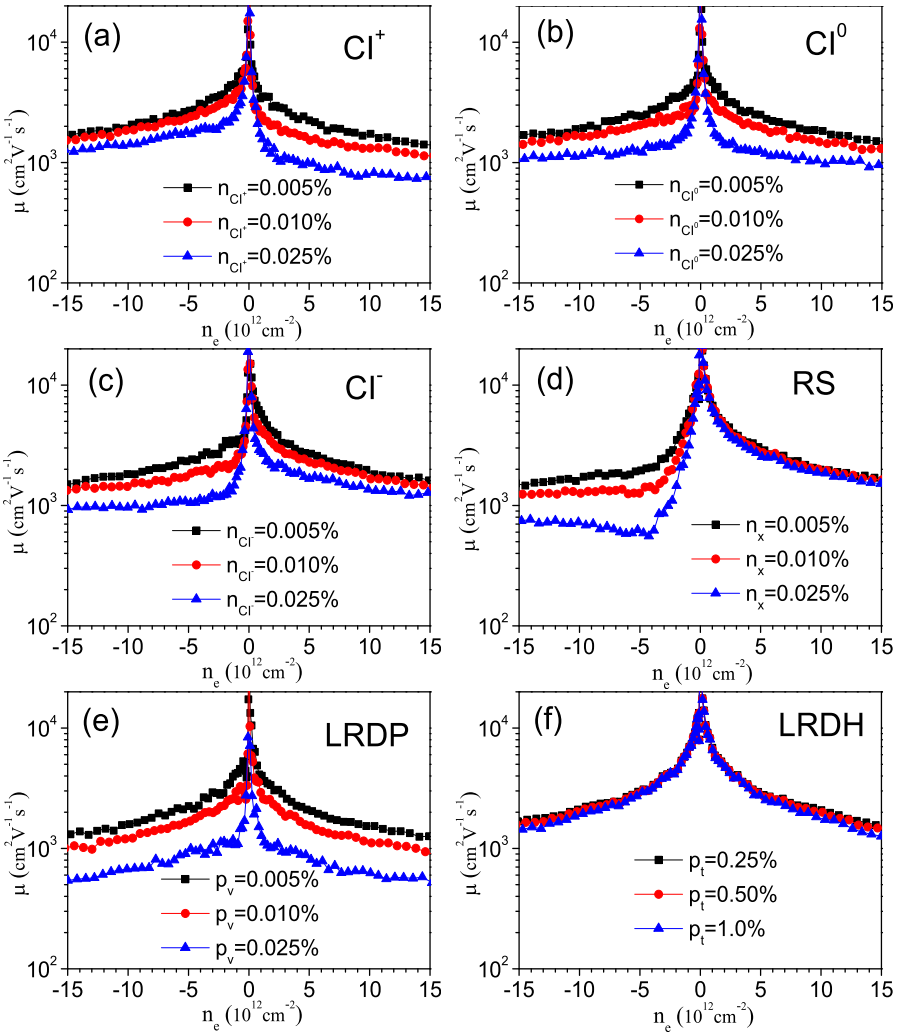

Figure 5.2: (Color online) The carrier mobility as a function of carrier density n_e for disorder graphene with t'.

The field-effect carrier mobility μ can be calculated from the conductivity and carrier-density through $\mu = \sigma/en_e$. In the following we show only the results with non-zero t'. From the results presented in Fig. 5.2, we see that (1) the carrier-dependence of mobility $\mu(n_e)$ is very similar for CI^0 and LRDP; (2) for LRDH, $\mu(n_e)$ is insensitive to the disorder strength; (3) electron-hole asymmetry appears for CI^+, CI^- and RS, but only in the case of CI^+ the electron mobility is smaller than the hole for the same concentration of carrier density; (4) for RS, the mobility on the electron side is insensitive to the impurity concentration, and its value can be one order of magnitude larger than the value on the hole side. For example, considering a RS concentration of $n_x = 0.025\%$, the electron mobility at carrier density $5 \times 10^{12} cm^{-2}$ is about $3,000$ $(cm^2V^{-1}s^{-1})$ but the hole mobility for the same carrier density is only ~ 300. This significant one order difference of the electron and hole mobility is a unique signature of RS; (5) with RS present, on the hole side, the carrier-density-dependent mobility is not monotonic and $\mu(n_e)$ reaches a minimum at the density corresponding to the tail of the conductivity plateau. However with RS present and $t' = 0$, the drop of mobility at the minimum is one order of magnitude larger than the experimental result.

The minimum conductivity $\sigma_{\min}$ at the Dirac point is of the order of $4e^2/h$ for all types of long-range disorders with $t' = t/10$. The values of $\sigma_{\min}$ in CI and LRDP do not depend on t', but change with the disorder strength such that larger concentration of disorder leads to larger values of $\sigma_{\min}$. This is due to the fact that the increase of potential sources in CI and LRDP will increase the DOS at the μ_F, leading to more states which can contribute to the transport. This may also explain the experimental observations in Ref. [101] and Ref. [103] in which the low mobility does not necessary correspond to a smaller value of $\sigma_{\min}$. For LRDH, the value of $\sigma_{\min}$ for $t' = 0$ is about two time larger than the value for $t' = t/10$, but both are insensitive to the disorder strength. For RS and $t' = 0$, $\sigma_{\min}$ is of the order of $4e^2/\pi h$, independent on the impurity concentration n_x [96–98], but if $t' = t/10$, $\sigma_{\min}$ from being of the order of $4e^2/h$ at small n_x to $4e^2/\pi h$ when $n_x \geq 0.1\%$, consistent with the numerical results of Ref. [98] (data not shown). Thus we conclude that our results indicate that the minimum conductivity $4e^2/h$ found in the experiments is dominated by long-range disorder but that the value of $4e^2/\pi h$ is due to RS only. It is worth to mention that our consideration does not take into account the effects of weak (anti) localization which can change the behavior of conductance at very large distances [104], due to energy smearing in our calculations. The latter works as dephasing. At the same time, this dephasing can be physical for real samples.

5.4 Optical Spectroscopy

The optical conductivity is calculated by using the Kubo formula [75] within TBPM[94] as (omitting the Drude contribution at $\omega = 0$)

$$\begin{aligned}\sigma(\omega) &= \lim_{\epsilon\to 0^+} \frac{e^{-\beta\omega}-1}{\omega\Omega}\int_0^\infty e^{-\epsilon t}\sin\omega t \\ &\quad \times 2\ \mathrm{Im}\,\langle\varphi|f(\mathcal{H})\,J(t)\,[1-f(\mathcal{H})]\,J|\varphi\rangle\,dt,\end{aligned} \tag{5.8}$$

where $\beta = 1/k_BT$ is the inverse temperature, $f(\mathcal{H}) = 1/\left[e^{\beta(\mathcal{H}-\mu_F)}+1\right]$ is the Fermi-Dirac distribution operator. Similar as for the transport properties, our numerical calculations show that t' has negligible effects on the optical properties of disordered graphene, except if RS are present. In general, disorder introduces new states which could contribute to the extra intraband excitations [4, 6–16], and therefore enhances the optical conductivity below $2\mu_F$, which might explain the observed background contribution in the optical spectrum for $0 < \omega < 2\mu_F$ [4, 5]. This is confirmed by the optical conductivity of disordered graphene calculations shown in Fig. 5.3. For disordered graphene with CI (including CI^0, CI^+ and CI^-) there is a strong enhancement of the optical conductivity below $2\mu_F$ and the enhanced spectrum forms a plateau with disorder-dependent minimum conductivity. For LRDP, there is in addition a disorder-dependent plateau in the optical spectrum below $2\mu_F$, which is much wider that the one due to CI. For LRDH, the enhancement of the optical conductivity is much smaller than for other types of disorders. For RS and $t' = 0$, a disorder-dependent peak appears at $\omega \approx \mu_F$, which is due to the enhanced excitations of the midgap states at the Dirac point. This peak disappears for $t' = t/10$, and instead, a disorder-dependent narrow plateau appears.

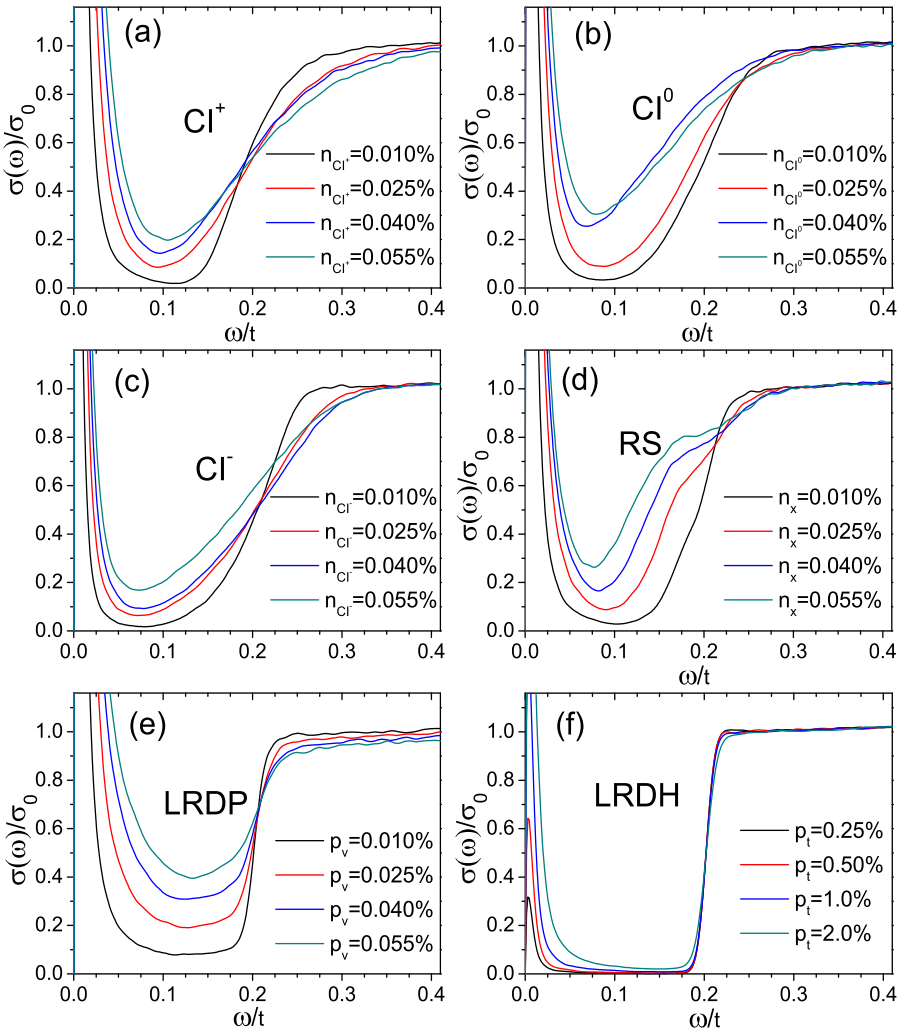

Figure 5.3: (Color online) The optical conductivity as a function of energy for disordered graphene with $\mu_F = 0.1t$ and $t' = 0.1t$. Here $\sigma_0 = \pi e^2/(2h)$ is the universal optical conductivity of graphene. All along the work the temperature of optical calculation is $T = 45K$, the same as in the experiment of Ref.[4].

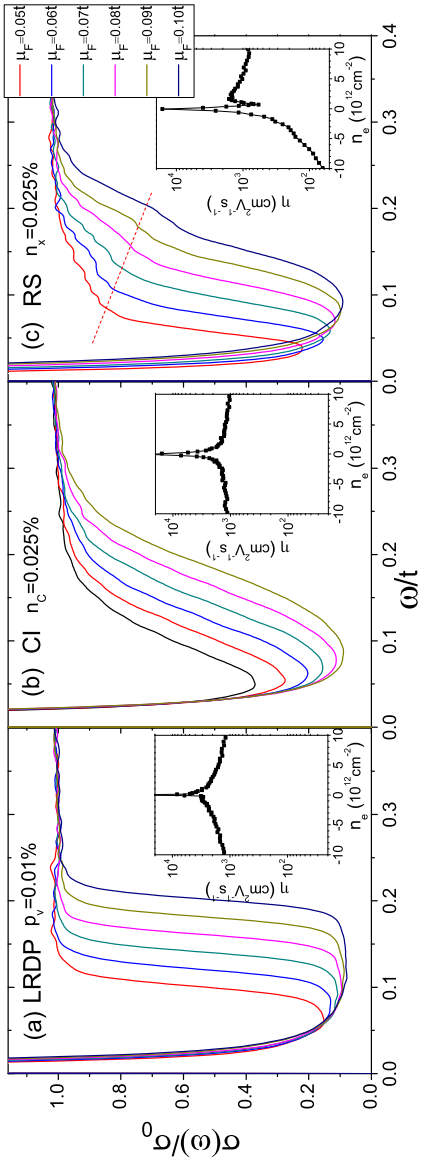

Figure 5.4: (Color online) The optical conductivity as a function of energy for disordered graphene (a) LRDP, (b) CI, and (c) RS with t'. The disorder concentrations are determined via the best fit to the experimental results of optical spectroscopy [4, 5]. The chemical potential μ_F changes from $0.05t$ to $0.1t$. The inner panels show the corresponding carrier mobility for the same concentration of disorder. The dashed line in (c) is a guide to eye separating two region in which the spectrum changes differently in the presence of RS.

In practice, instead of varying the disorder concentration, it is easier to change the chemical potential by applying an electrical potential to a gate. In order to compare to the experimental data of the spectroscopy measurements [4, 5] quantitatively, we plot in Fig. 5.4 the best fit of the optical conductivity for different chemical potentials ranging from $0.05t$ to $0.1t$ (since the results of CI^0, CI^+ and CI^- are similar, we present here only the case of CI^0). The disorder concentrations shown in Fig. 5.4 are determined by matching the minimum value of the optical conductivity plateau to the one observed [4, 5], yielding $\sigma_{plateau}$ of the order of $0.1\sigma_0$ for $\mu_F \approx t/10$. The best match of the disorder concentrations from our simulations is $p_v = 0.01\%$ for LRDP, $n_C = 0.025\%$ for CI and $n_x = 0.025\%$ for RS. A direct comparison of the profile of the spectrum between our simulations and the experiments in Ref. [4, 5] indicates that LRDP fits best to the experiments. In Ref. [4], the carrier mobility measured for the same device is as high as $8,700 cm^2 V^{-1} s^{-1}$ at carrier densities of $2 \times 10^{12} cm^{-2}$, and the LRDP also gives the highest mobility that it can reach $\sim 3,000$. For CI, $\mu \sim 1500$, and for RS the mobility is even smaller: for electrons it is $\sim 1,000$ and for holes ~ 300. Therefore we conclude that the background contribution of the optical conductivity below $2\mu_F$ as observed in Ref. [4] should be due mainly to the presence of LRDP.

5.5 Landau Level Spectrum

Finally we consider the electronic properties of graphene under a perpendicular magnetic field ($B = 50$T). The Landau quantization of the energy levels leads to separated peaks, as shown in Fig. 5.5. In the presence of disorder, the peak amplitudes of the Landau levels (LL) are reduced and the peaks become broader, except for LRDH in which the influence of disorder is much weaker than for other types of disorders. The peak profiles depend on the different sources of disorder. In general, for long range disorder, the peak is still symmetric along its center, but for RS, the changes are mainly restricted on the side with higher energy. Furthermore, the LL spectrum exhibits electron-hole symmetry for CI^0 and LRDP, but becomes asymmetric for CI^+, CI^- and RS. Especially, there are two small peaks around the first Landau level on the hole side shown in Fig. 5.5(d), which has the same origin as for the zero LL peaks, induced by RS [94]. The differences that appear in the LL spectrum also appear in quantum capacitance measurement, as the inverse of the latter is proportional to DOS [107–110]. Therefore, we also expect a huge effect of RS on the asymmetric quantum Hall conductivity, a topic for future research.

The quantum capacitance C_q, which is defined as $C_q = \rho e^2$, can be extracted experimentally from the total capacitance C and the geometry capacitance C_g via $1/C_q = 1/C - 1/C_g$. In Fig. 5.6 we show the carrier dependence of $1/\rho$, which is proportional to $1/C_q$, for different types of disorders under the same magnetic field

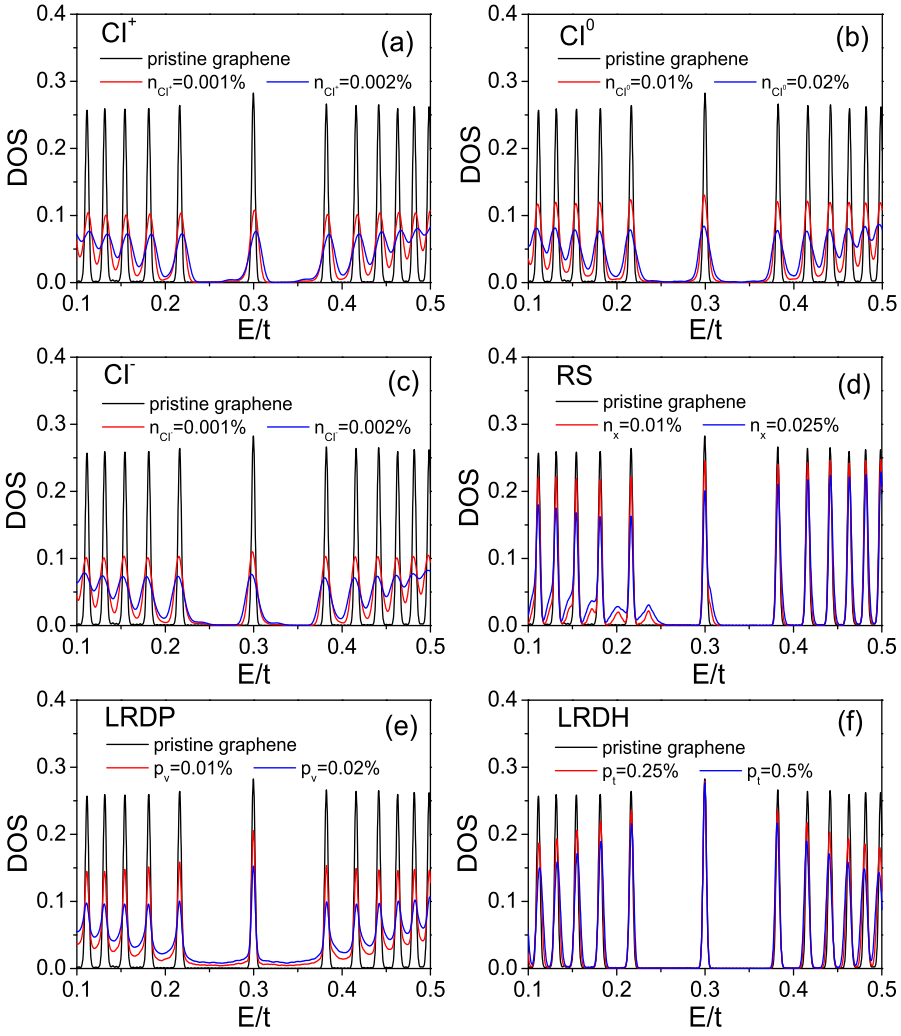

Figure 5.5: (Color online) Density of states as a function of energy for disordered graphene in the presence of a uniform perpendicular magnetic field ($B = 50$T).

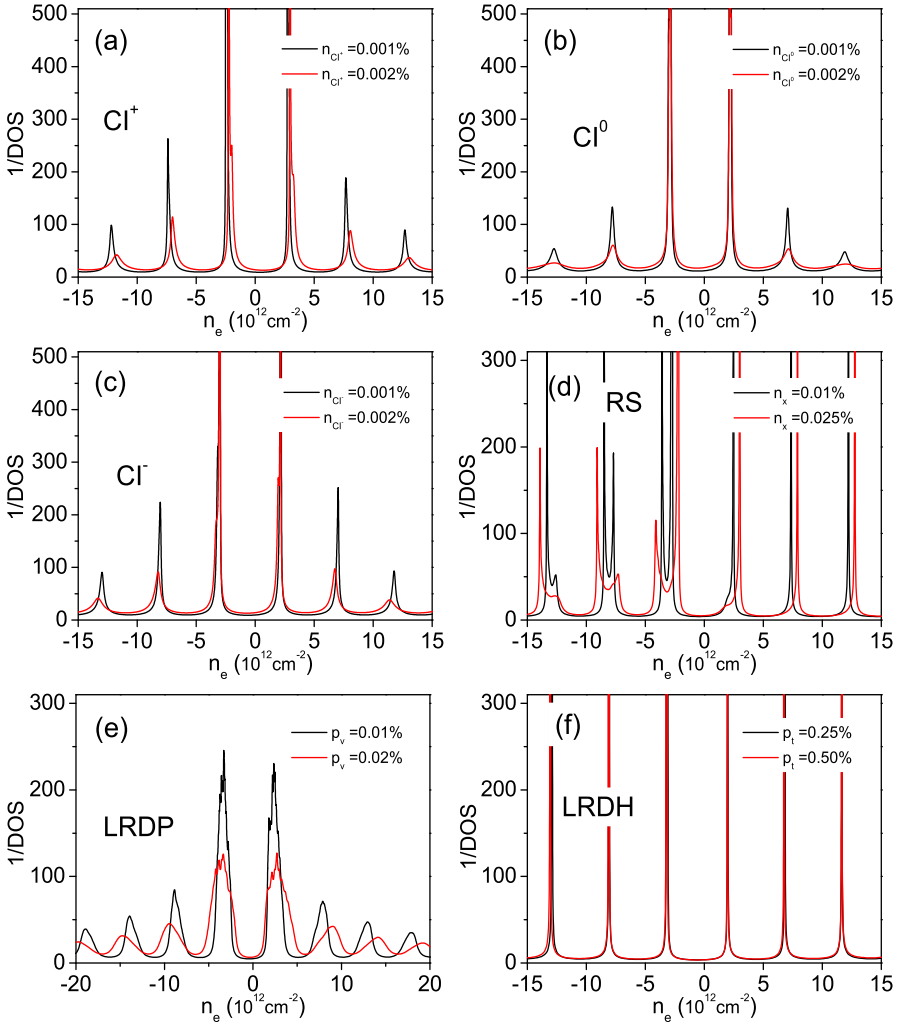

Figure 5.6: (Color online) The reciprocal of DOS as a function of carry density n_e for disordered graphene in the presence of a uniform perpendicular magnetic field ($B = 50$T).

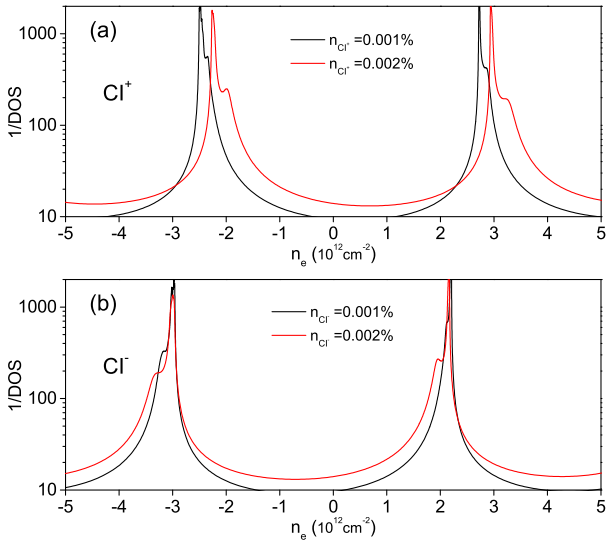

Figure 5.7: (Color online) The reciprocal of DOS as a function of carry density n_e for disordered graphene in the presence of a uniform perpendicular magnetic field ($B = 50$T).

($B = 50$T). Due to the presence of disorder, the peak amplitudes decrease significantly except for the LRDH, in which the influence of random hopping is negligible. The change of the spectrum profile for each type of disorder has similar feature deduced from the corresponding DOS. Furthermore, some characters become even more clear in the spectrum of $1/\rho$. For example, the electron-hole asymmetry appeared in the presence of single-type charge impurities (CI^+ or CI^-) is very special: the slopes of the peaks on the hole and electron sides point to the same direction, depending on the sign of CI (see a zoom of the first two peaks in Fig. 5.7). This unique feature has also been observed in the experiments[1]

5.6 Conclusion

We have studied the effects of different types of disorders on the electronic, transport and optical properties of graphene. By comparing the results with and without the NNN hopping, we find that the NNN hopping has negligible effect in combination with long-range disorder such as CI, LRDP and LRDH, but that it changes the physical properties dramatically if RS are present. In the latter case, we find that (1) there is

[1]private communication with Konstantin Novoselov.

Table 5.1: List of the dominant disorder source in different experimental samples, identified by using the fingerprints appeared in the transport or optical properties. The figures indicated in the table are these in the corresponding reference.

Ref.	Disorder	Fingerprints
[85]	LRDP	Symmetrical $\sigma(n_e)$ in Fig.2 (a), the minimum conductivity plateau in Fig. 2 (b), and the relation of mobility μ versus n^* in Fig. 2 (c).
[87]	RS	Asymmetrical $\sigma(n_e)$ of the blue and red curves in Fig. 2 (a).
[4]	LRDP	A plateau in the doped optical spectroscopy in Fig. 2 (b), together with the corresponding relatively high mobility.
[5]	CI^+	A narrow plateau in the doped optical spectroscopy, together with a shift of the minimum conductivity to the electron side in Fig. 1.
[101]	CI^+	The electron mobility is smaller than the hole one in Fig. 2 for samples K130, K145, K151; The minimum conductivity shifts to the electron side in Fig. 3.
[102]	CI^-	The hole conductivity is smaller than electron one and the minimum conductivity shifts to the hole side in Fig. 2.
[105]	CI^+	The hole conductivity is larger than electron one in Fig. 1 (the sample before annealing).
[106]	CI	A narrow plateau in the doped optical spectroscopy in Fig. 3 (b).

an extra conductivity plateau on the hole side, with a value larger than the minimum conductivity at the neutrality point; (2) the carrier-density-dependent mobility does not always drop with larger carrier density but instead, it reaches a minimum at the edge of the conductivity plateau. (3) a strong electron-hole asymmetry appears in the carrier-density-dependent transport properties and Landau level spectrum; (4) the minimum conductivity at the shifted Dirac point is no longer a constant, but drops to $4e^2/\pi h$ when the impurity concentration is larger than 0.05%. For long-range disorder, the minimum conductivity for $t' = t/10$ is of the order of $4e^2/h$ and increases with larger disorder concentration for CI and LRDP, but remains the same for LRDP. The mobility always becomes smaller with larger concentration of disorder, however, the minimum conductivity does not follow the same rule, consistent with

the transport measurement [101, 103]. For doped graphene, the presence of disorder introduces extra excitations below $2\mu_F$ but the profiles of the optical spectra are different for different types of disorders.

As an example of using the fingerprints discussed in the main text, we collect the dominant source of disorder in several well-known experiments and list them in Table I. Different types of disorders such as CI (including CI^0, CI^+ and CI^-), LRDP and RS have been identified in different experiments, except for the LRDH which has been proved to have negligible influence to the electronic properties. The results obtained in Table 5.1 also suggest the dominant source of disorder may vary from sample to sample.

In summary, we suggest that the different but characteristic features that appear in the calculated electronic, transport and optical properties can be used as fingerprints to identify the dominant sources of disorder in graphene.

Chapter 6

Dynamics of open quantum spin systems: An assessment of the quantum master equation

Data of the numerical solution of the time-dependent Schrödinger equation of a system containing one spin-1/2 particle interacting with a bath of up to 32 spin-1/2 particles is used to construct a Markovian quantum master equation describing the dynamics of the system spin. The procedure of obtaining this quantum master equation, which takes the form of a Bloch equation with time-independent coefficients, accounts for all non-Markovian effects in as much the general structure of the quantum master equation allows. Our simulation results show that, with a few rather exotic exceptions, the Bloch-type equation with time-independent coefficients provides a simple and accurate description of the dynamics of a spin-1/2 particle in contact with a thermal bath. A calculation of the coefficients that appear in the Redfield master equation in the Markovian limit shows that this perturbatively derived equation quantitatively differs from the numerically estimated Markovian master equation, the results of which agree very well with the solution of the time-dependent Schrödinger equation.

This chapter was previously published as
P. Zhao, H. De Raedt, S. Miyashita, F. Jin, and K. Michielsen, Physical Review E **94**, 022126 (2016).

6.1 Introduction

In general, a physical system can seldom be considered as completely isolated from its environment. Such closed systems can and should, of course, be studied in great detail. However, as they lack the ability to interact with the environment in which they are embedded or with the apparatus that is used to perform measurements on it, such studies do not include the effects of the, usually uncontrollable, environment which may affect the dynamics of the system in a non-trivial manner. The alternative is to consider the system of interest as an open system that is a system interacting with its environment.

The central idea of theoretical treatments of open quantum systems is to derive approximate equations of motion of the system by elimination of the environmental degrees of freedom [18, 111–113]. In 1928, Pauli derived a master equation for the occupation probabilities of a quantum subsystem interacting with the environment [114]. Since then, various methods have been developed to derive quantum master equations starting from the Liouville-von Neumann equation for the density matrix of the whole system [18, 111–113, 115]. In order to obtain an equation of motion for the system which is tractable and readily amenable to detailed analysis, it is customary to make the so-called Markov approximation, which in essence assumes that the correlations of the bath degrees of freedom vanish on a short time span.

Without reference to any particular model system, in 1970, Lindblad derived a quantum master equation which is Markovian and which preserves positivity (a non-negative definite density matrix) during the time evolution [113, 116]. The applicability of the Lindblad master equation is restricted to baths for which the time correlation functions of the operators that couple the system to the bath are essentially δ-functions [117], an assumption that may be well justified in quantum optics [115].

Using second-order perturbation theory, Redfield derived a master equation which does not require the bath correlations to be approximately δ-functions in time [18]. The Redfield master equation has found many applications to problems where the dynamics of the bath is faster than that of the system, for instance to the case of nuclear magnetic resonance in which the system consists of one spin coupled to other spins and/or to phonons. This approach and variations of it have been successfully applied to study the natural linewidth of a two-level system [19, 118, 119], systems of interacting spins [120] and nonlinear spin relaxation [121].

The Redfield master equation can be systematically derived from the principles of quantum theory but only holds for weak coupling. However, the Redfield master equation may lead to density matrices that are not always positive, in particular when the initial conditions are such that they correspond to density matrices that close to the boundary of physically admissible density matrices [122, 123].

Obviously, the effect of the finite correlation time of the thermal bath becomes important when the time scale of the system is comparable to that of the thermal bath. Then the Markovian approximation may no longer be adequate and in deriving the quantum master equation, it becomes necessary to consider the non-Markovian aspects and to treat the initial condition correctly [113, 124–132].

By introducing the concept of slippage in the initial conditions, it was shown that the Markovian equations of motion obtained in the weak coupling regime are a consistent approximation to the actual reduced dynamics and that slippage captures the effects of the non-Markovian evolution that takes place in a short transient time, of the order of the relaxation time of the isolated bath [122]. Provided that nonlocal memory effects that take place on a very short time scale are included, the Markovian approximation that preserves the symmetry of the Hamiltonian yields an accurate description of the system dynamics [122]. Following up on this idea, a general form of a slippage operator to be applied to the initial conditions of the Redfield master equation was derived [117]. The slippage was expressed in terms of an operator describing the non-Markovian dynamics of the system during the time in which the bath relaxes on its own, relatively short, time scale. It was shown that the application of the slippage superoperator to the initial density matrix of the system yields a Redfield master equation that preserves positivity [117]. Apparently, the difference between the non-Markovian dynamics and its Markovian approximation can be reduced significantly by first applying the slippage operator and then letting the system evolve according to the Redfield master equation [117].

The work discussed and cited earlier almost exclusively focuses on models of the environment that are described by a collection of harmonic oscillators. In contrast, the focus of this chapter is on the description of the time evolution of a quantum system with one spin-1/2 degree of freedom coupled to a larger system of similar degrees of freedom, acting as a thermal bath. Our reasons for focusing on spin-1/2 models are twofold.

First, such system-bath models are relevant for the description of relaxation processes in nuclear magnetic and electron spin resonance [17–19] but have also applications to, e.g. the field of quantum information processing, as most of the models used in this field are formulated in terms of qubits (spin-1/2 objects) [20, 21].

Secondly, the aim of the present work is to present a quantitative assessment of the quantum master equation approach by comparing the results with those obtained by an approximation-free, numerical solution of the time-dependent Schrödinger equation of the system+bath. The work presented in this chapter differs from earlier numerical work on dissipative quantum dynamics [133–137] by accounting for the non-trivial many-body dynamics of the bath without resorting to approximations, at the expense of using much more computational resources. Indeed, with state-of-the-art computer hardware, e.g the IBM BlueGene/Q, and corresponding simulation software [138],

it has become routine to solve the time-dependent Schrödinger equation for systems containing up to 36 spin-1/2 objects. As we demonstrate in this chapter, this allows us to mimic a large thermal bath at a specific temperature and solve for the full dynamic evolution of a spin-1/2 object coupled to the thermal bath of spin-1/2 objects.

From the numerically exact solution of the Schrödinger dynamics we compute the time-evolution of the density matrix of the system and by least-square fitting, obtain the "optimal" quantum master equation that approximately describes the same time-evolution. For a system of one spin-1/2 object, this quantum master equation takes the form of a Bloch equation with time-independent coefficients. Clearly, this procedure of obtaining the quantum master equation is free of any approximation and accounts for all non-Markovian effects in as much the general structure of the quantum master equation allows. Our simulation results show that, with a few rather exotic exceptions, the Bloch-type equation with time-independent coefficients provides a very simple and accurate description of the dynamics of a spin-1/2 object in contact with a thermal bath.

This chapter is organized as follows. In section 6.2, we give the Hamiltonians that specify the system, bath and system-bath interaction. Section 6.3 briefly reviews the numerical techniques that we use to solve the time-dependent Schrödinger equation, to compute the density matrix, and to prepare the bath in the thermal state at a given temperature. We also present simulation results that demonstrate that the method of preparation yields the correct thermal averages. For completeness, Sec. 6.4 recapitulates the standard derivation of the quantum master equation, writes the formal solution of the latter in a form that is suited for our numerical work and shows that the Redfield equations have this form. We then use the simulation tool to compute the correlations of the bath-operators that determine the system-bath interaction and discuss their relaxation behavior. Section 6.5 explains the least-square procedure of extracting, from the solution of the time-dependent Schrödinger equation, the time-evolution matrix and the time-independent contribution that determine the "optimal" quantum master equation. This least-square procedure is validated by its application to data that originate from the Bloch equation, as explained in Appendix A. In Sec. 6.6, we specify the procedure by which we fit the quantum master equation to the data obtained by solving the time-dependent Schrödinger equation and present results of several tests. The results of applying the fitting procedure to baths containing up to 32 spins are presented in Sec. 6.7. Finally, in Sec. 6.8, we discuss some exceptional cases for which the quantum master equation is not expected to provide a good description. The chapter concludes with the summary, given in Sec. 6.9.

6.2 System coupled to a bath: Model

The Hamiltonian of the system (S) + bath (B) takes the generic form

$$H \quad = \quad H_{\rm S} + H_{\rm B} + \lambda H_{\rm SB}. \tag{6.1}$$

The overall strength of the system-bath interaction is controlled by the parameter λ. In this work, we limit ourselves to a system which consists of one spin-1/2 object described by the Hamiltonian

$$H_{\rm S} \quad = \quad -h^x \sigma_0^x, \tag{6.2}$$

where $\sigma_n = (\sigma_n^x, \sigma_n^y, \sigma_n^z) = (\sigma_n^1, \sigma_n^2, \sigma_n^3)$ denote the Pauli-spin matrices for spin-1/2 object n, and h^x is a time-independent external field. Throughout this chapter, we adopt units such that $\hbar = 1$ and $h^x = 1/2$ and express time in units of π/h^x. We will use the double notation with the (x, y, z) and $(1, 2, 3)$ superscripts because depending on the situation, it simplifies the writing considerably.

The Hamiltonian for the system-bath interaction is chosen to be

$$H_{\rm SB} = -\sum_{n=1}^{N_{\rm B}} (J_n^x \sigma_n^x \sigma_0^x + J_n^y \sigma_n^y \sigma_0^y + J_n^z \sigma_n^z \sigma_0^z) = \sum_{\alpha=x,y,z} \sigma_0^\alpha B_\alpha = \sum_{i=1}^{3} \sigma_0^i B_i, \tag{6.3}$$

where $N_{\rm B}$ is the number of spins in the bath, the J_n^α are real-valued random numbers in the range $[-J, +J]$ and

$$\begin{aligned} B_x \quad &= B_1 = -\textstyle\sum_{n=1}^{N_{\rm B}} J_n^x \sigma_n^x \\ B_y \quad &= B_2 = -\textstyle\sum_{n=1}^{N_{\rm B}} J_n^y \sigma_n^y \\ B_z \quad &= B_3 = -\textstyle\sum_{n=1}^{N_{\rm B}} J_n^z \sigma_n^z \end{aligned} \tag{6.4}$$

are the bath operators which, together with the parameter λ, define the system-bath interaction. As the system-bath interaction strength is controlled by λ, we may set $J = 1/4$ without loss of generality.

As a first choice for the bath Hamiltonian $H_{\rm B}$ we take

$$H_{\rm B} = -K \sum_{n=1}^{N_{\rm B}} \left(\sigma_n^x \sigma_{n+1}^x + \sigma_n^y \sigma_{n+1}^y + \Delta \sigma_n^z \sigma_{n+1}^z\right) - \sum_{n=1}^{N_{\rm B}} \left(h_n^x \sigma_n^x + h_n^z \sigma_n^z\right). \tag{6.5}$$

The fields h_n^x and h_n^z are real-valued random numbers in the range $[-h_{\rm B}^x, +h_{\rm B}^x]$ and $[-h_{\rm B}^z, +h_{\rm B}^z]$, respectively. In our simulation work, we use periodic boundary conditions $\sigma_n^\alpha = \sigma_{n+N_{\rm B}}^\alpha$ for $\alpha = x, y, z$. Note that we could have opted equally well to use open-end boundary conditions but for the sake of simplicity of presentation, we choose

the periodic boundary conditions. For $\Delta = 1$, the first term in Eq. (6.5) is the Hamiltonian of the one-dimensional (1D) Heisenberg model on a ring.

As a second choice, we consider the 1D ring with Hamiltonian

$$H_{\rm B} = -\sum_{n=1}^{N_{\rm B}} \left(K_n^x \sigma_n^x \sigma_{n+1}^x + K_n^y \sigma_n^y \sigma_{n+1}^y + K_n^z \sigma_n^z \sigma_{n+1}^z\right) - \sum_{n=1}^{N_{\rm B}} \left(h_n^x \sigma_n^x + h_n^z \sigma_n^z\right), \quad (6.6)$$

where the K_n^x's, K_n^y's, and K_n^z's are uniform random numbers in the range $[-K, K]$. Because of the random couplings, it is unlikely that it is integrable (in the Bethe-ansatz sense) or has any other special features such as conserved magnetization etc.

The bath Hamiltonians (6.5) and (6.6) both share the property that the distribution of nearest-neighbor energy levels is of Wigner-Dyson-type, suggesting that the correspondig classical baths exhibit chaos. Earlier work along the lines presented in this chapter has shown that spin baths with a Wigner-Dyson-type distribution are more effective as sources for fast decoherence than spin baths with Poisson-type distribution [139]. Fast decoherence is a prerequisite for a system to exhibit fast relaxation to the thermal equilibrium state [140, 141]. Extensive simulation work on spin-baths with very different degrees of connectivity [142–145] suggest that as long as there is randomness in the system-bath coupling and randomness in the intra-bath couplings, the simple models (6.5) and (6.6) may be considered as generic spin baths.

Finally, as a third choice, we consider

$$H_{\rm B} = -\sum_{\langle n,n'\rangle} \left(K_{n,n'}^x \sigma_n^x \sigma_{n'}^x + K_{n,n'}^y \sigma_n^y \sigma_{n'}^y + K_{n,n'}^z \sigma_n^z \sigma_{n'}^z\right) - \sum_{n=1}^{N_{\rm B}} \left(h_n^x \sigma_n^x + h_n^z \sigma_n^z\right), \quad (6.7)$$

where the $K_{n,n'}^x$'s, $K_{n,n'}^y$'s, and $K_{n,n'}^z$'s are uniform random numbers in the range $[-K, K]$, and $\sum_{\langle n,n'\rangle}$ denotes the sum over all pairs of nearest neighbors on a three-dimensional (3D) cubic lattice. Again, because the random couplings and the 3D connectivity, it is unlikely that it is integrable or has any other special features such as conserved magnetization etc. As the solution of the time-dependent Schrödinger equation (TDSE) for the 3D model Eqs. (6.7) takes about a factor of 2 more CPU time than in the case of a 1D model with the same number of bath spins, in most of our simulations we will use the 1D models and only use the 3D model to illustrate that the connectivity of the bath is not a relevant factor.

6.3 Quantum dynamics of the whole system

The time evolution of a closed quantum system defined by Hamiltonian (6.1) is governed by the TDSE

$$i\frac{\partial}{\partial t}|\Psi(t)\rangle \quad = \quad H|\Psi(t)\rangle. \quad (6.8)$$

The pure state $|\Psi(t)\rangle$ of the whole system S + B evolves in time according to

$$|\Psi(t)\rangle \quad = \quad e^{-itH}|\Psi(0)\rangle = \sum_{i=1}^{D_{\rm S}} \sum_{p=1}^{D_{\rm B}} c(i,p,t)|i,p\rangle, \tag{6.9}$$

where $D_{\rm S} = 2$ and $D_{\rm B} = 2^{N_{\rm B}}$ are the dimensions of the Hilbert space of the system and bath, respectively. The coefficients $\{c(i,p,t)\}$ are the complex-valued amplitudes of the corresponding elements of the set $\{|i,p\rangle\}$ which denotes the complete set of the orthonormal states in up–down basis of the system and bath spins.

The size of the quantum systems that can be simulated, that is the size for which Eq. (6.9) can actually be computed, is primarily limited by the memory required to store the pure state. Solving the TDSE requires storage of all the numbers $\{c(i,p,t)|i = 1,2\ ,p = 1,\ldots,2^{N_{\rm B}}\}$. Hence the amount of memory that is required is proportional to $2^{N_{\rm B}+1}$, that is it increases exponentially with the number of spins of the bath. As the number of arithmetic operations also increases exponentially, it is advisable to use 13 - 15 digit floating-point arithmetic (corresponding to $16 = 2^4$ bytes for each pair of real numbers). Therefore, representing a pure state of $N_{\rm B} + 1$ spin-1/2 objects on a digital computer requires at least $2^{N_{\rm B}+5}$ bytes. For example, for $N_{\rm B} = 23$ ($N_{\rm B} = 35$) we need at least 256 MB (1 TB) of memory to store a single state $|\Psi(t)\rangle$. In practice we need storage for three vectors, and memory for communication buffers, local variables and the code itself.

The CPU time required to advance the pure state by one time step τ is primarily determined by the number of operations to be performed on the state vector, that is it also increases exponentially with the number of spins. The elementary operations performed by the computational kernel can symbolically be written as $|\Psi\rangle \leftarrow U|\Psi\rangle$ where the U's are sparse unitary matrices with a relatively complicated structure. A characteristic feature of the problem at hand is that for most of the U's, all elements of the set $\{c(i,p,t)|i = 1,2\ ,p = 1,2^{N_{\rm B}}\}$ are involved in the operation. This translates into a complicated scheme for efficiently accessing memory, which in turn requires a sophisticated communication scheme [138].

We can exclude that the conclusions that we draw from the numerical results are affected by the algorithm used to solve the TDSE by performing the real-time propagation by e^{-itH} by means of the Chebyshev polynomial algorithm [32–35]. This algorithm is known to yield results that are very accurate (close to machine precision), independent of the time step used [36]. A disadvantage of this algorithm is that, especially when the number of spins exceeds 28, it consumes significantly more CPU and memory resources than a Suzuki-Trotter product-formula based algorithm [36]. Hence, once it has been verified that the numerical results of the latter are, for practical purposes, as good as the numerically exact results, we use the latter for the simulations of the large systems.

6.3.1 Density matrix

According to quantum theory, observables are represented by Hermitian matrices and the correspondence with measurable quantities is through their averages defined as [146]

$$\langle \mathcal{A} \rangle = \mathbf{Tr}\ \rho(t)\mathcal{A}, \tag{6.10}$$

where $\mathcal{A}$ denotes a Hermitian matrix representing the observable, $\rho(t)$ is the density matrix of the whole system $S+B$ at time t and $\mathbf{Tr}$ denotes the trace over all states of the whole system S+B. If the numerical solution of the TDSE for a pure state of $N_{\mathrm{B}}+1$ spins already requires resources that increase exponentially with the number of spins of the bath, computing Eq. (6.10) seems an even more daunting task. Fortunately, we can make use of the "random-state technology" to reduce the computational cost to that of solving the TDSE for one pure state [147]. The key is to note that if $|\Phi\rangle$ is a pure state, picked randomly from the $2^{N_{\mathrm{B}}+1}$-dimensional unit hypersphere, one can show in general that for Hermitian matrices $\mathcal{A}$ [147]

$$\mathbf{Tr}\ \mathcal{A} = D\langle\Phi|\mathcal{A}|\Phi\rangle \pm \mathcal{O}(D^{-1/2}), \tag{6.11}$$

where D is the number of diagonal elements of the matrix $\mathcal{A}$ (= the dimension of the Hilbert space) and $\pm\mathcal{O}(x)$ should be read as saying that the standard deviation is of order x. For the case at hand $D = 2^{N_{\mathrm{B}}+1}$, hence Eq. (6.11) indicates that for a large bath, the statistical errors resulting from approximating $\mathbf{Tr}\ \mathcal{A}$ by $\langle\Phi|\mathcal{A}|\Phi\rangle$ vanishes exponentially with the number of bath spins. For large baths, this property makes the problem amenable to numerical simulation. Therefore, from now on, we replace the "$\mathbf{Tr}$ " by a matrix element of a random pure state whenever the trace operation involves a number of states that increases exponentially with the number of spins (in the present case, bath spins only).

The state of the system S is completely described by the reduced density matrix

$$\rho_{\mathrm{S}}(t) \equiv \mathbf{Tr}_{\mathrm{B}}\rho(t), \tag{6.12}$$

where $\rho(t)$ is the density matrix of the whole system $S+B$ at time t, $\mathbf{Tr}_{\mathrm{B}}$ denotes the trace over the degrees of freedom of the bath, and $\mathbf{Tr}_{\mathrm{S}}\rho_{\mathrm{S}}(t) = \mathbf{Tr}\ \rho(t) = 1$. In practice, as the dimension of the Hilbert space of the bath may be assumed to be large, we can, using the "random-state technology", compute the trace over the bath degrees of freedom as

$$(\mathbf{Tr}_{\mathrm{B}}\mathcal{A})_{i,j} \approx \sum_{p=1}^{D_{\mathrm{B}}} c^*(i,p,t)c(j,p,t)\ \langle i,p|\mathcal{A}|j,p\rangle. \tag{6.13}$$

In the case that the system contains only one spin, which is the case that we consider in the present work, the reduced density matrix can, without loss of generality,

be written as

$$\rho_{\rm S}(t) \;=\; \frac{1}{2}\sum_{\alpha=x,y,z}\left[1+\rho_\alpha(t)\sigma_0^\alpha\right] = \frac{1}{2}\sum_{k=1}^{3}\left[1+\rho_k(t)\sigma_0^k\right], \tag{6.14}$$

where $\rho_x(t)=\rho_1(t)$, $\rho_y(t)=\rho_2(t)$ and $\rho_z(t)=\rho_3(t)$ are real numbers. Making use of the "random-state technology", it follows immediately from Eq. (6.14) that

$$\begin{aligned}
\rho_1(t) &= \rho_x(t) = \mathbf{Tr}_{\rm S}\rho_{\rm S}(t)\sigma_0^x = \mathbf{Tr}\;\rho(t)\sigma_0^x \approx \langle\Psi(t)|\sigma_0^x|\Psi(t)\rangle\\
\rho_2(t) &= \rho_y(t) = \mathbf{Tr}_{\rm S}\rho_{\rm S}(t)\sigma_0^y = \mathbf{Tr}\;\rho(t)\sigma_0^y \approx \langle\Psi(t)|\sigma_0^y|\Psi(t)\rangle\\
\rho_3(t) &= \rho_z(t) = \mathbf{Tr}_{\rm S}\rho_{\rm S}(t)\sigma_0^z = \mathbf{Tr}\;\rho(t)\sigma_0^z \approx \langle\Psi(t)|\sigma_0^z|\Psi(t)\rangle.
\end{aligned} \tag{6.15}$$

Therefore, to obtain (accurate approximations to) the expectation values of the system operators we compute the expressions that appear in the left-hand side of Eq. (6.15) using the numerical solution of the TDSE in the form given by Eq. (6.9).

6.3.2 Thermal equilibrium state

As a first check on the numerical method, it is of interest to simulate the case in which the system+bath are initially in thermal equilibrium and study the effects of the bath size $N_{\rm B}$ and system-bath interaction strength λ on the expectation values of the system spin.

The procedure is as follows. First we generate a random state of the whole system, meaning that

$$|\Phi(\beta)\rangle \;=\; \frac{e^{-\beta H/2}|\Phi\rangle}{\langle\Phi|e^{-\beta H}|\Phi\rangle^{1/2}}, \tag{6.16}$$

where β denotes the inverse temperature. As one can show that for any observable $\mathcal{A}(t)$ [147]

$$\langle\mathcal{A}(t)\rangle = \frac{\mathbf{Tr}\;e^{-\beta H}\mathcal{A}(t)}{\mathbf{Tr}\;e^{-\beta H}} = \langle\Phi(\beta)|\mathcal{A}(t)|\Phi(\beta)\rangle \pm \mathcal{O}(D^{-1/2}), \tag{6.17}$$

we can use $\langle\Phi(\beta)|\mathcal{A}|\Phi(\beta)\rangle$ to estimate $\langle\mathcal{A}(t)\rangle$. As $e^{-\beta H}$ commutes with e^{-itH}, $\langle\mathcal{A}(t)\rangle = \langle\mathcal{A}(t=0)\rangle$ is time independent. Excluding the trivial case that $[H,\mathcal{A}(t)]=0$, $\langle\Phi(\beta)|\mathcal{A}(t)|\Phi(\beta)\rangle = \langle\Phi(\beta)|e^{+itH}\mathcal{A}e^{-itH}|\Phi(\beta)\rangle$ depends on time: indeed, in general the random state $|\Phi(\beta)\rangle$ is unlikely to be an eigenstate of H. Therefore, the simulation data obtained by solving the TDSE with $|\Phi(\beta)\rangle$ as the initial state should display some time dependence. However, from Eq. (6.17), it follows directly that the time dependent contributions will vanish very fast, namely as $D^{-1/2}$. Hence this time dependence, an artifact of using "random state technology", reveals itself as statistical fluctuations and can be ignored.

For the system in thermal equilibrium at the inverse temperature β we have

$$\langle \sigma_0^x \rangle = \tanh(\beta h^x) \quad , \quad \langle \sigma_0^y \rangle = 0 \quad , \quad \langle \sigma_0^z \rangle = 0. \tag{6.18}$$

In Fig. 6.1 we show simulation results for a bath at $\beta = 2$ for $N_{\rm B} = 13$ (left) and $N_{\rm B} = 28$ spins (right). If the system-bath interaction is sufficiently weak then, from Eq. (6.18), we expect that $\langle \sigma_0^x \rangle \approx \tanh \beta h^x$ which for $\beta h^x = 1$ yields $\langle \sigma_0^x \rangle \approx 0.762$. From the TDSE solution with $N_{\rm B} = 13$, it is clear that the spin averages fluctuate (due to the use of the random thermal state which is not an eigenstate of H). As expected, for $N_{\rm B} = 28$ the fluctuations are much smaller, in concert with Eq. (6.17).

Computing the time averages for a bath with $N_{\rm B} = 13$ and for the time interval $[0, T]$ with $T = 1000$ yields

$$\begin{aligned}
\frac{1}{T}\int_0^T dt\, \langle \Phi(\beta)|\sigma_0^x(t)|\Phi(\beta)\rangle &= 0.81(0.14) \\
\frac{1}{T}\int_0^T dt\, \langle \Phi(\beta)|\sigma_0^y(t)|\Phi(\beta)\rangle &= 0.00(0.05) \\
\frac{1}{T}\int_0^T dt\, \langle \Phi(\beta)|\sigma_0^z(t)|\Phi(\beta)\rangle &= -0.01(0.05),
\end{aligned} \tag{6.19}$$

where the numbers in parenthesis give the standard deviation. For $N_{\rm B} = 28$ and for the time interval $[0, T]$ with $T = 200$ we find

$$\begin{aligned}
\frac{1}{T}\int_0^T dt\, \langle \Phi(\beta)|\sigma_0^x(t)|\Phi(\beta)\rangle &= 0.76(0.01) \\
\frac{1}{T}\int_0^T dt\, \langle \Phi(\beta)|\sigma_0^y(t)|\Phi(\beta)\rangle &= 0.00(0.01) \\
\frac{1}{T}\int_0^T dt\, \langle \Phi(\beta)|\sigma_0^z(t)|\Phi(\beta)\rangle &= 0.00(0.01),
\end{aligned} \tag{6.20}$$

indicating that for most practical purposes, a bath of $N_{\rm B} = 28$ spin may be sufficiently large to mimic an infinitely large bath. The numbers in Eq. (6.20) also give an indication of the statistical fluctuations that we may expect for a bath containing $N_{\rm B} = 28$ spins. For the model parameters and the value of λ chosen, the second-order corrections in λ are of the order of 0.01 and are hidden in the statistical fluctuations, suggesting that values of $\lambda \leq 0.1$ are within the perturbative regime.

The latter statement is not as obvious as it may seem. To first order in λ, we have

$$\langle \sigma_0^x \rangle = \langle \sigma_0^x \rangle_{\rm S} - \beta\lambda \left(\langle \sigma_0^x \rangle_{\rm S} - 1 \right) \langle B^x \rangle_{\rm B}, \tag{6.21}$$

where $\langle . \rangle_{\rm S}$ and $\langle . \rangle_{\rm B}$ denote the thermal equilibrium averages with respect to the system and bath, respectively. For the sake of argument, consider the case that $K = 0$, $h_n^z = 0$

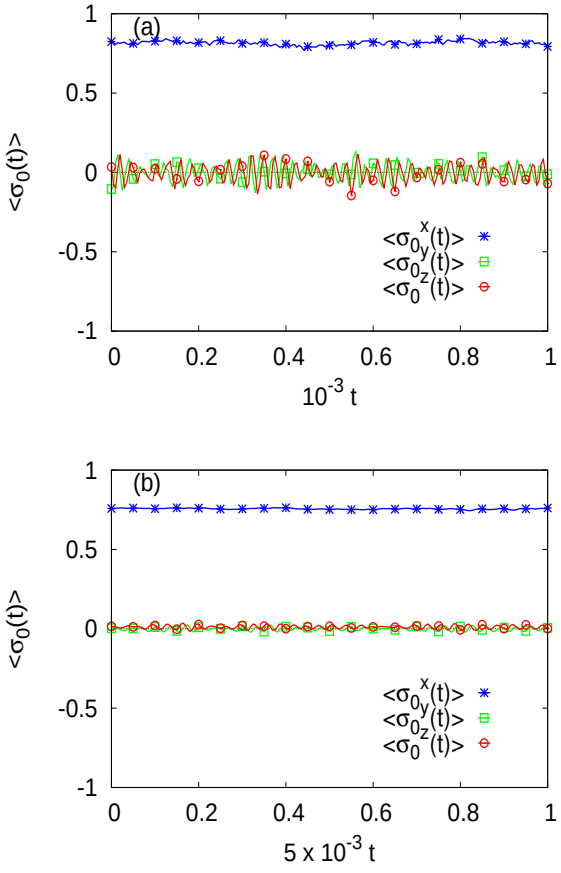

Figure 6.1: (color online) Time evolution of the average of the system spin as obtained by solving the TDSE with a random thermal state at $\beta = 2$ as the initial state. The Hamiltonian of the bath is given by Eq. (6.5) with $K = -1/4$ and $\Delta = 1$ (antiferromagnetic Heisenberg model), The parameters of the system-bath Hamiltonian Eq. (6.3) are $J = 1/4$ and $h_{\mathrm{B}}^{x} = h_{\mathrm{B}}^{z} = 1/8$. The system-bath interaction $\lambda = 0.1$. (a) $N_{\mathrm{B}} = 13$; (b) $N_{\mathrm{B}} = 28$. Lines connecting the data points are guide to the eye.

and $h_n^x = h_B^x$ for all $n = 1, \ldots, N_B$ (the same reasoning applies to the contributions of second order in λ). Then, Eq. (6.21) becomes

$$\langle \sigma_0^x \rangle = \tanh(\beta h^x) + \beta\lambda N_B (1 - \tanh(\beta h^x)) \tanh(\beta h_B^x), \tag{6.22}$$

showing that the contribution of the "perturbation term" increases with the number of spins in the bath. In other words, it is not sufficient to consider small values of λ. For the perturbation by the bath to be weak, it is necessary that λN_B is small. In this respect the spin bath considered in this chapter is not different from e.g. the standard spin-boson model [113]. In our simulation work, we adopt a pragmatic approach: we simply compute the averages and compare them with the theoretical results of the isolated system (as we did above). The coupling λ is considered to be small enough if the corrections are hidden in the statistical fluctuations.

6.4 Quantum master equation: generalities

We are interested in the dynamics of a system, the degrees of freedom of which interact with other degrees of freedom of a "bath", "environment", etc. The combination of system + bath forms a closed quantum system. When we consider the system only, we say that we are dealing with an open quantum system. The quantum state of the system + bath is represented by the density matrix $\rho = \rho(t)$ which evolves in time according to

$$\frac{\partial \rho(t)}{\partial t} = i[\rho(t), H], \tag{6.23}$$

where H is the Hamiltonian of the system + bath (recall that we adopt units such that $\hbar = 1$).

The "relevant" part of the dynamics may formally be separated from the "uninteresting" part by using the Nakajima-Zwanzig projection operator formalism [111, 112]. Let $\mathcal{P}$ be the projector onto the "relevant" part and introduce the Liouville operator $\mathcal{L}A = i[A, H]$. Denoting by $\mathcal{Q} = 1 - \mathcal{P}$ the projector on the "uninteresting" part, it follows that

$$\frac{\partial \mathcal{P}\rho(t)}{\partial t} = \mathcal{P}\mathcal{L}\mathcal{P}\rho(t) + \mathcal{P}\mathcal{L}\mathcal{Q}\rho(t), \tag{6.24}$$

$$\frac{\partial \mathcal{Q}\rho(t)}{\partial t} = \mathcal{Q}\mathcal{L}\mathcal{P}\rho(t) + \mathcal{Q}\mathcal{L}\mathcal{Q}\rho(t). \tag{6.25}$$

Note that because H is Hermitian, $i\mathcal{L}$, $i\mathcal{P}\mathcal{L}\mathcal{P}$ and $i\mathcal{Q}\mathcal{L}\mathcal{Q}$ are Hermitian too. The formal solution of the matrix-valued, inhomogeneous, linear, first-order differential

equation Eq. (6.25) reads as

$$\mathcal{Q}\rho(t) = e^{t\mathcal{Q}\mathcal{L}\mathcal{Q}}\mathcal{Q}\rho(t=0) + \int_0^t du\, e^{u\mathcal{Q}\mathcal{L}\mathcal{Q}}\mathcal{Q}\mathcal{L}\mathcal{P}\rho(t-u), \tag{6.26}$$

as can be verified most easily by calculating its derivative with respect to time and using $\mathcal{P}\mathcal{P} = \mathcal{P}$, $\mathcal{P}\mathcal{Q} = \mathcal{Q}\mathcal{P} = 0$ and $\mathcal{Q}\mathcal{Q} = \mathcal{Q}$. Substituting Eq. (6.26) into Eq. (6.24) yields

$$\frac{\partial\mathcal{P}\rho(t)}{\partial t} = \mathcal{P}\mathcal{L}\mathcal{P}\rho(t) + \mathcal{P}\mathcal{L}\mathcal{Q}e^{t\mathcal{Q}\mathcal{L}\mathcal{Q}}\mathcal{Q}\rho(t=0) + \int_0^t du\, \mathcal{P}\mathcal{L}\mathcal{Q}e^{u\mathcal{Q}\mathcal{L}\mathcal{Q}}\mathcal{Q}\mathcal{L}\mathcal{P}\rho(t-u). \tag{6.27}$$

We are primarily interested in the time evolution of the system. Therefore, we choose $\mathcal{P}$ such that it projects onto the system variables and we perform the trace over the bath degrees-of-freedom. A common choice for the projector $\mathcal{P}$ is [113, 117, 122, 128, 130, 131]

$$\mathcal{P}A = \rho_{\mathrm{B}}\mathbf{Tr}_{\mathrm{B}}\, A, \tag{6.28}$$

where

$$\rho_{\mathrm{B}} = \frac{e^{-\beta H_{\mathrm{B}}}}{\mathbf{Tr}_{\mathrm{B}}\, e^{-\beta H_{\mathrm{B}}}}, \tag{6.29}$$

is the density matrix of the bath in thermal equilibrium. Accordingly, the density matrix of the system is given by

$$\rho_{\mathrm{S}}(t) = \mathbf{Tr}_{\mathrm{B}}\mathcal{P}\rho(t) = \mathbf{Tr}_{\mathrm{B}}\rho(t), \tag{6.30}$$

consistent with Eq. (6.12).

In the present work, we will mostly consider initial states that are represented by the direct-product ansatz

$$\rho(t=0) = \rho_{\mathrm{S}}\rho_{\mathrm{B}},. \tag{6.31}$$

but occasionally, we also consider as an initial state, the thermal equilibrium state of the system + bath, that is $\rho(t=0) = e^{-\beta H}/\mathbf{Tr}\; e^{-\beta H}$, see Sec. 6.3.2. The direct-product ansatz Eq. (6.31) not only implies $\mathcal{Q}\rho(t=0) = 0$ but also defines the initial condition for Eq. (6.27). In general, this initial condition may be incompatible with the initial condition for the TDSE of the whole system, which may affect the dynamics on a time-scale comparable to the relaxation time of the bath [130].

Adopting Eq. (6.31), Eq. (6.27) simplifies to

$$\frac{\partial\rho_{\mathrm{S}}(t)}{\partial t} = \mathbf{Tr}_{\mathrm{B}}\mathcal{P}\mathcal{L}\mathcal{P}\rho(t) + \int_0^t du\, \mathbf{Tr}_{\mathrm{B}}\mathcal{P}\mathcal{L}\mathcal{Q}e^{u\mathcal{Q}\mathcal{L}\mathcal{Q}}\mathcal{Q}\mathcal{L}\mathcal{P}\rho(t-u), \tag{6.32}$$

which is not a closed equation for $\rho_{\mathrm{S}}(t)$ yet [128].

Using the explicit form of the Hamiltonian Eq. (6.1), the first term in Eq. (6.32) may be written as $\mathbf{Tr}_{\mathrm{B}}\mathcal{P}\mathcal{L}\mathcal{P}\rho(t) = \mathcal{L}_0\rho_{\mathrm{S}}(t)$ where for any system operator X_{S},

$$\mathcal{L}_0 X_{\mathrm{S}} \equiv -i\left\{[H_S, X_{\mathrm{S}}(t)] + \sum_{i=1}^{3}\langle B_i\rangle_{\mathrm{B}}\left[\sigma_0^i, X_{\mathrm{S}}(t)\right]\right\}, \tag{6.33}$$

and $\langle B_i\rangle_{\mathrm{B}} \equiv \mathbf{Tr}_{\mathrm{B}}\rho_{\mathrm{B}}B_i$. Therefore, Eq. (6.32) may be written as

$$\frac{\partial\rho_{\mathrm{S}}(t)}{\partial t} = \mathcal{L}_0\rho_{\mathrm{S}}(t) + \int_0^t du\ \mathbf{Tr}_{\mathrm{B}}\mathcal{P}\mathcal{L}\mathcal{Q}e^{(t-u)\mathcal{Q}\mathcal{L}\mathcal{Q}}\mathcal{Q}\mathcal{L}\rho_{\mathrm{B}}\rho_{\mathrm{S}}(u). \tag{6.34}$$

Using representation Eq. (6.14), multiplying both sides of Eq. (6.34) by σ_0^j, performing the trace over the system degree of freedom, and denoting $\rho(t) = (\rho_1(t), \rho_2(t), \rho_3(t))$, Eq. (6.34) can be written as

$$\frac{\partial\rho(t)}{\partial t} = \mathbf{L}\rho(t) + \int_0^t du\ \mathbf{M}(t-u)\rho(u) + \int_0^t du\ \mathbf{K}(u), \tag{6.35}$$

where

$$\begin{aligned}
\mathbf{L}_{jk} &= \frac{1}{2}\mathbf{Tr}_{\mathrm{S}}\sigma_0^j\mathcal{L}_0\sigma_0^k \\
\mathbf{M}_{jk}(u) &= \frac{1}{2}\mathbf{Tr}\ \sigma_0^j\mathcal{P}\mathcal{L}\mathcal{Q}e^{u\mathcal{Q}\mathcal{L}\mathcal{Q}}\mathcal{Q}\mathcal{L}\rho_{\mathrm{B}}\sigma_0^k \\
\mathbf{K}_j(u) &= \frac{1}{2}\mathbf{Tr}\ \sigma_0^j\mathcal{P}\mathcal{L}\mathcal{Q}e^{u\mathcal{Q}\mathcal{L}\mathcal{Q}}\mathcal{Q}\mathcal{L}\rho_{\mathrm{B}}.
\end{aligned} \tag{6.36}$$

As we have only made formal manipulations, solving Eq. (6.35) of the system is just as difficult as solving Eq. (6.23) of the whole system. In other words, in order to make progress, it is necessary to make approximations. A common route to derive an equation which can actually be solved is to assume that λ is sufficiently small such that perturbation theory may be used to approximate the second term in Eq. (6.34) and that it is allowed to replace $\rho_{\mathrm{S}}(u)$ in Eq. (6.34) by $\rho_{\mathrm{S}}(t)$ [113].

As the purpose of the present work is to scrutinize the approximations just mentioned by comparing the solution obtained from the Markovian quantum master equation with the one obtained by solving the TDSE, we will not dwell on the justification of these approximations and derivation of this equation itself, but merely state that the result of making these approximations is an equation that may be cast in the form

$$\boxed{\frac{\partial\boldsymbol{\rho}(t)}{\partial t} = \mathbf{A}\boldsymbol{\rho}(t) + \mathbf{b}.} \tag{6.37}$$

In the following we will refer to Eq. (6.37) as "the" quantum master equation (QMEQ). In Sec. 6.4.1 we give a well-known example of a quantum master equation that is of the form Eq. (6.37).

The formal solution of Eq. (6.37) reads as

$$\boldsymbol{\rho}(t) \quad = \quad e^{t\mathbf{A}}\boldsymbol{\rho}(0) + \int_0^t e^{(t-u)\mathbf{A}}\mathbf{b}\, du, \tag{6.38}$$

or, equivalently

$$\boldsymbol{\rho}(t+\tau) \quad = \quad e^{\tau\mathbf{A}}\boldsymbol{\rho}(t) + \int_0^\tau e^{(\tau-u)\mathbf{A}}\mathbf{b}\, du = e^{\tau\mathbf{A}}\boldsymbol{\rho}(t) + \mathbf{B}, \tag{6.39}$$

where

$$\mathbf{B} = \int_0^\tau e^{(\tau-u)\mathbf{A}}\mathbf{b}\, du, \tag{6.40}$$

does not depend on time. Equation (6.39) directly connects to the numerical work because in practice, we solve the TDSE with a finite time step τ.

Generally speaking, as a result of the coupling to the bath, the system is expected to exhibit relaxation towards a stationary state, meaning that $\boldsymbol{\rho}(t) \approx \boldsymbol{\rho}(\infty)$ for t sufficiently large. If such a stationary state exists, it follows from Eq. (6.39) that $\boldsymbol{\rho}(\infty) \approx e^{\tau\mathbf{A}}\boldsymbol{\rho}(\infty) + \mathbf{B}$ or that $\mathbf{B} \approx (1 - e^{\tau\mathbf{A}})\boldsymbol{\rho}(\infty)$, yielding

$$\boldsymbol{\rho}(t+\tau) - \boldsymbol{\rho}(\infty) \quad \approx \quad e^{\tau\mathbf{A}}(\boldsymbol{\rho}(t) - \boldsymbol{\rho}(\infty)). \tag{6.41}$$

Equation (6.41) suggests that the existence of a stationary state implies that there is no need to determine $\mathbf{B}$. However, numerical experiments with the Bloch equation model (see Appendix A) show that using Eq. (6.41), a least-square fit to solution of the Bloch equation often fails to yield the correct $e^{\tau\mathbf{A}}$. Therefore, as explained in Sec. 6.5, we will use Eq. (6.39) and determine both $e^{\tau\mathbf{A}}$ and $\mathbf{B}$ by least-square fitting to TDSE or Bloch equation data.

We can now formulate more precisely, the procedure to test whether or not a quantum master equation of the form Eq. (6.37) provides a good approximation to the data $\rho_k(t) = \langle\sigma^k(t)\rangle$ obtained by solving the TDSE of the system interacting with the bath using a time step τ. To this end, we use the latter data to determine the matrix $e^{\tau\mathbf{A}}$ and vector $\mathbf{B}$ such that, in a least square sense, the difference between the data obtained by solving Eq. (6.39) for a substantial interval of time and the corresponding TDSE data is as small as possible. If the values of $\boldsymbol{\rho}(t)$ computed according to Eq. (6.39) are in good agreement with the data $\rho_k(t)$, one might say that at least for the particular time interval studied, there exists a mapping of the Schrödinger dynamics of the system onto the QMEQ Eq. (6.37).

6.4.1 Markovian quantum master equation: Example

We consider the Redfield master equation [18] under the Markovian assumption [113, 117]

$$\begin{aligned}\frac{d\rho_{\rm S}(t)}{dt} &= -i[H_S,\rho_{\rm S}(t)] \\ &\quad + \lambda^2 \sum_{j=1}^{3} \Big(R_j \rho_{\rm S}(t)\sigma_j + \sigma_j \rho_{\rm S}(t) R_j^\dagger - \sigma_j R_j \rho_{\rm S}(t) - \rho_{\rm S}(t) R_j^\dagger \sigma_j \Big) ,\end{aligned} \tag{6.42}$$

where $\rho_{\rm S}(t)$ is the density matrix of the system. The operators R_j are given by [117]

$$R_j \;=\; \sum_{k=1}^{3} \int_0^\infty dt\; C_{jk}(t) e^{-itH_s} \sigma_k e^{+itH_s} \quad , \quad j=1,2,3, \tag{6.43}$$

where $C_{jk}(t) = \mathbf{Tr}_{\rm B} \rho_{\rm B} B_j(t) B_k(0)$ are the correlations of the bath operators [117]. The specific form of $C_{jk}(t)$ is not of interest to us at this time (but also see Sec. 6.7). For what follows, it is important that the specific form Eq. (6.43) of the operators R_j allows us to write

$$R_j \;=\; \sum_{k=1}^{3} r_{jk} \sigma_k, \tag{6.44}$$

where

$$\begin{aligned} r_{j1} &= \int_0^\infty dt\; C_{j1}(t) \\ r_{j2} &= \int_0^\infty dt\; \left(C_{j2}(t)\cos 2h^x t + C_{j3}(t) \sin 2h^x t \right) \\ r_{j3} &= \int_0^\infty dt\; \left(C_{j3}(t)\cos 2h^x t - C_{j2}(t) \sin 2h^x t \right) , \end{aligned} \tag{6.45}$$

do not depend on time (due to the Markov approximation).

As a first step, we want to derive from Eq. (6.42), the corresponding equations in terms of the $\rho_k(t)$'s. This can be done by using representation Eq. (6.14), multiplying both sides of Eq. (6.42) with σ_k for $k=1,2,3$ and taking the trace, a calculation for which we resort to Mathematica®. We obtain

$$\begin{aligned} \frac{d\rho_1}{dt} &= +4\lambda^2 \left[\left(r_{23}^{\rm I} - r_{32}^{\rm I} \right) - \left(r_{22}^{\rm R} + r_{33}^{\rm R} \right) \rho_1 + r_{21}^{\rm R} \rho_2 + r_{31}^{\rm R} \rho_3 \right] \\ \frac{d\rho_2}{dt} &= +h^x \rho_3 + 4\lambda^2 \left[\left(r_{31}^{\rm I} - r_{13}^{\rm I} \right) + r_{12}^{\rm R} \rho_1 - \left(r_{11}^{\rm R} + r_{33}^{\rm R} \right) \rho_2 + r_{32}^{\rm R} \rho_3 \right] \\ \frac{d\rho_3}{dt} &= -h^x \rho_2 + 4\lambda^2 \left[r_{12}^{\rm I} - r_{21}^{\rm I} + r_{13}^{\rm R} \rho_1 + r_{23}^{\rm R} \rho_2 - \left(r_{11}^{\rm R} + r_{22}^{\rm R} \right) \rho_3 \right] , \end{aligned} \tag{6.46}$$

where we used the notation $z = z^{\rm R} + i z^{\rm I}$. It directly follows that Eq. (6.46) can be written in the form Eq. (6.37). It is straightforward to show that this holds for quantum master equations of the Lindblad form as well.

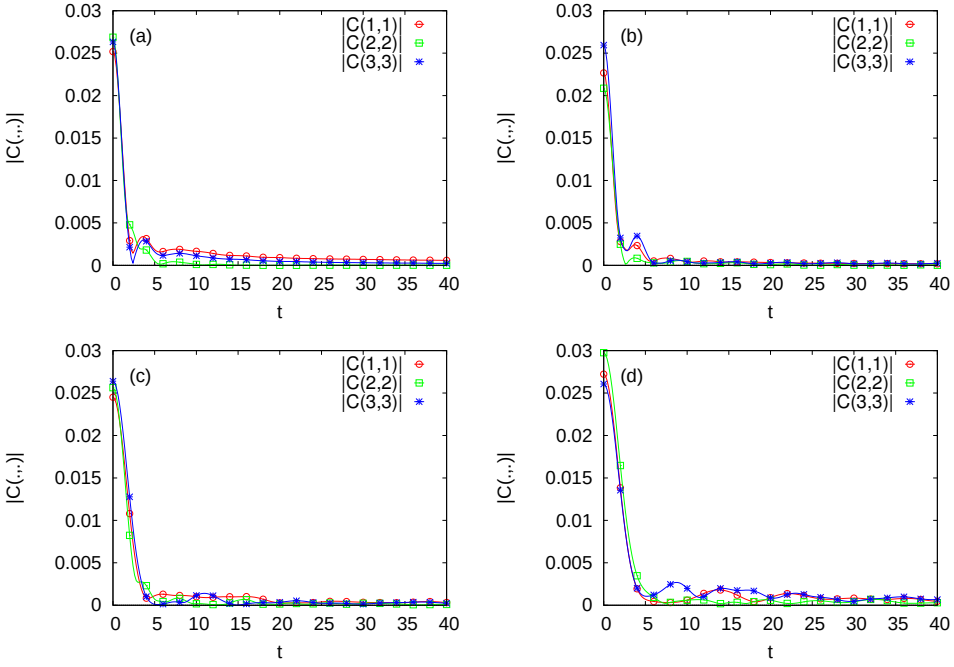

Figure 6.2: (color online) The absolute values of three of the nine bath-operator correlations Eq. (6.47) as obtained by solving the TDSE for a bath of $N_{\rm B} = 32$ spins with a random thermal state at $\beta = 1$ as the initial state. The bath-operator correlations that have absolute values that are too small to be seen on the scale of the plot have been omitted. The parameters of the system-bath Hamiltonian $H_{\rm SB}$ are $J = 1/4$ and $h^x_{\rm B} = h^z_{\rm B} = 1/8$. (a) the bath Hamiltonian $H_{\rm B}$ is given by Eq. (6.5) with $K = -1/4$ and $\Delta = 1$ (antiferromagnetic Heisenberg model) and $\lambda = 0$; (b) same as (a) except that $\lambda = 0.1$; (c) the bath Hamiltonian $H_{\rm B}$ is given by Eq. (6.6) with $K = 1/4$ and $\lambda = 0$; (d) same as (a) except that $\lambda = 0.1$.

6.4.2 Bath correlations

A crucial assumption in deriving the QMEQ Eq. (6.37) from the exact equation Eq. (6.34) is that the correlations of the bath decay on a short time scale, short relative to the time scale of the motion of the system spin [113]. Moreover, in the perturbative derivation of quantum master equations, such as the Redfield master equation, it is assumed that the time evolution of the bath operators is governed by the bath Hamiltonian only [113].

Having the time evolution of the whole system at our disposal, we can compute, without additional assumptions or approximations, the correlations

$$C(i,j,t) = \mathbf{Tr}\rho(t=0)B_i(t)B_j(0) \quad , \quad i,j = 1,2,3, \tag{6.47}$$

of the bath operators Eq. (6.4). Note that in general, Eq. (6.47) is complex-valued and that, because of the choice Eq. (6.31), $C(i,j,t) = C_{ij}(t)$ if $\lambda = 0$. Of particular interest is the question whether, for the chosen value of the system-bath interaction λ, the dynamics of the system spin significantly affects the bath dynamics.

In Fig. 6.2 we present simulation results of the correlations $|C(i,i,t)|$ for a bath of $N_{\mathrm{B}} = 32$ spins, for different choices of the bath Hamiltonian, and with and without system-bath interaction. The calculation of the nine correlations Eq. (6.47) requires solving four TDSEs simultaneously, using as the initial states the random thermal state $|\Psi(\beta)\rangle$, $B_1|\Psi(\beta)\rangle$, $B_2|\Psi(\beta)\rangle$, and $B_3|\Psi(\beta)\rangle$. As the whole system contains 33 spins, these calculations are fairly expensive in terms of CPU and memory cost. One such calculation needs somewhat less than 1TB memory to run and takes about 5 hours using 65536 BlueGene/Q processors which, in practice, limits the time interval that can be studied.

In all four cases, the absolute values of correlations for $i \neq j$ are much smaller than those for $i = j$ and have therefore been omitted in Fig. 6.2. The remaining three correlations decay rapidly but, on the time scale shown, are definitely non-zero at $t = 20$. Comparison of the top and bottom figures of Fig. 6.2 may suggest that the bath correlations decay faster if the bath is described by the antiferromagnetic Heisenberg model (6.5) than if the bath Hamiltonian has random couplings [see Eq. (6.6)]. However, this is a little misleading. For the bath Hamiltonian with random couplings K_n^α in the range $[-1/4, 1/4]$, we have $\langle|K_n^\alpha|\rangle \approx 1/8$. On the other hand, for the antiferromagnetic Heisenberg bath we have $K = -1/4$ roughly indicating that the bath dynamics may be about two times faster than in the case of the bath Hamiltonian with random couplings. The presence of random couplings renders the quantitative comparison of the relaxation times non-trivial. However, from Fig. 6.2 it is clear that as a bath, the antiferromagnetic Heisenberg model performs better than the model with random interactions in the sense that for $t > 10$ the correlations of the former seem to have reached a stationary state whereas in the case of the latter, they do not.

Moreover, using the full Hamiltonian ($\lambda = 0.1$) instead of only the bath Hamiltonian to solve the TDSE, for $t > 10$ the changes to the correlations are less pronounced if the bath is an antiferromagnetic Heisenberg model than if the bath has random interactions. Based on these results, it seems advantageous to adopt the antiferromagnetic Heisenberg model ($K = -1/4$) as the Hamiltonian of the bath.

Qualitatively, in all cases, the correlations are either small for all t or decrease by about order of magnitude on a short time scale ($t < 10$), indicating that the approximations that changed Eq. (6.35) into Eq. (6.37) may apply to the spin model we are considering.

6.5 Algorithm to extract $e^{\tau \mathbf{A}}$ and B from TDSE data

Recall that our primary objective is to determine the Markovian master equation Eq. (6.37) which gives the best (in the least-square sense) fit to the solution of the TDSE. Obviously, this requires taking into account the full motion of the system spin, not only the decay envelope, over an extended period of time.

The numerical solution of the TDSE of the full problem yields the data $\rho_k(t) = \langle \sigma^k(t) \rangle$. In this section, we consider these data as given and discuss the algorithm that takes as input the values of $\rho_k(t)$ and returns the optimal choice of the matrix $e^{\tau \mathbf{A}}$ and vector $\mathbf{B}$, meaning that we minimize the least-square error between the data $\{\rho_k(t)\}$ and the corresponding data, obtained by solving Eq. (6.39).

Denoting $\rho_k(n) \equiv \rho_k(n\tau)$, it follows that if Eq. (6.39) is assumed to hold, we must have

$$\begin{pmatrix} \rho_1(1) & \rho_1(2) & \dots & \rho_1(N) \\ \rho_2(1) & \rho_2(2) & \dots & \rho_2(N) \\ \rho_3(1) & \rho_3(2) & \dots & \rho_3(N) \end{pmatrix} = \begin{pmatrix} (e^{\tau \mathbf{A}})_{11} & (e^{\tau \mathbf{A}})_{12} & (e^{\tau \mathbf{A}})_{13} & (\mathbf{B})_1 \\ (e^{\tau \mathbf{A}})_{21} & (e^{\tau \mathbf{A}})_{22} & (e^{\tau \mathbf{A}})_{23} & (\mathbf{B})_2 \\ (e^{\tau \mathbf{A}})_{31} & (e^{\tau \mathbf{A}})_{32} & (e^{\tau \mathbf{A}})_{33} & (\mathbf{B})_3 \end{pmatrix} \begin{pmatrix} \rho_1(0) & \rho_1(1) & \dots & \rho_1(N-1) \\ \rho_2(0) & \rho_2(1) & \dots & \rho_2(N-1) \\ \rho_3(0) & \rho_3(1) & \dots & \rho_3(N-1) \\ 1 & 1 & 1 & 1 \end{pmatrix}, \tag{6.48}$$

where N is the number of time steps for which the solution of the TDSE is known. We may write Eq. (6.48) in the more compact form

$$\mathbf{Z} = \mathbf{Y}\mathbf{X}, \tag{6.49}$$

where $\mathbf{Z}$ is a $3 \times N$ matrix of data, $\mathbf{Y}$ is a 3×4 matrix that we want to determine, and $\mathbf{X}$ is a $4 \times N$ matrix of data.

We determine $\mathbf{Y}$ by solving the linear least square problem, that is we search for the solution of the problem $\min_{\mathbf{Y}} ||\mathbf{Z} - \mathbf{Y}\mathbf{X}||^2$. A numerically convenient way to solve this minimization problem is to compute the singular value decomposition [148, 149] of $\mathbf{X} = \mathbf{U}\mathbf{\Sigma}\mathbf{V}^T$ where $\mathbf{U}$ is an orthogonal 3×3 matrix, $\mathbf{\Sigma}$ is the $3 \times N$ matrix with the singular values of $\mathbf{X}$ on its diagonal, and $\mathbf{V}^T$ is an orthogonal $N \times N$ matrix. In terms of these matrices we have

$$\mathbf{Y} = \mathbf{Z}\mathbf{V}\mathbf{\Sigma}^{+}\mathbf{U}^T, \tag{6.50}$$

where $\mathbf{\Sigma}^{+}$ is the pseudo-inverse of $\mathbf{\Sigma}$, which is formed by replacing every non-zero diagonal entry of $\mathbf{\Sigma}$ by its reciprocal and transposing the resulting matrix.

Numerical experiments show that the procedure outlined above is not robust: it sometimes fails to reproduce the known $e^{\tau\mathbf{A}}$ and $\mathbf{B} = 0$, in particular in the case that $e^{\tau\mathbf{A}}$ is (close to) an orthogonal matrix. Fortunately, a straightforward extension renders the procedure very robust. The key is to use data from three runs with different initial conditions. This also reduces the chance that the estimates of $e^{\tau\mathbf{A}}$ and $\mathbf{B}$ are good by accident. In practice, we take the initial states to be orthogonal (see Sec. 6.6 for the precise specification).

Labeling the data for different initial states by superscripts we have

$$\begin{pmatrix} \mathbf{Z}^{(1)} & \mathbf{Z}^{(2)} & \mathbf{Z}^{(3)} \end{pmatrix} = \mathbf{Y} \begin{pmatrix} \mathbf{X}^{(1)} & \mathbf{X}^{(2)} & \mathbf{X}^{(3)} \end{pmatrix}, \tag{6.51}$$

but now $\mathbf{Z} = (\mathbf{Z}^{(1)}\,\mathbf{Z}^{(2)}\,\mathbf{Z}^{(3)})$ and $\mathbf{X} = (\mathbf{X}^{(1)}\,\mathbf{X}^{(2)}\,\mathbf{X}^{(3)})$ are $3\times 3N$ and $4\times 3N$ matrices of data, respectively. Using Eq. (6.50) we compute

$$\mathbf{Y} = \begin{pmatrix} (e^{\tau\mathbf{A}})_{11} & (e^{\tau\mathbf{A}})_{12} & (e^{\tau\mathbf{A}})_{13} & (\mathbf{B})_1 \\ (e^{\tau\mathbf{A}})_{21} & (e^{\tau\mathbf{A}})_{22} & (e^{\tau\mathbf{A}})_{23} & (\mathbf{B})_2 \\ (e^{\tau\mathbf{A}})_{31} & (e^{\tau\mathbf{A}})_{32} & (e^{\tau\mathbf{A}})_{33} & (\mathbf{B})_3 \end{pmatrix}, \tag{6.52}$$

from which the matrix $e^{\tau\mathbf{A}}$ and vector $\mathbf{B}$ immediately follow. In Appendix A, we discuss the method that we used to validate the extraction method.

6.6 Fitting a quantum master equation to the solution of the TDSE

The procedure to test the hypothesis as to whether the QMEQ Eq. (6.37) provides a good approximation to the exact TDSE of a (small) system which is weakly coupled to a (large) environment can be summarized as follows:

1. Make a choice for the model parameters h_{B}^x, h_{B}^z, K, Δ, and the system-bath interaction λ, for the number of bath spins N_{B}, the inverse temperature β of the bath, and the time step τ ($\tau = 1$ unless mentioned explicitly).

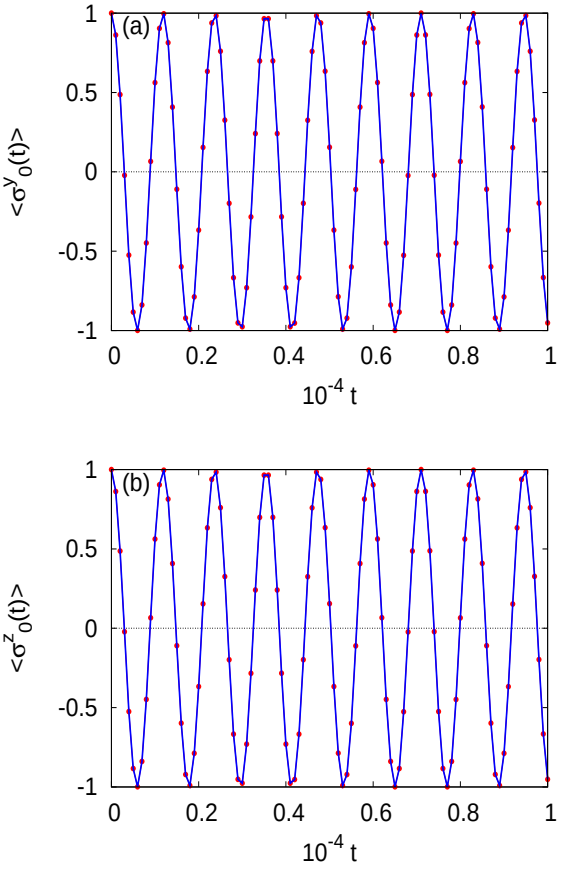

Figure 6.3: (color online) Comparison between the spin averages as obtained by solving the TDSE (solid lines) and the QMEQ (solid circles) with $e^{\tau \mathbf{A}}$ and $\mathbf{B}$ extracted from the TDSE data. (a) initial state $|y\rangle|\phi\rangle$; (b) initial state $|\uparrow\rangle|\phi\rangle$. The model parameters are: $\lambda = 0$, $N_{\rm B} = 13$, $\beta = 0$, $K = -1/4$, $\Delta = 1$ and $h^x_{\rm B} = h^z_{\rm B} = 1/8$. For clarity, the system-spin averages are shown with a time interval of 100. The markers represent the data obtained by least-square fitting to 15000 numbers generated by the TDSE solver.

2. Prepare three initial states $|\Psi(0)\rangle_x = |x\rangle|\phi\rangle$, $|\Psi(0)\rangle_y = |y\rangle|\phi\rangle$, and $|\Psi(0)\rangle_z = |\uparrow\rangle|\phi\rangle$ where $|x\rangle = (|\uparrow\rangle + |\downarrow\rangle)/\sqrt{2}$, $|y\rangle = (|\uparrow\rangle + i|\downarrow\rangle)/\sqrt{2}$, and $|\phi\rangle$ denotes a pure state picked randomly from the 2^{N_B}-dimensional unit hypersphere. For each of the three initial states we may or may not use different realizations of $|\phi\rangle$. If $\beta > 0$, prepare typical thermal states by projection [147], that is set $|\Psi(0)\rangle_x = |x\rangle|\phi(\beta/2)\rangle/\langle\phi(\beta/2)|\phi(\beta/2)\rangle^{1/2}$ (and similarly for the two other initial states) where $|\phi(\beta/2)\rangle = e^{-\beta H_B/2}|\phi\rangle$.

3. For each of the three initial states, solve the TDSE for $0 \leq t = n\tau \leq T = N\tau$. The case of interest is when T is large enough for the system-bath to reach a steady state. For each of the three different initial states compute $\rho_{i,j}(k) \equiv \langle\Psi(k\tau)|\sigma_0^i|\Psi(k\tau)\rangle_j$, for $i, j = x, y, z$ and store this data.

4. Use the data $\rho_{i,j}(k)$ to construct the $3 \times 3N$ matrix $\mathbf{Z} = (\mathbf{Z}^{(1)}\,\mathbf{Z}^{(2)}\,\mathbf{Z}^{(3)})$ and $4 \times 3N$ matrix $\mathbf{X} = (\mathbf{X}^{(1)}\,\mathbf{X}^{(2)}\,\mathbf{X}^{(3)})$ [see Eq. (6.51)] and compute the 3×4 matrix $\mathbf{Y}$, yielding the best (in the least-square sense) estimates of $e^{\tau\mathbf{A}}$ and $\mathbf{B}$.

5. Use the estimates of $e^{\tau\mathbf{A}}$ and $\mathbf{B}$ to compute the averages [denoted by $\widetilde{\rho}_{i,j}(k)$] of the three components of the system spin operators $\boldsymbol{\sigma}_0(t)$, according to Eq. (6.39) for each of the three different initial states. Quantify the difference of the reconstructed data, i.e. the solution of the "best" approximation in terms of the QMEQ, and the original data obtained by solving the TDSE by the number

$$e_{\max}(t = k\tau) = \max_{i,j} |\rho_{i,j}(k) - \widetilde{\rho}_{i,j}(k)|. \tag{6.53}$$

6. Check if the approximate density matrix of the system, defined by $\widetilde{\rho}_{i,j}(k)$, is non-negative definite. In none of our simulation runs the approximate density matrix of the system failed this test.

Test of the procedure to fit Eq. (6.37) to TDSE data

If the system does not interact with the bath ($\lambda = 0$), the system spin simply performs Larmor rotations in the magnetic field $\mathbf{H} = (h^x, 0, 0)$. Therefore, the $\lambda = 0$ case provides a simple, but as mentioned in Appendix A from the numerical viewpoint the most difficult case for the fitting procedure.

In Fig. 6.3, we present simulation results of the y- and z-components of the system spin as obtained by solving the TDSE with initial states $|y\rangle|\phi\rangle$ and $|\uparrow\rangle|\phi\rangle$, respectively. Looking at the time interval shown in Fig. 6.3 and recalling that the spin components perform oscillations with a period π/h^x, it is clear that Fig. 6.3 does not show these rapid oscillations. Instead, not to clutter the plots too much, we only plotted the values at regular intervals, as indicated by the markers. For the initial state $|x\rangle|\phi\rangle$, the x-component is exactly constant (both for the TDSE and time evolution using

the estimated $e^{\tau \mathbf{A}}$ and $\mathbf{B}$) and therefore not shown. The difference between the spin averages obtained from the TDSE and from time evolution according to Eq. (6.39) (using the estimated $e^{\tau \mathbf{A}}$ and $\mathbf{B}$) is rather small ($e_{\max}(t) < 10^{-5}$ for $0 \leq t \leq 10000$) and is therefore not shown either.

The small values of $e_{\max}(t)$ are reflected in the excellent agreement between the TDSE and QMEQ (Eq. (6.37)) data shown in Fig. 6.3. From these simulation data we conclude that for $\lambda = 0$, the matrix $e^{\tau \mathbf{A}}$ and vector $\mathbf{B}$ obtained by least-square fitting to the TDSE data define a QMEQ that reproduces the correct values of the spin averages.

The next step is to repeat the analysis for the case of weak system-bath interaction $\lambda = 0.05$ (recall that we already found that $\lambda = 0.1$ corresponds to a weak interaction). To head off misunderstandings, recall that our least-square procedure estimates the best $e^{\tau \mathbf{A}}$ and $\mathbf{B}$ using the data of three different solutions of the TDSE. It does not fit data for individual spin components separately nor does it fit data obtained from a TDSE solution of one particular choice of the initial state. Our procedure yields the best *global* estimates for $e^{\tau \mathbf{A}}$ and $\mathbf{B}$ in the least-square sense.

In Fig. 6.4 we illustrate the procedure for sampling and processing the TDSE data and for plotting these data along with the data obtained from Eq. (6.39) using the estimated $e^{\tau \mathbf{A}}$ and $\mathbf{B}$. We present data for short times (top figures) and for the whole time interval (bottom figures). The TDSE data (solid line) is being sampled, namely at times indicated by the t-values of the markers, which in the case corresponds to a time steps of 0.2 [see Figs. 6.4(a)–6.4(c)]. The sampled data of the whole interval $[0, 1000]$ are used to determine $e^{\tau \mathbf{A}}$ and $\mathbf{B}$ by the least-square procedure described in Sec. 6.5. In this particular case, the TDSE solver supplies 15000 numbers to the least-square procedure. The estimated $e^{\tau \mathbf{A}}$ and $\mathbf{B}$ thus obtained are then used to compute the time-evolution of the spin components, the data being represented by the markers.

From Fig. 6.4(d), it is clear that although the QMEQ produces the correct qualitative behavior of the x-component of the system spin, the difference with the TDSE data is significant (as is also clear from $e_{\max}(t)$). In particular, the TDSE data of the x-component of the system spin do not show relaxation to the thermal equilibrium value, which is zero for $\beta = 0$. At first sight, this could be a signature that the fitting procedure breaks down because it is certainly possible to produce a much better fit to the TDSE data of the x-component *if we would fit a curve to this data only*. But, as explained above, we estimate $e^{\tau \mathbf{A}}$ and $\mathbf{B}$ by fitting to the nine (three spin components $\times$ three different initial states) of such curves simultaneously. Apparently, the mismatch in the x-component is compensated for by the close match of the y–component [see Fig. 6.4(e) and z-component (not shown)].

Remarkably, the matrix $e^{\tau \mathbf{A}}$ and vector $\mathbf{B}$ extracted from the TDSE data yield

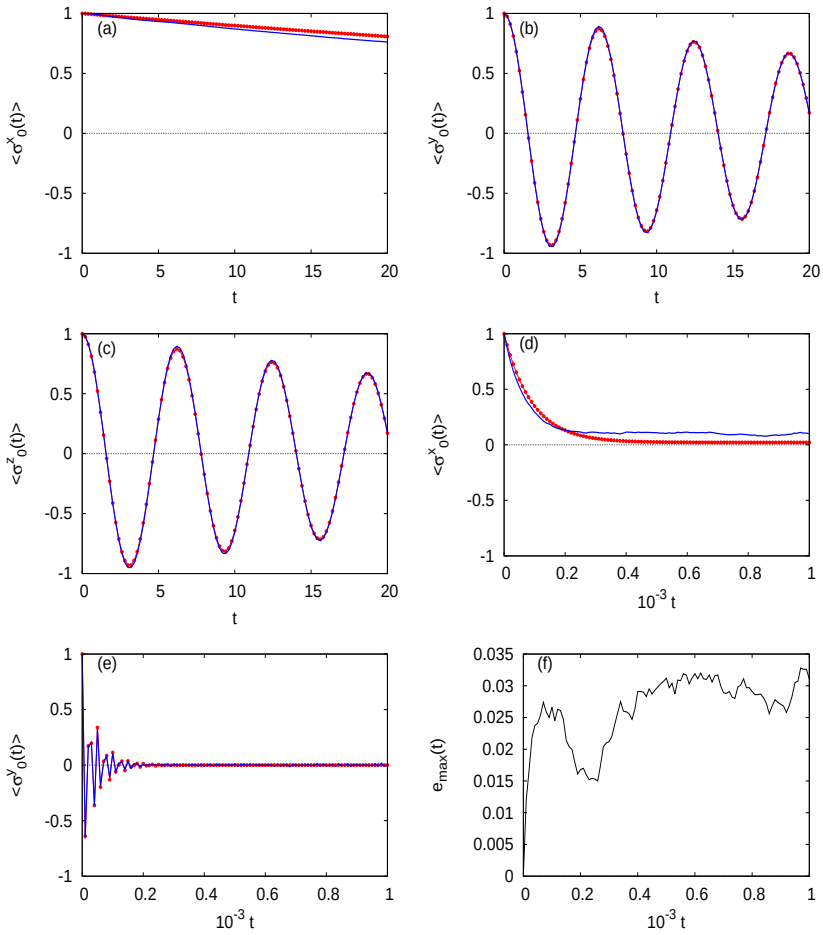

Figure 6.4: (color online) Comparison between the spin averages as obtained by solving the TDSE (solid lines) and the QMEQ (solid circles) with $e^{\tau \mathbf{A}}$ and $\mathbf{B}$ extracted from the TDSE data. (a)–(c) show how the TDSE data (solid line) are being sampled, namely at times indicated by the t-values of the markers, which in the case corresponds to a time steps of 0.2. (d)– (f): the sampled data of the whole interval $[0, 1000]$, in this case 15000 numbers, are used to determine by the least-square procedure described in Sec. 6.5, the parameters that enter the time-evolution of the Markovian master equation Eq. (6.37). The latter is then used to compute the time-evolution of the spin components, the data being represented by the markers. For clarity, in the bottom figures, the data are shown with a time interval of 10. The model parameters are: $h^x_{\rm B} = h^z_{\rm B} = 1/8$ and $\lambda = 0.1$, $N_{\rm B} = 13$, $\beta = 0$, $K = -1/4$, and $\Delta = 1$. (a),(d) initial state $|x\rangle|\phi\rangle$; (b),(e) initial state $|y\rangle|\phi\rangle$; (c) initial state $|z\rangle|\phi\rangle$; (f) the error $e_{\rm max}(t)$.

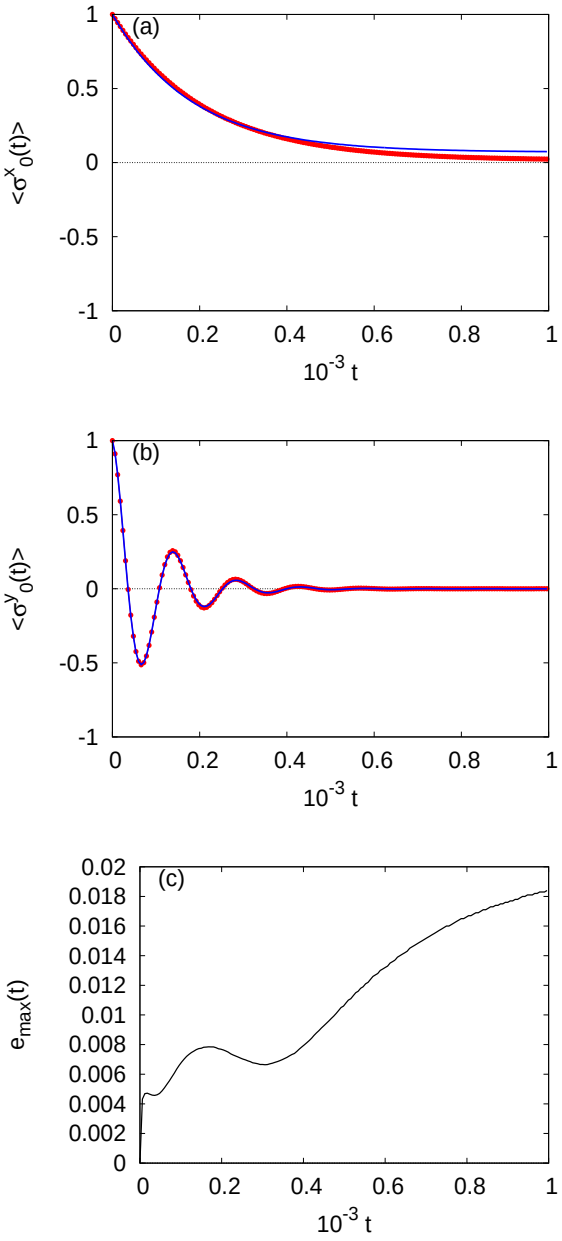

Figure 6.5: (color online) Same as Fig. 6.4, except that the bath contains $N_{\mathrm{B}} = 24$ spins and $\lambda = 0.05$. The markers represent the data obtained by least-square fitting to 15000 numbers generated by the TDSE solver. For clarity the data is shown with a time interval of 6.

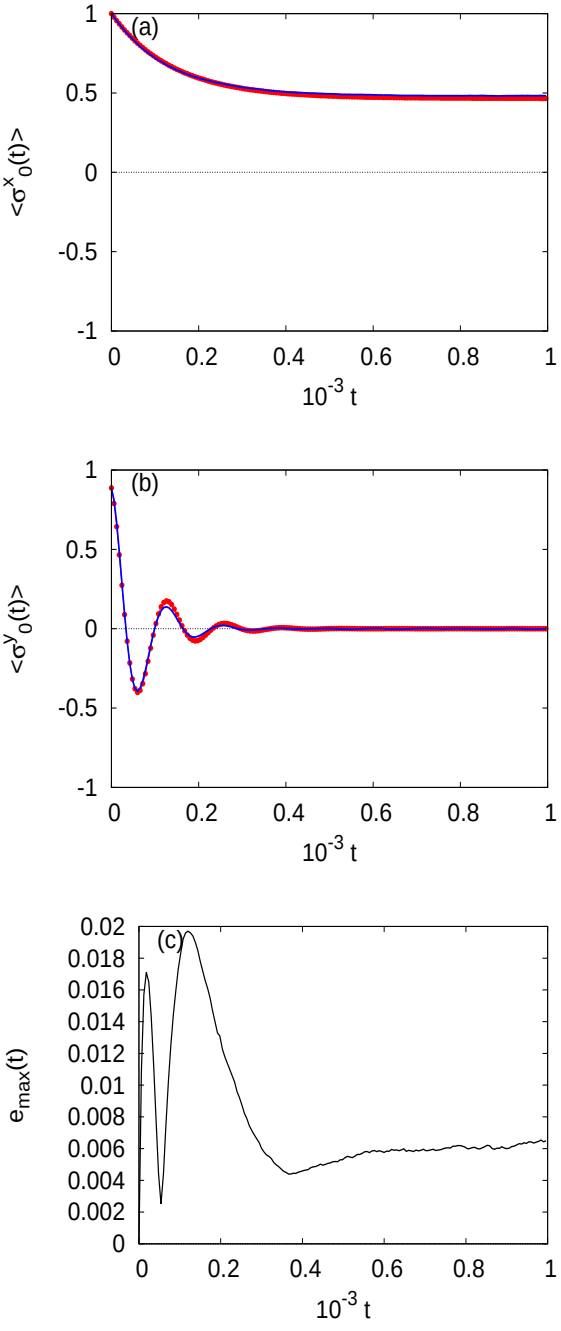

Figure 6.6: (color online) Same as Fig. 6.5, except that the bath is initially at $\beta = 1$.

a QMEQ that does indicate that the system spin relaxes to a state that is close to thermal equilibrium: The QMEQ yields a value of 0.04 for the expectation value of the x-component of the system spin and values less than 10^{-4} for the other two components. From the general theory of the QMEQ in the Markovian approximation [113], we know that if the correlations of the bath-operators Eq. (6.47) satisfy the Kubo-Martin-Schwinger condition, the stationary state solution of the QMEQ is exactly the same as the thermal equilibrium state of the system (ignoring corrections of $\mathcal{O}(\lambda)$ [see Ref. [128] for a detailed discussion)].

The mismatch between the QMEQ and TDSE data of the x-component can be attributed to the fact that a bath of $N_{\mathrm{B}} = 13$ spins is too small to act as a bath in thermal equilibrium. However, the argument that leads to this conclusion is somewhat subtle. As shown in Sec. 6.3.2, the random state approach applied to the system + bath yields the correct thermal equilibrium properties. In particular, in the case at hand ($\beta = 0$, $N_{\mathrm{B}} = 13$), within the usual statistical fluctuations it yields $\langle\Phi(\beta = 0)|\sigma_0^\alpha(t)|\Phi(\beta = 0)\rangle \approx 0$ for $\alpha = x, y, z$. Note that in this kind of calculation, the initial state $|\Phi(\beta = 0)\rangle$ is a random state of the system + bath. In contrast, the data shown in Fig. 6.4(d) are obtained by solving the TDSE with the initial state $|\Psi(0)\rangle_x = |x\rangle|\phi\rangle$ (see Sec. 6.6). Therefore, the results of Fig. 6.4(d) demonstrate that for $N_{\mathrm{B}} = 13$, the statement that

$$|x\rangle|\phi\rangle \longrightarrow \text{TDSE evolution} \longrightarrow |\widetilde{\Phi}\rangle,$$

where $\widetilde{\Phi}$ denotes an (approximate) random state of the whole system, *is not necessarily true*. Otherwise, we would have $\langle\widetilde{\Phi}|\sigma_0^x(t)|\widetilde{\Phi}\rangle \approx 0$ for t large enough, in contradiction with the data shown in Fig. 6.4(d). Roughly speaking, one could say that a bath of $N_{\mathrm{B}} = 13$ is not sufficiently "complex" to let the TDSE evolve certain initial states towards a random state of the whole system. For a discussion of the fact that in general, Eq. (6.54) does not necessarily hold, see Ref. [141].

As a check on this argument, we repeat the simulation with a bath $N_{\mathrm{B}} = 24$ spins. The results are shown in Fig. 6.5. Comparing Figs. 6.4 and 6.5, it is clear that for long times the value of the x-component decreases as the number of spins in the bath increases and that the agreement between the TDSE data and the fitted QMEQ data has improved considerably. This suggests that as the size of the bath increases and with the bath initially in a random state, the TDSE evolution can drive the state to an (approximate) random state of the whole system, meaning that the whole system relaxes to the thermal equilibrium state. However, as discussed in Sec. 6.9 there are exceptions [141].

In general, we may expect that for short times, a Markovian QMEQ cannot represent the TDSE evolution very well [117, 122]. But if we follow the evolution for times much longer than the typical correlation times of the bath-operators, the difference between the QMEQ and TDSE data for short times does not affect the results of

fitting the data over the whole, large time-interval in a significant manner. Hence there is no need to discard the short-time data in the fitting procedure. As a matter of fact, the data shown in Fig. 6.4 indicate that the least-square procedure applied to the whole data set yields a Markovian master equation that reproduces the short-time behavior quite well.

Finally, we check that the conclusions reached so far for a bath at $\beta = 0$ also hold when $\beta > 0$. In Fig. 6.6, we show the simulation results for $\beta = 1$, for the same system and bath as the one used to obtain the data shown in Fig. 6.5. From Fig. 6.6 we conclude that the agreement between the TDSE and QMEQ data is quite good.

Table 6.1: The parameters that appear in Eq. (6.54) as obtained by fitting the QMEQ to the TDSE data shown in Fig. 6.7.

β	i	$A_{i,1}$	$A_{i,2}$	$A_{i,3}$	b_i
0	1	-0.29×10^{-1}	$+0.57 \times 10^{-3}$	-0.11×10^{-2}	-0.31×10^{-3}
0	2	-0.55×10^{-2}	-0.73×10^{-1}	$+1.01$	-0.95×10^{-4}
0	3	-0.73×10^{-3}	-1.01	-0.74×10^{-1}	-0.56×10^{-4}
1	1	-0.40×10^{-1}	$+0.11 \times 10^{-1}$	-0.11×10^{-3}	-0.18×10^{-1}
1	2	-0.11×10^{-1}	-0.36×10^{-1}	$+0.99$	-0.29×10^{-3}
1	3	-0.54×10^{-3}	-0.99	-0.53×10^{-1}	-0.32×10^{-3}
2	1	-0.35×10^{-1}	$+0.29 \times 10^{-1}$	$+0.75 \times 10^{-3}$	-0.27×10^{-1}
2	2	-0.22×10^{-1}	-0.45×10^{-1}	$+0.98$	-0.47×10^{-2}
2	3	-0.84×10^{-3}	-0.98	-0.40×10^{-1}	-0.16×10^{-3}

6.7 Simulation results: $N_{\rm B} = 28, 32$

As already mentioned in Sec. 6.3, in practice, there is a limitation on the sizes and time intervals that can be explored. By increasing the system-bath interaction λ, we can shorten the time needed for the system to relax to equilibrium. On the other hand, λ should not be taken too large because when we leave the perturbative regime, the QMEQ of the form Eq. (6.37) cannot be expected to capture the true quantum dynamics. From our exploratory simulations, we know that $\lambda = 0.1$ is still within the perturbative regime, hence we will adopt this value when solving the TDSE for baths with up to $N_{\rm B} = 32$ spins.

In Fig. 6.7 we present the results as obtained with a bath containing $N_{\rm B} = 28$ spins, prepared at $\beta = 0, 1, 2$. Although Fig. 6.7 may suggest otherwise, the maximum error $\max_k e_{\max}(t) \approx 0.05, 0.1, 0.2$ for $\beta = 0, 1, 2$, respectively, indicating that the difference between the TDSE data and the QMEQ approximation increases with β. The results presented in Fig. 6.8 for a bath of $N_{\rm B} = 32$ spins and $\beta = 1$ provide additional

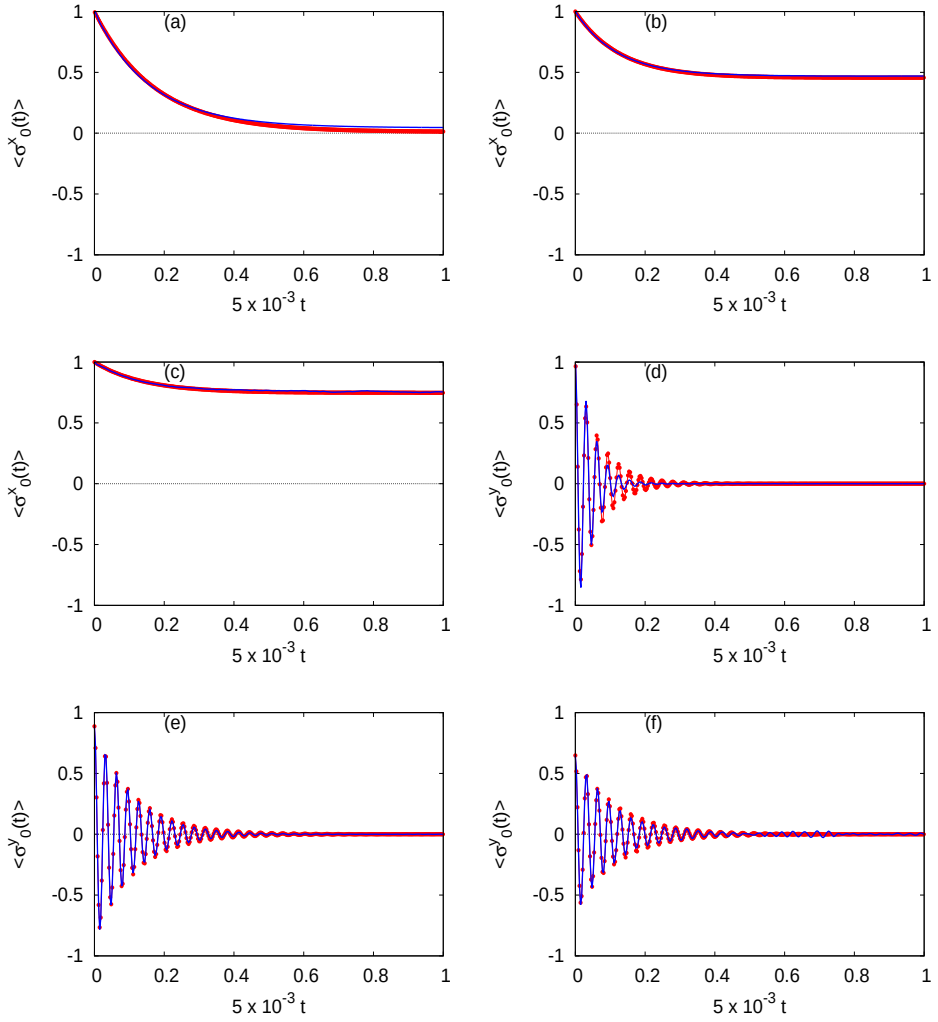

Figure 6.7: (color online) Simulation data for a bath with $N_{\rm B} = 28$ spins and system-bath interaction $\lambda = 0.1$. The model parameters are: $h^x_{\rm B} = h^z_{\rm B} = 1/8$, $K = -1/4$, and $\Delta = 1$. Solid lines: TDSE data; solid circles: QMEQ data. Top row: $\langle\sigma^x(t)\rangle$ as obtained by starting from the initial state $|x\rangle|\phi\rangle$, (a)–(c) corresponding to $\beta = 0, 1, 2$, respectively. Bottom row: $\langle\sigma^y(t)\rangle$ as obtained by starting from the initial state $|y\rangle|\phi\rangle$, (d)–(f) corresponding to $\beta = 0, 1, 2$, respectively. The TDSE simulations yield $\langle|\sigma^x_0(t = 200)|\rangle = 0.044$, $\langle|\sigma^x_0(t = 200)|\rangle = 0.475$, and $\langle|\sigma^x_0(t = 200)|\rangle = 0.756$ for $\beta = 0, 1, 2$, respectively, whereas for the system in equilibrium we have $\langle\sigma^x_0\rangle = 0, 0.462, 0.762$ for $\beta = 0, 1, 2$, respectively. For clarity, the data are shown with a time interval of 0.6. The TDSE solver provided 3000 numbers as input to the least-square procedure.

evidence for the observation that a bath of $N_{\rm B} = 28, 32$ spins are sufficiently large to mimic an infinite thermal bath. At any rate, in all cases, there is very good qualitative agreement between the TDSE and QMEQ data.

From the TDSE data, we can, of course, also extract the values of the entries in the matrix $\mathbf{A}$ and vector $\mathbf{b}$, see Eq. (6.37). Writing Eq. (6.37) more explicitly as

$$\begin{aligned}
\frac{\partial\langle\boldsymbol{\sigma}_0^x(t)\rangle}{\partial t} &= A_{1,1}\langle\boldsymbol{\sigma}_0^x(t)\rangle + A_{1,2}\langle\boldsymbol{\sigma}_0^y(t)\rangle + A_{1,3}\langle\boldsymbol{\sigma}_0^z(t)\rangle + b_1 \\
\frac{\partial\langle\boldsymbol{\sigma}_0^y(t)\rangle}{\partial t} &= A_{2,1}\langle\boldsymbol{\sigma}_0^x(t)\rangle + A_{2,2}\langle\boldsymbol{\sigma}_0^y(t)\rangle + A_{2,3}\langle\boldsymbol{\sigma}_0^z(t)\rangle + b_2 \\
\frac{\partial\langle\boldsymbol{\sigma}_0^z(t)\rangle}{\partial t} &= A_{3,1}\langle\boldsymbol{\sigma}_0^x(t)\rangle + A_{3,2}\langle\boldsymbol{\sigma}_0^y(t)\rangle + A_{3,3}\langle\boldsymbol{\sigma}_0^z(t)\rangle + b_3, \qquad (6.54)
\end{aligned}$$

and using, as an example, the data shown in Fig. 6.7, we obtain the values of the coefficients as given in Table 6.1. From Table 6.1, we readily recognize that (i) $A_{2,3} \approx -A_{3,2} \approx 1$ represents the precession of the system spin in the magnetic field $h^x = 1/2$, (ii) there is a weak coupling between the x- and (y, z)- components of the system spin and (iii) the three spin components have different relaxations times.

As a final check whether $\lambda = 0.1$ is well within the perturbative regime, we repeat the simulations for a bath containing $N_{\rm B} = 32$ spins and system-bath interaction $\lambda = 0.2$ and $\beta = 0$. The simulation data are presented in Fig. 6.9. Clearly, there still is good qualitative agreement between the TDSE and QMEQ data but, as expected, $\max_k e_{\max}(t)$ has become larger (by a factor of about 3).

In Table 6.2 we present results (first three rows) for the least-square estimates of the parameters that enter the QMEQ, as obtained from the TDSE data shown in Fig. 6.8. Taking into account that with each run, the random values of the model parameters change, the order-of-magnitude agreement between the data for $N_{\rm B} = 28$ (Table 6.1, rows 4–6) and the $N_{\rm B} = 32$ data is rather good. We also present results (middle and last three rows) for the parameters that enter the Redfield equation Eq. (6.46), as obtained from the TDSE data of the bath-operator correlations $C(i, j, t)$ for $0 \leq t \leq 40$ [see Figs. 6.2(a) and 6.2(c) for a picture of some of these data]. From Table 6.2, it is clear that there seems to be little quantitative agreement between a description based on the Redfield quantum master equation (6.46) obtained by using the bath-operator correlations $C(i, j, t)$ data and the parameters obtained from the least-square fit of Eq. (6.54) to the TDSE data. Simulations using the 3D bath Hamiltonian (6.7) support this conclusion (see Appendix B).

Although our results clearly demonstrate that QMEQ Eq. (6.37) quantitatively describes the true quantum dynamics of a spin interacting with a spin bath rather well, the Redfield quantum master equation Eq. (6.46) in the Markovian approximation, which is also of the form Eq. (6.37), seems to perform rather poorly in comparison. The estimates of the diagonal matrix elements of the matrix $\mathbf{A}$ as obtained from the expressions in terms of the bath-operator correlations $C(i, j, t)$ are too small by factors

Table 6.2: First three data rows: coefficients that appear in Eq. (6.54) as obtained by fitting the QMEQ to the TDSE data shown in Fig. 6.8. Middle three rows: the corresponding coefficients as obtained by numerically calculating the parameters r_{jk} that appear in the Redfield quantum master equation Eq. (6.46) according to Eq. (6.45), using the TDSE data of the bath-operator correlations shown in Fig. 6.2(a). Last three rows: same as the middle three rows except that the used TDSE data of the bath-operator correlations are shown in Fig. 6.2(c). Note that the baths used in these simulations are very different (see Fig. 6.2), yet the relevant numbers (those with absolute value larger than 10^{-4}) are in the same ballpark.

i	$A_{i,1}$	$A_{i,2}$	$A_{i,3}$	b_i
1	-0.49×10^{-1}	$+0.82\times10^{-2}$	-0.56×10^{-3}	-0.19×10^{-1}
2	-0.80×10^{-2}	-0.42×10^{-1}	$+1.02$	-0.14×10^{-4}
3	-0.38×10^{-3}	-1.01	-0.41×10^{-1}	-0.40×10^{-3}
1	-0.71×10^{-2}	-0.15×10^{-3}	$+0.18\times10^{-3}$	-0.29×10^{-2}
2	-0.13×10^{-3}	-0.15×10^{-1}	$+1.00$	-0.63×10^{-4}
3	$+0.16\times10^{-3}$	-1.00	-0.15×10^{-1}	$+0.75\times10^{-4}$
1	-0.64×10^{-2}	$+0.16\times10^{-3}$	$+0.14\times10^{-3}$	-0.26×10^{-2}
2	$+0.75\times10^{-3}$	-0.14×10^{-1}	$+1.00$	$+0.64\times10^{-4}$
3	-0.16×10^{-3}	-1.00	-0.15×10^{-1}	$+0.64\times10^{-4}$

3–7. This suggests that the approximations involved in the derivation of Eq. (6.46) are not merely of a perturbative nature but affect the dynamics in a more intricate manner [see Ref. [127] for an in-depth discussion of these aspects].

6.8 Exceptions

The simulation results presented in Secs. 6.6 and 6.7 strongly suggest that, disregarding some minor quantitative differences, the complicated Schrödinger dynamics of the system interacting with the bath can be modeled by the much simpler QMEQ of the form (6.37). But, as mentioned in Sec. 6.4, there are several approximations involved to justify the reduction of the Schrödinger dynamics to a QMEQ. In this section, we consider a few examples for which this reduction may fail.

The first case that we consider is defined by the Hamiltonian

$$H = -h^x\sigma_0^x + \frac{\lambda}{4}\sum_{n=1}^{N_\mathrm{B}}\left(\sigma_n^x\sigma_0^x + \sigma_n^y\sigma_0^y + \sigma_n^z\sigma_0^z\right) + \frac{1}{4}\sum_{n=1}^{N_\mathrm{B}}\left(\sigma_n^x\sigma_{n+1}^x + \sigma_n^y\sigma_{n+1}^y + \sigma_n^z\sigma_{n+1}^z\right). \tag{6.55}$$

In other words, both the system-bath and intra-bath interactions are of the isotropic

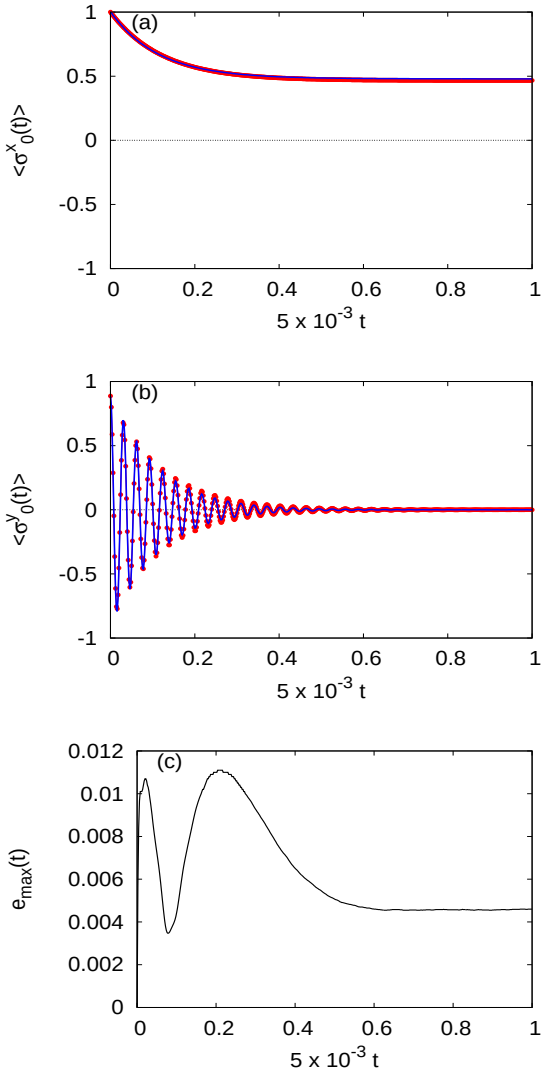

Figure 6.8: (color online) Simulation data for a bath with $N_{\rm B} = 32$ spins prepared at $\beta = 1$ and system-bath interaction $\lambda = 0.1$. The model parameters are: $h_{\rm B}^x = h_{\rm B}^z = 1/8$, $K = -1/4$, and $\Delta = 1$. Figures (a,b) show TDSE data (solid lines) and QMEQ data (solid circles). (a) initial state $|x\rangle|\phi\rangle$; (b) initial state $|y\rangle|\phi\rangle$; (c) the error $e_{\rm max}(t)$. The data obtained with the initial state $|\uparrow\rangle|\phi\rangle$ is very similar as the data obtained with the initial state $|y\rangle|\phi\rangle$ and are therefore not shown. For clarity, the data are shown with a time interval of 0.4. The TDSE solver provided 3000 numbers as input to the least-square procedure.

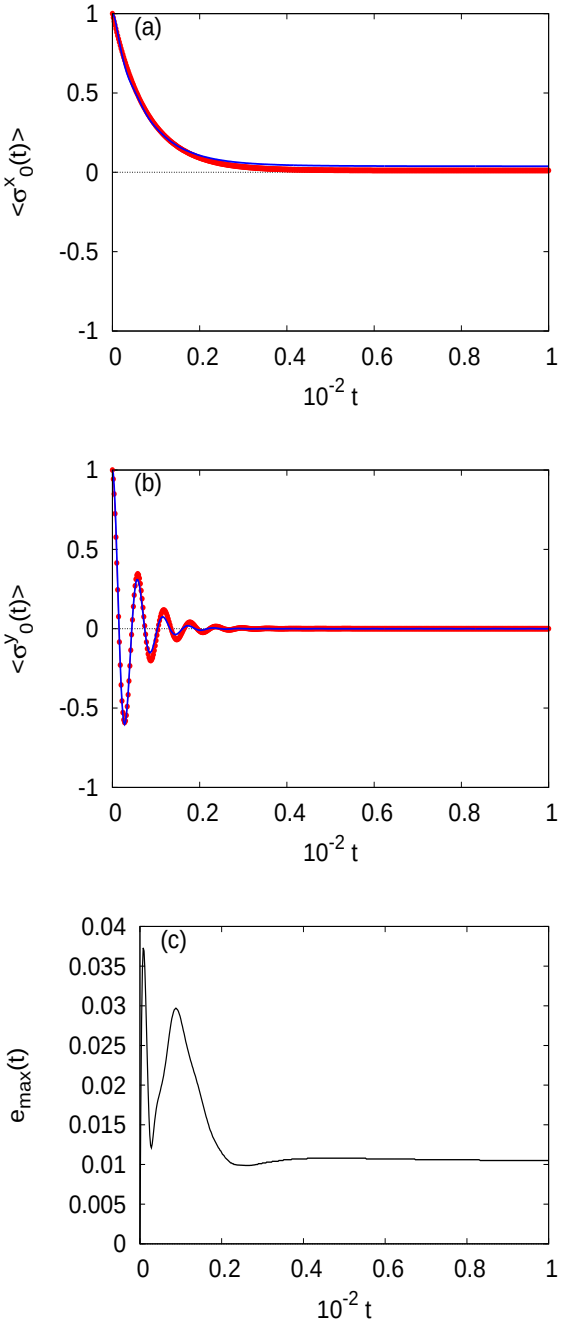

Figure 6.9: (color online) Same as Fig. 6.8 except that $\beta = 0$ and $\lambda = 0.2$.

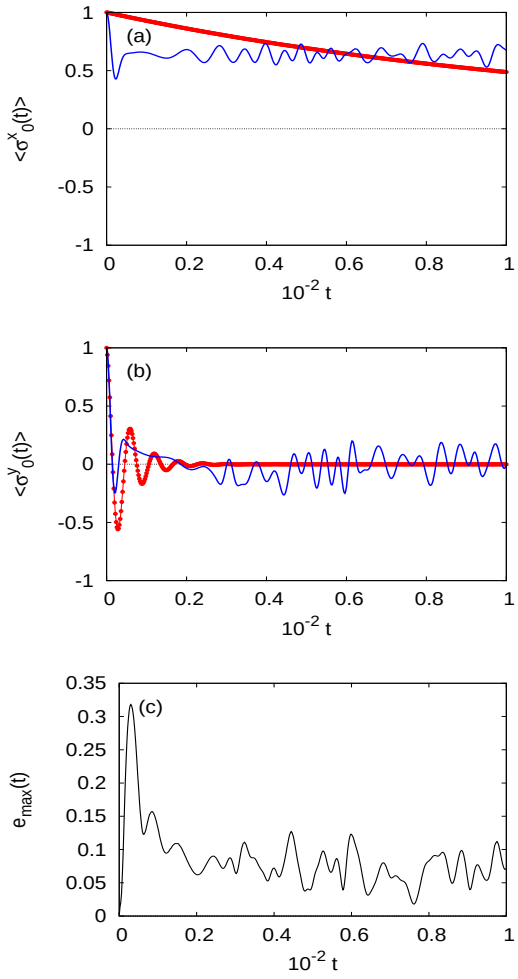

Figure 6.10: (color online) Simulation data for a bath with $N_{\rm B} = 32$ spins prepared at $\beta = 0$ and system-bath interaction $\lambda = 0.2$. The system Hamiltonian is given by Eq. (6.2). The system-bath interaction is given by Eq. (6.3) with $J_n^x = J_n^y = J_n^z = 1/4$. The bath Hamiltonian is given by Eq. (6.5) with $K = -1/4$, $\Delta = 1$ and $h_n^x = h_n^z = 0$. The full Hamiltonian is given by Eq. (6.55). Figures (a,b) show TDSE data (solid lines) and QMEQ data (solid circles). (a) initial state $|x\rangle|\phi\rangle$; (b) initial state $|y\rangle|\phi\rangle$; (c) the error $e_{\rm max}(t)$. The data obtained with the initial state $|\uparrow\rangle|\phi\rangle$ is very similar as the data obtained with the initial state $|y\rangle|\phi\rangle$ and are therefore not shown. With this choice of parameters of bath and system-bath Hamiltonians, the system does not relax to its thermal equilibrium state $\lim_{t\to\infty}\langle\sigma_0^x(t)\rangle = \lim_{t\to\infty}\langle\sigma_0^y(t)\rangle = \lim_{t\to\infty}\langle\sigma_0^z(t)\rangle = 0$. For clarity, the data is shown with a time interval of 0.4. The TDSE solver provided 3000 numbers as input to the least-square procedure.

antiferromagnetic Heisenberg type and all interaction strengths are constant. The simulation results for this case are presented in Fig. 6.10. From Fig. 6.10(a), it is immediately clear that the system does not relax to its thermal equilibrium state at $\beta = 0$ (for which $\lim_{t\to\infty}\langle\sigma_0^x(t)\rangle = 0$). Apparently, the bath Hamiltonian is too "regular" to drive the system to its thermal equilibrium state, hence it is also not surprising that the attempt to let the QMEQ describe the Schrödinger dynamics fails.

The second case that we consider is defined by the Hamiltonian

$$H = -h^x\sigma_0^x + \frac{\lambda}{4}\sum_{n=1}^{N_\mathrm{B}} J_n^z\sigma_n^z\sigma_0^z + \frac{1}{4}\sum_{n=1}^{N_\mathrm{B}}\sigma_n^z\sigma_{n+1}^z, \tag{6.56}$$

with system-bath interactions J_n^z chosen at random and distributed uniformly over the interval $[-1,1]$ and the bath is modeled by an Ising Hamiltonian. The model Eq. (6.56) is known to exhibit quantum oscillations in the absence of quantum coherence [150]. As the bath Hamiltonian commutes with all other terms of the Hamiltonian, the only non-zero bath correlation $C(3,3,t)$ is constant in time, hence one of the basic assumptions in deriving the QMEQ Eq. (6.37) does not hold.

Because of the special structure of the Hamiltonian Eq. (6.56) it is straightforward to compute closed form expressions for the expectation values of the system spin. For $\beta = 0$ we find

$$z\langle\sigma_0^x(t)\rangle = 1 - 2\lambda^2\left\langle\left\langle\frac{\mathcal{B}^2\sin^2 t\sqrt{(h^x)^2+\mathcal{B}^2}}{(h^x)^2+\mathcal{B}^2}\right\rangle\right\rangle, \quad |\Psi(t=0)\rangle = |x\rangle|\phi\rangle, \tag{6.57}$$

$$\langle\sigma_0^y(t)\rangle = \left\langle\left\langle\cos 2t\sqrt{(h^x)^2+\mathcal{B}^2}\right\rangle\right\rangle, \qquad |\Psi(t=0)\rangle = |y\rangle|\phi\rangle, \tag{6.58}$$

$$\langle\sigma_0^z(t)\rangle = 1 - 2\lambda^2(h^x)^2\left\langle\left\langle\frac{\sin^2 t\sqrt{(h^x)^2+\mathcal{B}^2}}{(h^x)^2+\mathcal{B}^2}\right\rangle\right\rangle, \quad |\Psi(t=0)\rangle = |\uparrow\rangle|\phi\rangle, \tag{6.59}$$

where $\mathcal{B} = \mathcal{B}(\{s_n\}) = \sum_{n=1}^{N_\mathrm{B}} J_n^z s_n$ and

$$\langle\langle\mathcal{X}\rangle\rangle \equiv \sum_{\{s_1=\pm1\}}\cdots\sum_{\{s_{N_\mathrm{B}}=\pm1\}}|\langle s_1\ldots s_{N_\mathrm{B}}|\phi\rangle|^2\mathcal{X}(\{s_n\}), \tag{6.60}$$

denotes the average over all the bath-spin configurations.

From Eq. (6.57) it follows immediately that if the system+bath is initially in the state $|\Psi(t=0)\rangle = |x\rangle|\phi\rangle$, we must have $\langle\sigma_0^x(t)\rangle \geq 1-2\lambda^2$. Hence the system will never relax to its thermal equilibrium state [for which $\lim_{t\to\infty}\langle\sigma_0^x(t)\rangle = 0$]. Nevertheless, from Fig. 6.11 it may still seem that the QMEQ captures the essential features of the Schrödinger dynamics but the qualitative agreement is a little misleading. More insight into this aspect can be obtained by considering the limit of a very larger number of bath spins N_B, by assuming $|\phi\rangle$ to be a uniform superposition of the 2^{N_B}

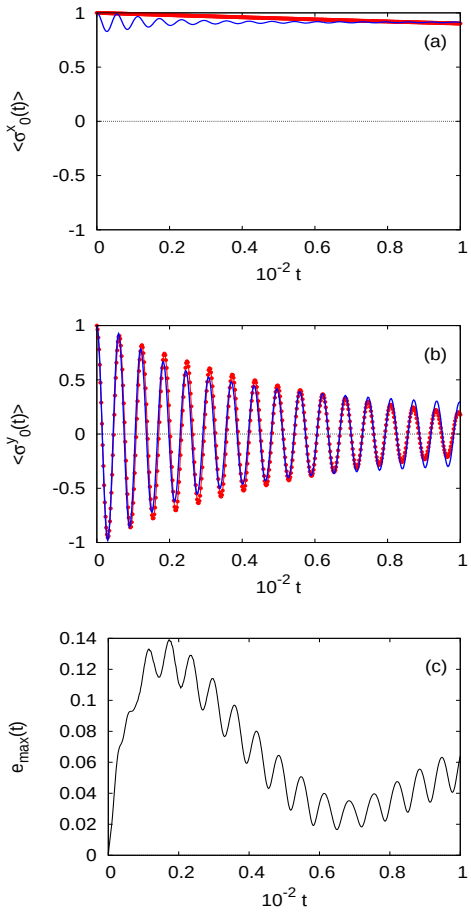

Figure 6.11: (color online) Simulation data for a bath with $N_{\rm B} = 32$ spins prepared at $\beta = 0$ and system-bath interaction $\lambda = 0.2$. The system Hamiltonian is given by Eq. (6.2). The system-bath interaction is given by Eq. (6.3) with $J_n^x = J_n^y = 0$ and J_n^z uniformly random between $-1/4$ and $1/4$, in which case the interaction of the system and bath spins is through the coupling of the z-components of the spins only. The bath Hamiltonian is given by Eq. (6.6) with $K_n^x = K_n^y = h_n^x = h_n^z = 0$ and K_n^z uniformly random between -1 and 1. The full Hamiltonian is given by Eq. (6.56). (a),(b) Show TDSE data (solid lines) and QMEQ data (solid circles). (a) initial state $|x\rangle|\phi\rangle$; (b) initial state $|y\rangle|\phi\rangle$; (c) the error $e_{\max}(t)$. The data obtained with the initial state $|\uparrow\rangle|\phi\rangle$ are very similar as the data obtained with the initial state $|y\rangle|\phi\rangle$ and are therefore not shown. With this choice of bath and system-bath Hamiltonians, the system does not relax to its thermal equilibrium state $\lim_{t\to\infty}\langle\sigma_0^x(t)\rangle = \lim_{t\to\infty}\langle\sigma_0^y(t)\rangle = \lim_{t\to\infty}\langle\sigma_0^z(t)\rangle = 0$. For clarity, the data are shown with a time interval of 0.4. The TDSE solver provided 3000 numbers as input to the least-square procedure.

different bath states and by approximating $\mathcal{B}$, being a sum of independent uniform random variables, by a Gaussian random variable. Then we have (after substituting $\mathcal{B} = h^x u$)

$$\langle \sigma^y(t) \rangle = \frac{1}{\sigma\sqrt{2\pi}} \int_{-\infty}^{+\infty} du\, e^{-u^2\theta/2\sigma^2} \cos\left(2th^x\sqrt{1+u^2}\right). \tag{6.61}$$

For large t, we can evaluate Eq. (6.61) by the stationary phase method and we find that $\langle \sigma^y(t) \rangle$ decays as $1/\sqrt{t}$. Such a slow algebraic decay cannot result from a time evolution described by a single matrix exponential $e^{t\mathbf{A}}$. In other words, the apparent agreement shown in Fig. (6.11) is due to the relatively short time interval covered. On the other hand, as already mentioned, the model defined by Eq. (6.56) is rather exceptional in the sense that the bath correlations do not exhibit any dynamics. Hence it is not a surprise that the QMEQ cannot capture the $1/\sqrt{t}$ dependence.

Finally, in Fig. 6.12 we illustrate what happens if the $\lambda = 1$, that is if the system-bath interaction becomes comparable to the other energy scales h^x and K. Then, the perturbation expansion that is used to derive the QMEQ of the form Eq. (6.37) is no longer expected to hold [113]. The data presented in Fig. 6.12 clearly show that even though the time it takes for the system to reach the stationary state is rather short (because $\lambda = 1$), the QMEQ fails to capture, even qualitatively, the dynamic behavior of the system. Note that the Schrödinger dynamics drives the system to a stationary state which is far from the thermal equilibrium state of the isolated system. The TDSE solution yields $\langle \sigma_0^x(t = 100) \rangle = 0.264$ [$|\langle \sigma_0^z(t = 100) \rangle| \leq 10^{-2}$ $|\langle \sigma_0^z(t = 100) \rangle| \leq 10^{-2}$], whereas from statistical mechanics for the isolated system at $\beta = 1$ we expect $\langle \sigma_0^x \rangle = \tanh(1/2) = 0.462$ [$\langle \sigma_0^y(t = 100) \rangle = \langle \sigma_0^z(t = 100) \rangle = 0$], a significant difference which, in view of the strong system-bath interaction, is not entirely unexpected.

6.9 Discussion and Conclusion

We have addressed the question to what extent a quantum master equation of the form (6.37) captures the salient features of the exact Schrödinger equation dynamics of a single spin coupled to a bath of spins. The approach taken was to solve the time-dependent Schrödinger equation of the whole system and fit the data of the expectation values of the spin components to those of a quantum master equation of the form (6.37).

In all cases in which the approximations used to derive a quantum master equation of the form (6.37) seem justified, it was found that the quantum master equation (6.37) extracted from the solutions of the time-dependent Schrödinger equation describes these solutions rather well. The least-square procedure that is used to fit the quantum master equation (6.37) data to the time-dependent Schrödinger data accounts for non-

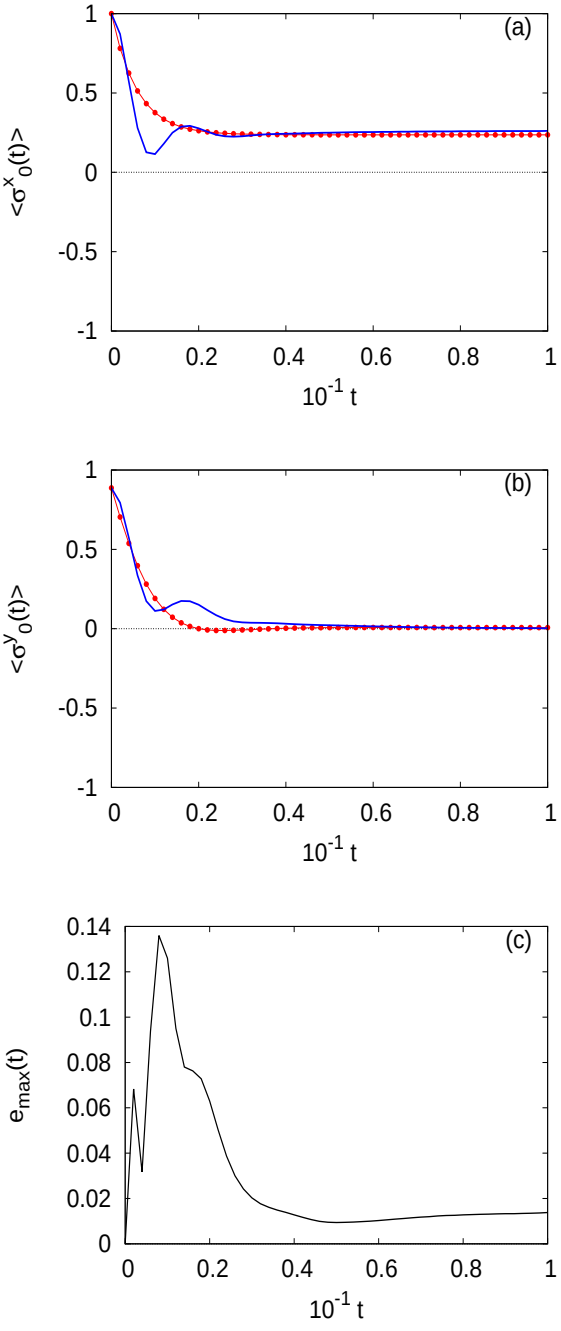

Figure 6.12: (color online) Same as Fig. 6.8 except that $\beta = 1$ and $\lambda = 1$.

Markovian effects and nonperturbative contributions. Quantitatively, we found that differences between the data produced by the quantum master equation, obtained by least-square fitting to the time-dependent Schrödinger data, and the latter data increases with decreasing temperature.

The main finding of this work is that the exact Schrödinger dynamics of a single spin-1/2 object interacting with a spin-1/2 bath can be accurately and effectively described by Eq. (6.37) which, for convenience of the reader, is repeated here and reads as

$$\frac{\partial \boldsymbol{\rho}(t)}{\partial t} = \mathbf{A}\boldsymbol{\rho}(t) + \mathbf{b}, \tag{6.62}$$

where the 3×3 matrix $\mathbf{A}$ and the three elements of the vector $\mathbf{b}$ are time independent. As the mathematical structure of the (Markovian) quantum master equation (6.62) is the same as that of the Bloch equation (A.1), as a phenomenological description, the quantum master equation (6.62) offers no advantages over the latter. Of course, when the system contains more than one spin, the Bloch equation can no longer be used whereas the quantum master equation (6.62) still has the potential to describe the dynamics. We relegate the assessment of the quantum master equation approach to systems of two or more spins to a future research project.

Appendices

Appendix A

Bloch equations

Whatever method we use to extract $e^{\tau \mathbf{A}}$ and $\mathbf{B}$, it is necessary to validate the method by applying it to a non-trivial problem for which we know the answer for sure. The Bloch equations, originally introduced by Felix Bloch [151] as phenomenological equations to describe the equations of motion of nuclear magnetization, provide an excellent test bed for the extraction algorithm presented in Sec. 6.5.

In matrix notation the Bloch equations read as

$$\frac{d\mathbf{M}(t)}{dt} = \widehat{\mathbf{A}}\mathbf{M}(t) + \widehat{\mathbf{b}}, \tag{A.1}$$

where $\mathbf{M}$ is the magnetization,

$$\widehat{\mathbf{A}} = \begin{pmatrix} -1/T_2 & h_z & -h_y \\ -h_z & -1/T_2 & h_x \\ h_y & -h_x & -1/T_1 \end{pmatrix}, \tag{A.2}$$

and $\widehat{\mathbf{b}} = \mathbf{M}_0/T_1$ where $\mathbf{M}_0$ is the steady state magnetization. The transverse and longitudinal relaxation times T_2 and T_1 are strictly larger than zero. The special but interesting case in which there is no relaxation corresponds to $1/T_1 = 1/T_2 = 0$,

Obviously Eq. (A.1) has the same form as Eq. (6.37). Hence we can use Eq. (A.1) to generate the data $\boldsymbol{\rho(t)} = \mathbf{M}(t)$ that is needed to test the algorithm described in Sec. 6.5. In order that the identification $\boldsymbol{\rho(t)} = \mathbf{M}(t)$ makes sense in the context of the quantum master equation we have to impose the trivial condition that $\|\mathbf{M}(t=0)\| \leq 1$ and $\|\mathbf{M}_0\| \leq 1$.

We generate the test data by integrating Eq. (A.1). In practice, we compute $e^{\tau \widehat{\mathbf{A}}}$ using the second-order product-formula [152]

$$e^{\tau \widehat{\mathbf{A}}} \approx e^{\tau \widetilde{\mathbf{A}}} = \left(e^{\tau \mathbf{A}_1/2m} e^{\tau \mathbf{A}_2/m} e^{\tau \mathbf{A}_1/2m} \right)^m, \tag{A.3}$$

where $\widehat{\mathbf{A}} = \mathbf{A}_1 + \mathbf{A}_2$ and

$$\mathbf{A}_1 = \begin{pmatrix} -1/T_2 & 0 & 0 \\ 0 & -1/T_2 & 0 \\ 0 & 0 & -1/T_1 \end{pmatrix}, \tag{A.4}$$

$$\mathbf{A}_2 = \begin{pmatrix} 0 & h_z & -h_y \\ -h_z & 0 & h_x \\ h_y & -h_x & 0 \end{pmatrix}. \tag{A.5}$$

The second-order product-formula approximation satisfies the bound $\|e^{\tau\widehat{\mathbf{A}}} - e^{\tau\widetilde{\mathbf{A}}}\| \leq c_2\tau^3/m^2$ where the constant $c_2 = \mathcal{O}(\|[A_1, A_2]\|)$. Hence the error incurred by the approximation is known and can be reduced systematically by increasing m.

It is straightforward to compute the closed form expressions of the matrix exponentials that appear in the second-order product-formula. We have

$$e^{\tau\mathbf{A}_1} = \begin{pmatrix} e^{-\tau/T_2} & 0 & 0 \\ 0 & e^{-\tau/T_2} & 0 \\ 0 & 0 & e^{-\tau/T_1} \end{pmatrix} \tag{A.6}$$

$$e^{\tau\mathbf{A}_2} = \frac{1}{\Omega^2}\begin{pmatrix} E_{11} & E_{12} & E_{13} \\ E_{21} & E_{22} & E_{23} \\ E_{31} & E_{32} & E_{33} \end{pmatrix}, \tag{A.7}$$

with

$$\begin{aligned}
E_{11} &= h_x^2 + (h_y^2 + h_z^2)\cos\tau\Omega \\
E_{12} &= h_x h_y(1 - \cos\tau\Omega) + h_z\Omega\sin\tau\Omega \\
E_{13} &= h_x h_z(1 - \cos\tau\Omega) - h_y\Omega\sin\tau\Omega \\
E_{21} &= h_x h_y(1 - \cos\tau\Omega) - h_z\Omega\sin\tau\Omega \\
E_{22} &= h_y^2 + (h_x^2 + h_z^2)\cos\tau\Omega \\
E_{23} &= h_y h_z(1 - \cos\tau\Omega) + h_x\Omega\sin\tau\Omega \\
E_{31} &= h_x h_z(1 - \cos\tau\Omega) + h_y\Omega\sin\tau\Omega \\
E_{32} &= h_y h_z(1 - \cos\tau\Omega) - h_x\Omega\sin\tau\Omega \\
E_{33} &= h_z^2 + (h_x^2 + h_y^2)\cos\tau\Omega
\end{aligned} \tag{A.8}$$

where $\Omega^2 = h_x^2 + h_y^2 + h_z^2$.

Summarizing, the numerical solution of the Bloch equations Eq. (A.1) is given by

$$\boldsymbol{\rho}(t+\tau) = e^{\tau\widetilde{\mathbf{A}}}\boldsymbol{\rho}(t) + \widetilde{\mathbf{B}}, \tag{A.9}$$

where $\boldsymbol{\rho}(t) = \mathbf{M}(t)$ and the trapezium rule was used to write

$$\widehat{\mathbf{B}} = \int_0^\tau e^{(\tau-u)\widehat{\mathbf{A}}}\widehat{\mathbf{b}}\,du \approx \frac{\tau}{2}\left(1 + e^{\tau\widetilde{\mathbf{A}}}\right)\widehat{\mathbf{b}} = \widetilde{\mathbf{B}}. \tag{A.10}$$

The approximate solution obtained from Eqs. (A.9) and (A.10) will converge to the solution of Eq. (A.1) as $\tau \to 0$. Clearly, Eq. (A.9) has the same structure as Eq. (6.39) and hence we can use the solution of the Bloch equations as input data for testing the extraction algorithm. Note that the extraction algorithm is expected to yield $e^{\tau\widetilde{\mathbf{A}}}$ and $\widetilde{\mathbf{B}}$, not $e^{\tau\widehat{\mathbf{A}}}$ and $\widehat{\mathbf{B}}$.

A.1 Validation procedure

We use the Bloch equation model to generate the data set $\mathcal{D} = \{\boldsymbol{\rho}(k\tau)|\ 0 \leq k \leq N-1\}$. The validation procedure consists of the following steps:

1. Choose the model parameters h_x, h_y, h_z, $1/T_1$, $1/T_2$ and the steady-state magnetization $\mathbf{M}_0$.
2. Choose τ and m.
3. For each of the three initial states $\rho^{(1)}(0) = (1,0,0)^T$, $\rho^{(2)}(0) = (0,1,0)^T$, and $\rho^{(3)}(0) = (0,0,1)^T$ repeat the operation

$$\rho^{(j)}((k+1)\tau) \leftarrow e^{\tau\widetilde{\mathbf{A}}}\rho^{(j)}(k\tau) + \widetilde{\mathbf{B}} \quad , \quad k = 0, \ldots, N-1 \quad , \quad j = 1,2,3,$$

   and store these data.
4. Use the data $\{\rho^{(j)}(k\tau)\}$ to construct the matrices $3 \times 3N$ matrix $\mathbf{Z} = (\mathbf{Z}^{(1)}\,\mathbf{Z}^{(2)}\,\mathbf{Z}^{(3)})$ and the $4 \times 3N$ matrix $\mathbf{X} = (\mathbf{X}^{(1)}\,\mathbf{X}^{(2)}\,\mathbf{X}^{(3)})$. Then use the singular value decomposition of $\mathbf{X}$ to compute the matrix $\mathbf{Y}$ according to Eq. (6.50) and extract the matrix $e^{\tau\mathbf{A}}$ and vector $\mathbf{B}$ from it, see Eq. (6.48). If one or more of the singular values are zero, the extraction failed.
5. Compute the relative errors

$$e_{\mathrm{A}} = \|e^{\tau\widetilde{\mathbf{A}}} - e^{\tau\widehat{\mathbf{A}}}\|/\|e^{\tau\widehat{\mathbf{A}}}\|, \tag{A.11}$$

$$e_{\mathrm{B}} = \|\widetilde{\mathbf{B}} - \widehat{\mathbf{B}}\|/\|\widehat{\mathbf{B}}\|, \tag{A.12}$$

$$e_{\boldsymbol{\rho}} = \max_k \|\boldsymbol{\rho}((k+1)\tau) - e^{\tau\widetilde{\mathbf{A}}}\boldsymbol{\rho}(k\tau) - \widetilde{\mathbf{B}}\|/\|\boldsymbol{\rho}(k\tau)\|. \tag{A.13}$$

A necessary condition for the algorithm to yield reliable results is that the errors e_{A} and e_{B} are small, of the order of 10^{-10}. Indeed, if one or more of the singular values are zero and the extraction has failed, $e_{\boldsymbol{\rho}}$ may be (very) small but e_{A} or e_{B} is not.

In the case that is of interest to us, the case in which the whole system evolves according to the TDSE, we do not know $e^{\tau\mathbf{A}}$ nor $\mathbf{B}$ and a small value of $e_{\boldsymbol{\rho}}$ is, by itself, no guarantee that the extraction process worked properly. Hence, it also is important to check that all singular values are nonzero.

A.2 Numerical results

In Table A.1 we present some representative results for the errors incurred by the extraction process. In all cases, the relative errors on the estimate of the time evolution operator and the constant term are for the present purpose, rather small. Therefore, the algorithm to extract the time evolution operator $e^{\tau\widetilde{\mathbf{A}}}$ and constant term $\widetilde{\mathbf{B}}$ appearing in the time evolution equation Eq. (6.39) from the data obtained by solving the TDSE yields accurate results when the data are taken from the solution of the Bloch equations. No exceptions have been found yet.

Table A.1: The errors $e_{\mathbf{A}}$, $e_{\mathbf{B}}$, and $e_{\boldsymbol{\rho}}$ as obtained fitting the matrix $e^{\tau\mathbf{A}}$ and the constant term $\mathbf{B}$, to the data of the numerical solution of the Bloch equation with three different initial conditions (see text). The Bloch equations are solved for $N = 500$ steps with the time step τ. The value of the vector $\mathbf{M}_0 = (0, 0, 0.4)^T$. The data of the whole time interval $[0, N-1]$ were used for the least-square fitting procedure. The column labeled $\Sigma_i \neq 0$ indicates whether all singular values are nonzero or not. For the meaning of all other symbols, see text.

h_x	h_y	h_z	$1/T_1$	$1/T_2$	τ	$\Sigma_i \neq 0$	$e_{\mathbf{A}} < 10^{-10}$	$e_{\mathbf{B}} < 10^{-10}$	$e_{\boldsymbol{\rho}} < 10^{-10}$
0.5	1.5	0.7	0.05	0.3	0.1	✓	✓	✓	✓
0.5	1.5	0.7	0	0	0.1	✓	✓	✓	✓
0.5	1.5	0.7	0.01	0	1.0	✓	✓	✓	✓
0	0	1	0	0	1.0	✓	✓	✓	✓

Appendix B

Simulation results using the 3D bath Hamiltonian

In this appendix, we present some additional results in support of the conclusions drawn from the simulations of using the 1D bath Hamiltonians (6.5) and (6.6).

Table B.1 summarizes the results of the analysis of TDSE data, as obtained with the 3D bath Hamiltonian Eq. (6.7) with random intra-bath couplings and random h-fields for the bath spins. The model parameters that were used to compute the TDSE data are the same as those that yield the results for the 1D bath presented in Table 6.2. Comparing the first three rows (the parameters that appear in the Markovian master equation (6.54) with the corresponding last three rows (the parameters r_{jk} that appear in the Redfield quantum master equation Eq. (6.46)), we conclude that changing the connectivity of the bath does not significantly improve (compared to the data shown in Table 6.1) the quantitative agreement between the data in the two sets of three rows.

In Table B.2, we show the effect of increasing the energy scale of the bath spins by a factor of 10, reducing the relaxation times of the bath-correlations by a factor of 10, i.e., closer to the regime of the Markovian limit in which Eq. (6.46) has been derived. The differences between the QMEQ estimates (first three rows) and the Redfield equation estimates (second three rows) values of $A_{2,2}$ and $A_{3,3}$ are significantly smaller than in those for the case shows in e.g. Table B.1 but the $A_{1,1}$ elements differ by a factor of four and the $A(2,1)$ elements differ even much more. Although the results presented in Tables B.1 and B.2 indicate that the data extracted from the TDSE through Eq. (6.54) and those obtained by calculating the parameters r_{jk} that appear in the Redfield quantum master equation Eq. (6.46) in the Markovian limit will converge to each other, it becomes computationally very expensive to approach

Table B.1: First three data rows: coefficients that appear in Eq. (6.54) as obtained by fitting the QMEQ Eq. (6.37) to the TDSE data for $h^x = 1/2$, $\lambda = 0.1$, $N_\mathrm{B} = 27$, the 3D bath Hamiltonian Eq. (6.7) with random couplings ($K = 1/4$) and random h-fields ($h^x_\mathrm{B} = h^z_\mathrm{B} = 1/4$). Last three rows: the corresponding coefficients as obtained by numerically calculating the parameters r_{jk} that appear in the Redfield quantum master equation Eq. (6.46) according to Eq. (6.45) from the TDSE data of the bath-operator correlations.

i	$A_{i,1}$	$A_{i,2}$	$A_{i,3}$	b_i
1	-0.25×10^{-1}	-0.82×10^{-2}	$+0.67 \times 10^{-3}$	-0.11×10^{-1}
2	$+0.11 \times 10^{-1}$	-0.47×10^{-1}	$+0.99$	$+0.91 \times 10^{-4}$
3	$+0.16 \times 10^{-3}$	-1.00	-0.47×10^{-1}	$+0.51 \times 10^{-3}$
1	-0.49×10^{-2}	$+0.49 \times 10^{-5}$	-0.80×10^{-4}	-0.20×10^{-2}
2	$+0.15 \times 10^{-3}$	-0.19×10^{-1}	$+1.00 \times 10^{+0}$	$+0.59 \times 10^{-5}$
3	$+0.53 \times 10^{-2}$	$-0.99 \times 10^{+0}$	-0.19×10^{-1}	-0.50×10^{-4}

Table B.2: The same as Table B.1 except that the random couplings ($K = 10/4$) and random h-fields ($h^x_\mathrm{B} = h^z_\mathrm{B} = 10/4$).

i	$A_{i,1}$	$A_{i,2}$	$A_{i,3}$	b_i
1	-0.77×10^{-2}	$+0.20 \times 10^{-1}$	-0.77×10^{-4}	-0.37×10^{-3}
2	-0.19×10^{-1}	-0.99×10^{-2}	$+0.99$	-0.52×10^{-4}
3	$+0.43 \times 10^{-2}$	-0.99	-0.88×10^{-2}	-0.21×10^{-4}
1	-0.16×10^{-2}	$+0.19 \times 10^{-4}$	$+0.38 \times 10^{-4}$	-0.66×10^{-4}
2	$+0.87 \times 10^{-5}$	-0.64×10^{-2}	$+1.00$	$+0.13 \times 10^{-4}$
3	-0.67×10^{-2}	-1.01	-0.66×10^{-2}	$+0.17 \times 10^{-4}$

that limit closer. The reason is simple: by increasing the energy-scale of the bath, it is necessary to reduce the time step (or equivalently increase the number of terms in the Chebyshev polynomial expansion) in order to treat the fast oscillations properly. Keeping the same relaxation times roughly the same but taking a smaller time step requires more computation. For instance, it takes about 4 (20) h CPU time of 16384 BlueGene/Q processors to produce the TDSE data from which the numbers in Table B.1 (Table B.2) have been obtained.

Bibliography

[1] N. M. R. Peres, "*Colloquium* : The transport properties of graphene: An introduction," *Reviews of Modern Physics* **82** (Sep, 2010) 2673–2700.

[2] M. I. Katsnelson, *Graphene: Carbon in Two Dimensions*. Cambridge University Press, 2012.

[3] M. Orlita and M. Potemski, "Dirac electronic states in graphene systems: optical spectroscopy studies," *Semiconductor Science and Technology* **25** (2010) no. 6, 063001.

[4] Z. Li, E. A. Henriksen, Z. Jiang, Z. Hao, M. C. Martin, P. Kim, H. Stormer, and D. N. Basov, "Dirac charge dynamics in graphene by infrared spectroscopy," *Nature Physics* **4** (2008) no. 7, 532–535.

[5] C.-F. Chen, C.-H. Park, B. W. Boudouris, J. Horng, B. Geng, C. Girit, A. Zettl, M. F. Crommie, R. A. Segalman, S. G. Louie, and F. Wang, "Controlling inelastic light scattering quantum pathways in graphene," *Nature* **471** (2011) 617–620.

[6] T. Ando, Y. Zheng, and H. Suzuura, "Dynamical conductivity and zero-mode anomaly in honeycomb lattices," *Journal of the Physical Society of Japan* **71** (2002) no. 5, 1318–1324.

[7] A. Grüneis, R. Saito, G. G. Samsonidze, T. Kimura, M. A. Pimenta, A. Jorio, A. G. S. Filho, G. Dresselhaus, and M. S. Dresselhaus, "Inhomogeneous optical absorption around the K point in graphite and carbon nanotubes," *Physical Review B* **67** (Apr, 2003) 165402.

[8] N. M. R. Peres, F. Guinea, and A. H. Castro Neto, "Electronic properties of disordered two-dimensional carbon," *Physical Review B* **73** (Mar, 2006) 125411.

[9] V. P. Gusynin, S. G. Sharapov, and J. P. Carbotte, "Unusual microwave response of dirac quasiparticles in graphene," *Physical Review Letters* **96** (Jun, 2006) 256802.

[10] T. Stauber, N. M. R. Peres, and F. Guinea, "Electronic transport in graphene: A semiclassical approach including midgap states," *Physical Review B* **76** (Nov, 2007) 205423.

[11] V. P. Gusynin, S. G. Sharapov, and J. P. Carbotte, "Ac conductivity of graphene: from tight-binding model to 2+1-dimensional quantum electrodynamics," *International Journal of Modern Physics B* **21** (2007) 4611.

[12] T. Stauber, N. M. R. Peres, and A. K. Geim, "Optical conductivity of graphene in the visible region of the spectrum," *Physical Review B* **78** (Aug, 2008) 085432.

[13] T. Stauber, N. M. R. Peres, and A. H. Castro Neto, "Conductivity of suspended and non-suspended graphene at finite gate voltage," *Physical Review B* **78** (Aug, 2008) 085418.

[14] H. Min and A. H. MacDonald, "Origin of universal optical conductivity and optical stacking sequence identification in multilayer graphene," *Physical Review Letters* **103** (Aug, 2009) 067402.

[15] K. F. Mak, M. Y. Sfeir, Y. Wu, C. H. Lui, J. A. Misewich, and T. F. Heinz, "Measurement of the optical conductivity of graphene," *Physical Review Letters* **101** (Nov, 2008) 196405.

[16] S. Yuan, R. Roldán, H. De Raedt, and M. I. Katsnelson, "Optical conductivity of disordered graphene beyond the dirac cone approximation," *Physical Review B* **84** (Nov, 2011) 195418.

[17] R. Kubo, "Statistical-mechanical theory of irreversible processes. I.," *Journal of the Physical Society of Japan* **12** (1957) 570–586t.

[18] A. Redfield, "On the theory of relaxation processes," *IBM Journal of Research and Development* **1** (1957) 19–31.

[19] A. Abragam, *Principles of Nuclear Resonance*. Oxford Press, London, 1961.

[20] M. Nielsen and I. Chuang, *Quantum Computation and Quantum Information*. Cambridge University Press, Cambridge, 10th anniversary edition ed., 2010.

[21] M. W. Johnson, M. H. S. Amin, S. Gildert, T. Lanting, F. Hamze, N. Dickson, R. Harris, A. J. Berkley, J. Johansson, P. Bunyk, E. M. Chapple, C. Enderud, J. P. Hilton, K. Karimi, E. Ladizinsky, N. Ladizinsky, T. Oh, I. Perminov, C. Rich, M. C. Thom, E. Tolkacheva, C. J. S. Truncik, S. Uchaikin, J. Wang, B. Wilson, and G. Rose, "Quantum annealing with manufactured spins," *Nature* **473** (2011) 194–198.

[22] A. Hams and H. De Raedt, "Fast algorithm for finding the eigenvalue distribution of very large matrices," *Physical Review E* **62** (Sep, 2000) 4365–4377.

[23] R. Steinigeweg, F. Heidrich-Meisner, J. Gemmer, K. Michielsen, and H. De Raedt, "Scaling of diffusion constants in the spin-$\frac{1}{2}$ xx ladder," *Physical Review Letters* **90** (Sep, 2014) 094417.

[24] C. Bartsch and J. Gemmer, "Dynamical typicality of quantum expectation values," *Physical Review Letters* **102** (Mar, 2009) 110403.

[25] R. Steinigeweg, J. Gemmer, and W. Brenig, "Spin-current autocorrelations from single pure-state propagation," *Physical Review Letters* **112** (Mar, 2014) 120601.

[26] T. A. Elsayed and B. V. Fine, "Regression relation for pure quantum states and its implications for efficient computing," *Physical Review Letters* **110** (Feb, 2013) 070404.

[27] R. Steinigeweg, A. Khodja, H. Niemeyer, C. Gogolin, and J. Gemmer, "Pushing the limits of the eigenstate thermalization hypothesis towards mesoscopic quantum systems," *Physical Review Letters* **112** (2014) no. 13, 130403.

[28] F. Jin, H. De Raedt, S. Yuan, M. I. Katsnelson, S. Miyashita, and K. Michielsen, "Approach to equilibrium in nano-scale systems at finite temperature," *Journal of the Physical Society of Japan* **79** (2010) no. 12, 124005.

[29] T. Iitaka, S. Nomura, H. Hirayama, X. Zhao, Y. Aoyagi, and T. Sugano, "Calculating the linear response functions of noninteracting electrons with a time-dependent schrödinger equation," *Physical Review E* **56** (Jul, 1997) 1222–1229.

[30] T. Iitaka, "Correlation functions for a time-dependent calculation of linear-response functions," *Physical Review E* **56** (Dec, 1997) 7318–7319.

[31] T. Iitaka and T. Ebisuzaki, "Random phase vector for calculating the trace of a large matrix," *Physical Review E* **69** (May, 2004) 057701.

[32] H. Tal-Ezer and R. Kosloff, "An accurate and efficient scheme for propagating the time dependent schrdinger equation," *The Journal of Chemical Physics* **81** (1984) 3967–3971.

[33] C. Leforestier, R. H. Bisseling, C. Cerjan, M. D. Feit, R. Friesner, A. Guldberg, A. Hammerich, G. Jolicard, W. Karrlein, H.-D. Meyer,

N. Lipkin, O. Roncero, and R. Kosloff, "A comparison of different propagation schemes for the time dependent Schrödinger equation," *Journal of Computational Physics* **94** (1991) 59–80.

[34] T. Iitaka, S. Nomura, H. Hirayama, X. Zhao, Y. Aoyagi, and T. Sugano, "Calculating the linear response functions of noninteracting electrons with a time-dependent Schrödinger equation," *Physical Review E* **56** (1997) 1222–1229.

[35] V. V. Dobrovitski and H. De Raedt, "Efficient scheme for numerical simulations of the spin-bath decoherence," *Physical Review E* **67** (2003) 056702.

[36] H. De Raedt and K. Michielsen, "Computational Methods for Simulating Quantum Computers," in *Handbook of Theoretical and Computational Nanotechnology*, M. Rieth and W. Schommers, eds., pp. 2 – 48. American Scientific Publishers, Los Angeles, 2006.

[37] D. J. Griffiths, *Introduction to Quantum Mechanics*. Addison-Wesley Professional, 2004.

[38] K. Blum, *Density matrix theory and applications*, vol. 64. Springer Science & Business Media, 2012.

[39] R. C. Tolman, *The Principles of Statistical Mechanics*. Dover Publications; Revised ed. edition, 2010.

[40] H. De Raedt, "Product formula algorithms for solving the time dependent schrödinger equation," *Computer Physics Reports* **7** (1987) no. 1, 1–72.

[41] H. Tal-Ezer and R. Kosloff, "An accurate and efficient scheme for propagating the time dependent schrödinger equation," *The Journal of Chemical Physics* **81** (1984) no. 9, 3967–3971.

[42] M. Abramowitz, I. A. Stegun, *et al.*, *Handbook of mathematical functions*, vol. 1046. Dover New York, 1965.

[43] W. H. Press, *Numerical Recipes (3rd edition): The art of scientific computing*. Cambridge University Press, 2007.

[44] C. Leforestier, R. Bisseling, C. Cerjan, M. Feit, R. Friesner, A. Guldberg, A. Hammerich, G. Jolicard, W. Karrlein, H.-D. Meyer, *et al.*, "A comparison of different propagation schemes for the time dependent schrödinger equation," *Journal of Computational Physics* **94** (1991) no. 1, 59–80.

[45] H. De Raedt and A. Lagendijk, "Monte carlo simulation of quantum statistical lattice models," *Physics Reports* **127** (1985) no. 4, 233–307.

[46] H. De Raedt, "Computer simulation of quantum phenomena in nano-scale devices," *Annual Reviews of Computational Physics* **4** (1996) 107–146.

[47] K. Binder, D. P. Landau, D. W. Heermann, A. N. Burkitt, R. H. Swendsen, J.-S. Wang, A. M. Ferrenberg, H. J. Herrmann, D. Levesque, J. J. Weis, K. E. Schmidt, *et al.*, *The Monte Carlo method in condensed matter physics*, vol. 71. Springer Science & Business Media, 2012.

[48] M. Suzuki, "Generalized trotter's formula and systematic approximants of exponential operators and inner derivations with applications to many-body problems," *Communications in Mathematical Physics* **51** (1976) no. 2, 183–190.

[49] H. F. Trotter, "On the product of semi-groups of operators," *Proceedings of the American Mathematical Society* **10** (1959) no. 4, 545–551.

[50] M. Suzuki, "Decomposition formulas of exponential operators and lie exponentials with some applications to quantum mechanics and statistical physics," *Journal of Mathematical Physics* **26** (1985) no. 4, 601–612.

[51] M. Suzuki, "Transfer-matrix method and monte carlo simulation in quantum spin systems," *Physical Review B* **31** (Mar, 1985) 2957–2965.

[52] M. Suzuki, "General theory of fractal path integrals with applications to many-body theories and statistical physics," *Journal of Mathematical Physics* **32** (1991) no. 2, 400–407.

[53] H. Kobayashi, N. Hatano, and M. Suzuki, "Study of correction terms for higher-order decompositions of exponential operators," *Physica A: Statistical Mechanics and its Applications* **211** (1994) no. 2-3, 234–254.

[54] G. A. Baym, *Lectures on Quantum Mechanics*. Benjamin, 1969.

[55] P. A. M. Dirac, *Lectures on Quantum Mechanics*. Courier, 2013.

[56] L. E. Ballentine, *Quantum Mechanics: a modern development*. World Scientific, 1998.

[57] M. Suzuki, "Phenomenological theory of spin-glasses and some rigorous results," *Progress of Theoretical Physics* **58** (1977) no. 4, 1151–1165.

[58] P. de Vries and H. De Raedt, "Solution of the time-dependent schrödinger equation for two-dimensional spin-1/2 heisenberg systems," *Physical Review B* **47** (Apr, 1993) 7929–7937.

[59] R. Kubo, "Statistical-mechanical theory of irreversible processes. i. general theory and simple applications to magnetic and conduction problems," *Journal of the Physical Society of Japan* **12** (1957) no. 6, 570–586.

[60] D. Stirzaker, G. R. Grimmett, G. R. Grimmett, G. B. Statisticien, G. R. Grimmett, and G. B. Statistician, *Probability and random processes*. Clarendon Press, 1992.

[61] R. Alben, M. Blume, H. Krakauer, and L. Schwartz, "Exact results for a three-dimensional alloy with site diagonal disorder: comparison with the coherent potential approximation," *Physical Review B* **12** (Nov, 1975) 4090–4094.

[62] M. D. Feit, J. A. Fleck, and A. Steiger, "Solution of the schrödinger equation by a spectral method," *Journal of Computational Physics* **47** (1982) no. 3, 412–433.

[63] H. De Raedt and P. de Vries, "Simulation of two and three-dimensional disordered systems: Lifshitz tails and localization properties," *Zeitschrift für Physik B Condensed Matter* **77** (1989) no. 2, 243–251.

[64] T. Kawarabayashi and T. Ohtsuki, "Diffusion of electrons in two-dimensional disordered symplectic systems," *Physical Review B* **53** (Mar, 1996) 6975–6978.

[65] T. Ohtsuki and T. Kawarabayashi, "Anomalous diffusion at the anderson transitions," *Journal of the Physical Society of Japan* **66** (1997) no. 2, 314–317.

[66] S. Nomura, T. Iitaka, X. Zhao, T. Sugano, and Y. Aoyagi, "Linear scaling calculation for optical-absorption spectra of large hydrogenated silicon nanocrystallites," *Physical Review B* **56** (Aug, 1997) R4348–R4350.

[67] S. Nomura, T. Iitaka, X. Zhao, T. Sugano, and Y. Aoyagi, "Quantum-size effect in model nanocrystalline/amorphous mixed-phase silicon structures," *Physical Review B* **59** (Apr, 1999) 10309–10314.

[68] T. Iitaka and T. Ebisuzaki, "Efficient algorithm for calculating two-photon absorption spectra," *Physical Review E* **60** (Aug, 1999) R1178–R1180.

[69] T. Iitaka and T. Ebisuzaki, "Non-degenerate two photon absorption spectra of si nanocrystallites," *Microelectronic Engineering* **47** (1999) no. 1-4, 321–323.

[70] T. Iitaka and T. Ebisuzaki, "Calculating response functions in time domain with nonorthonormal basis sets," *Physical Review E* **61** (Apr, 2000) R3314–R3317.

[71] H. De Raedt, A. Hams, K. Michielsen, S. Miyashita, and K. Saito, "Quantum statistical mechanics on a quantum computer," *Progress of Theoretical Physics Supplement* **138** (2000) 489–494.

[72] D. S. Abrams and S. Lloyd, "Quantum algorithm providing exponential speed increase for finding eigenvalues and eigenvectors," *Physical Review Letters* **83** (Dec, 1999) 5162–5165.

[73] J. P. Hobson and W. A. Nierenberg, "The statistics of a two-dimensional, hexagonal net," *Physical Review* **89** (Feb, 1953) 662–662.

[74] E. Lieb, T. Schultz, and D. Mattis, "Two soluble models of an antiferromagnetic chain," *Annals of Physics* **16** (1961) no. 3, 407–466.

[75] A. Ishihara, *Statistical Physics.* Academic Press, New York, 1971.

[76] S. Yuan, H. De Raedt, and M. I. Katsnelson, "Modeling electronic structure and transport properties of graphene with resonant scattering centers," *Phys. Rev. B* **82** (Sep, 2010) 115448.

[77] A. Ishihara, *Statistical Physics.* Academic Press, New York, 1971.

[78] L. A. Falkovsky and S. S. Pershoguba, "Optical far-infrared properties of a graphene monolayer and multilayer," *Physical Review B* **76** (Oct, 2007) 153410.

[79] A. B. Kuzmenko, E. van Heumen, F. Carbone, and D. van der Marel, "Universal optical conductance of graphite," *Physical Review Letters* **100** (Mar, 2008) 117401.

[80] L. A. Ponomarenko, R. Yang, T. M. Mohiuddin, M. I. Katsnelson, K. S. Novoselov, S. V. Morozov, A. A. Zhukov, F. Schedin, E. W. Hill, and A. K. Geim, "Effect of a high-κ environment on charge carrier mobility in graphene," *Physical Review Letters* **102** (May, 2009) 206603.

[81] N. J. G. Couto, B. Sacépé, and A. F. Morpurgo, "Transport through graphene on srtio$_3$," *Physical Review Letters* **107** (Nov, 2011) 225501.

[82] M. I. Katsnelson and A. K. Geim, "Electron scattering on microscopic corrugations in graphene," *Philosophical Transactions of the Royal Society A* **366** (2008) no. 1863, 195–204.

[83] M. Gibertini, A. Tomadin, M. Polini, A. Fasolino, and M. I. Katsnelson, "Electron density distribution and screening in rippled graphene sheets," *Physical Review B* **81** (Mar, 2010) 125437.

[84] M. Gibertini, A. Tomadin, F. Guinea, M. I. Katsnelson, and M. Polini, "Electron-hole puddles in the absence of charged impurities," *Physical Review B* **85** (May, 2012) 201405.

[85] N. J. G. Couto, D. Costanzo, S. Engels, D.-K. Ki, K. Watanabe, T. Taniguchi, C. Stampfer, F. Guinea, and A. F. Morpurgo, "Random strain fluctuations as dominant disorder source for high-quality on-substrate graphene devices," *Physical Review X* **4** (Oct, 2014) 041019.

[86] M. A. H. Vozmediano, M. I. Katsnelson, and F. Guinea, "Gauge fields in graphene," *Physics Reports* **496** (2010) no. 4, 109–148.

[87] Z. Ni, L. Ponomarenko, R. Nair, R. Yang, S. Anissimova, I. Grigorieva, F. Schedin, P. Blake, Z. Shen, E. Hill, *et al.*, "On resonant scatterers as a factor limiting carrier mobility in graphene," *Nano Letters* **10** (2010) no. 10, 3868–3872.

[88] T. O. Wehling, S. Yuan, A. I. Lichtenstein, A. K. Geim, and M. I. Katsnelson, "Resonant scattering by realistic impurities in graphene," *Physical Review Letters* **105** (Jul, 2010) 056802.

[89] F. Wang, Y. Zhang, C. Tian, C. Girit, A. Zettl, M. Crommie, and Y. R. Shen, "Gate-variable optical transitions in graphene," *Science* **320** (2008) no. 5873, 206–209.

[90] A. H. Castro Neto, F. Guinea, N. M. R. Peres, K. S. Novoselov, and A. K. Geim, "The electronic properties of graphene," *Reviews of Modern Physics* **81** (Jan, 2009) 109–162.

[91] A. Kretinin, G. L. Yu, R. Jalil, Y. Cao, F. Withers, A. Mishchenko, M. I. Katsnelson, K. S. Novoselov, A. K. Geim, and F. Guinea, "Quantum capacitance measurements of electron-hole asymmetry and next-nearest-neighbor hopping in graphene," *Physical Review B* **88** (Oct, 2013) 165427.

[92] V. M. Pereira, J. Nilsson, and A. H. Castro Neto, "Coulomb impurity problem in graphene," *Physical Review Letters* **99** (Oct, 2007) 166802.

[93] J. P. Robinson, H. Schomerus, L. Oroszlány, and V. I. Fal'ko, "Adsorbate-limited conductivity of graphene," *Physical Review Letters* **101** (Nov, 2008) 196803.

[94] S. Yuan, H. De Raedt, and M. I. Katsnelson, "Modeling electronic structure and transport properties of graphene with resonant scattering centers," *Physical Review B* **82** (Sep, 2010) 115448.

[95] S. Yuan, T. O. Wehling, A. I. Lichtenstein, and M. I. Katsnelson, "Enhanced screening in chemically functionalized graphene," *Physical Review Letters* **109** (Oct, 2012) 156601.

[96] A. Cresti, F. Ortmann, T. Louvet, D. Van Tuan, and S. Roche, "Broken symmetries, zero-energy modes, and quantum transport in disordered graphene: From supermetallic to insulating regimes," *Physical Review Letters* **110** (May, 2013) 196601.

[97] G. Trambly de Laissardière and D. Mayou, "Conductivity of graphene with resonant and nonresonant adsorbates," *Physical Review Letters* **111** (Oct, 2013) 146601.

[98] G. Trambly de Laissardière and D. Mayou, "Conductivity of graphene with resonant adsorbates: beyond the nearest neighbor hopping model," *Advances in Natural Sciences: Nanoscience and Nanotechnology* **5** (2014) no. 1, 015007.

[99] V. M. Pereira, J. M. B. Lopes dos Santos, and A. H. Castro Neto, "Modeling disorder in graphene," *Physical Review B* **77** (Mar, 2008) 115109.

[100] W. Zhu and B. Lv, "Uncovering the dominant scattering mechanism in graphene system," *Physics Letters A* **377** (2013) no. 25, 1649–1654.

[101] Y.-W. Tan, Y. Zhang, K. Bolotin, Y. Zhao, S. Adam, E. H. Hwang, S. Das Sarma, H. L. Stormer, and P. Kim, "Measurement of scattering rate and minimum conductivity in graphene," *Physical Review Letters* **99** (Dec, 2007) 246803.

[102] J.-H. Chen, C. Jang, S. Adam, M. Fuhrer, E. Williams, and M. Ishigami, "Charged-impurity scattering in graphene," *Nature Physics* **4** (2008) no. 5, 377–381.

[103] A. K. Geim and K. S. Novoselov, "The rise of graphene," *Nature Materials* **6** (2007) no. 3, 183–191.

[104] F. Evers and A. D. Mirlin, "Anderson transitions," *Reviews of Modern Physics* **80** (Oct, 2008) 1355–1417.

[105] K. I. Bolotin, K. J. Sikes, J. Hone, H. L. Stormer, and P. Kim, "Temperature-dependent transport in suspended graphene," *Physical Review Letters* **101** (Aug, 2008) 096802.

[106] L. Ren, Q. Zhang, J. Yao, Z. Sun, R. Kaneko, Z. Yan, S. Nanot, Z. Jin, I. Kawayama, M. Tonouchi, *et al.*, "Terahertz and infrared spectroscopy of gated large-area graphene," *Nano Letters* **12** (2012) no. 7, 3711–3715.

[107] T. Fang, A. Konar, H. Xing, and D. Jena, "Carrier statistics and quantum capacitance of graphene sheets and ribbons," *Applied Physics Letters* **91** (2007) no. 9, 092109.

[108] J. Xia, F. Chen, J. Li, and N. Tao, "Measurement of the quantum capacitance of graphene," *Nature Nanotechnology* **4** (2009) 505.

[109] S. Dröscherscher, P. Roulleau, F. Molitor, P. Studerus, C. Stampfer, K. Ensslin, and T. Ihn, "Quantum capacitance and density of states of graphene," *Applied Physics Letters* **96** (2010) 152104.

[110] L. Wang, X. Chen, W. Zhu, Y. Wang, C. Zhu, Z. Wu, Y. Han, M. Zhang, W. Li, Y. He, and N. Wang, "Detection of resonant impurities in graphene by quantum capacitance measurement," *Physical Review B* **89** (Feb, 2014) 075410.

[111] S. Nakajima, "On quantum theory of transport phenomena," *Progress of Theoretical Physics* **20** (1958) 948 – 959.

[112] R. Zwanzig, "Ensemble method in the theory of irreversibility," *The Journal of Chemical Physics* **33** (1960) 1338 – 1341.

[113] H.-P. Breuer and F. Petruccione, *Open Quantum Systems.* Oxford University Press, Oxford, 2002.

[114] W. Pauli, *Festschrift zum 60. Geburtstage A. Sommerfelds.* Hirzel, Leipzig, 1928. p. 30.

[115] M. B. Plenio and P. L. Knight, "The quantum-jump approach to dissipative dynamics in quantum optics," *Reviews of Modern Physics* **70** (1998) 101–144.

[116] G. Lindblad, "On the generators of quantum dynamical semigroups," *Communications in Mathematical Physics* **48** (1976) 119–130.

[117] P. Gaspard and M. Nagaoka, "Slippage of initial conditions for the redfield master equation," *The Journal of Chemical Physics* **111** (1999) 5668 – 5675.

[118] W. Louisell, *Quantum Statistical Properties of Radiation.* Wiley, New York, 1973.

[119] C. Cohen-Tannoudji, J. Dupont-Roc, and G. Grynberg, *Atom-Photon Interactions.* Wiley, New York, 1992.

[120] Y. Hamano and F. Shibata, "Theory of exchange splitting in a strong magnetic field: I. General formulation," *Journal of Physics C: Solid State Physics* **17** (1984) 4843–4853.

[121] F. Shibata and M. Asou, "Theory of nonlinear spin relaxation. II," *Journal of the Physical Society of Japan* **49** (1980) 1234–1241.

[122] A. Suárez, R. Silbey, and I. Oppenheim, "Memory effects in the relaxation of quantum systems," *The Journal of Chemical Physics* **97** (1992) 5101 – 5107.

[123] P. Pechukas, "Reduced dynamics need not be completely positive," *Physical Review Letters* **73** (1994) 1060–1062.

[124] M. Sassetti and U. Weiss, "Correlation functions for dissipative two-state systems: Effects of the initial preparation," *Physical Review A* **41** (1990) 5383–5393.

[125] U. Weiss, *Quantum Dissipative Systems*. World Scientific, Singapore, 2 ed., 1999.

[126] Y. Tanimura, "Stochastic Liouville, Langevin, Fokker-Planck, and master equation approaches to quantum dissipative systems," *Journal of the Physical Society of Japan* **75** (2006) 082001–1–39.

[127] H.-P. Breuer, J. Gemmer, and M. Michel, "Non-Markovian quantum dynamics: Correlated projection superoperators and Hilbert space averaging," *Physical Review E* **73** (2006) 016139.

[128] T. Mori and S. Miyashita, "Dynamics of the density matrix in contact with a thermal bath and the quantum master equation," *Journal of the Physical Society of Japan* **77** (2008) 124005.

[129] M. Saeki, "Relaxation method and TCLE method of linear response in terms of thermo-field dynamics," *Physica A* **387** (2008) 1827–1850.

[130] C. Uchiyama, M. Aihara, M. Saeki, and S. Miyashita, "Master equation approach to line shape in dissipative systems," *Physical Review E* **80** (2009) 021128.

[131] T. Mori, "Natural correlation between a system and a thermal reservoir," *Physical Review A* **89** (2014) 040101(R).

[132] H.-B. Chen, N. Lambert, Y.-C. Cheng, Y.-N. Chen, and F. Nori, "Using non-Markovian measures to evaluate quantum master equations for photosynthesis," *Scientific Reports* **5** (2015) 12753.

[133] H. Wang, "Basis set approach to the quantum dissipative dynamics: Application of the multiconfiguration time-dependent Hartree method to the spin-boson problem," *The Journal of Chemical Physics* **113** (2000) 9948–9956.

[134] M. Nest and H.-D. Meyer, "Dissipative quantum dynamics of anharmonic oscillators with the multiconfiguration time-dependent Hartree method," *The Journal of Chemical Physics* **119** (2003) 24–33.

[135] D. Gelman and R. Kosloff, "Simulating dissipative phenomena with a random thermal phase wavefunctions, high temperature application of the surrogate Hamiltonian approach," *Chemical Physics Letters* **381** (2003) 129–138.

[136] D. Gelman, C. Koch, and R. Kosloff, "Dissipative quantum dynamics with the surrogate Hamiltonian approach. a comparison between spin and harmonic baths," *The Journal of Chemical Physics* **121** (2004) 661–671.

[137] G. Katz, D. Gelman, M. Ratner, and R. Kosloff, "Stochastic surrogate Hamiltonian," *The Journal of Chemical Physics* **129** (2008) 034108.

[138] K. De Raedt, K. Michielsen, H. De Raedt, B. Trieu, G. Arnold, M. Richter, T. Lippert, H. Watanabe, and N. Ito, "Massively parallel quantum computer simulator," *Comp. Phys. Comm.* **176** (2007) 121 – 136.

[139] J. Lages, V. V. Dobrovitski, M. I. Katsnelson, H. A. De Raedt, and B. N. Harmon, "Decoherence by a chaotic many-spin bath," *Physical Review E* **72** (2005) 026225.

[140] S. Yuan, M. Katsnelson, and H. De Raedt, "Origin of the canonical ensemble: Thermalization with decoherence," *Journal of the Physical Society of Japan* **78** (2009) 094003.

[141] F. Jin, H. De Raedt, S. Yuan, M. I. Katsnelson, S. Miyashita, and K. Michielsen, "Approach to Equilibrium in Nano-scale Systems at Finite Temperature," *Journal of the Physical Society of Japan* **79** (2010) 124005.

[142] S. Yuan, M. Katsnelson, and H. De Raedt, "Evolution of a quantum spin system to its ground state: Role of entanglement and interaction symmetry," *Physical Review A* **75** (2007) 052109.

[143] S. Yuan, M. Katsnelson, and H. De Raedt, "Decoherence by a spin thermal bath: Role of spin-spin interactions and initial state of the bath," *Physical Review B* **77** (2008) 184301.

[144] F. Jin, K. Michielsen, M. A. Novotny, , S. Miyashita, S. Yuan, and H. De Raedt, "Quantum decoherence scaling with bath size: Importance of dynamics, connectivity, and randomness," *Physical Review A* **87** (2013) 022117.

[145] M. A. Novotny, F. Jin, S. Yuan, S. Miyashita, H. De Raedt, and K. Michielsen, "Quantum decoherence and thermalization at finite temperatures within the canonical-thermal-state ensemble," *Physical Review A* **93** (2016) 032110.

[146] L. E. Ballentine, *Quantum Mechanics: A Modern Development*. World Scientific, Singapore, 2003.

[147] A. Hams and H. De Raedt, "Fast algorithm for finding the eigenvalue distribution of very large matrices," *Physical Review E* **62** (2000) 4365 – 4377.

[148] G. H. Golub and C. F. Van Loan, *Matrix Computations*. John Hopkins University Press, Baltimore, 1996.

[149] W. H. Press, B. P. Flannery, S. A. Teukolsky, and W. T. Vetterling, *Numerical Recipes*. Cambridge University Press, Cambridge, 2003.

[150] V. V. Dobrovitski, H. De Raedt, M. Katsnelson, and B. Harmon, "Quantum oscillations without quantum coherence," *Physical Review Letters* **90** (2003) 210401.

[151] F. Bloch, "Nuclear induction," *Physical Review* **70** (1946) 460–474.

[152] M. Suzuki, "Decomposition formulas of exponential operators and lie exponentials with some applications to quantum mechanics and statistical physics," *Journal of Mathematical Physics* **26** (1985) 601 – 612.

Summary

This thesis consists of three major parts. The first part focuses on the theory that is behind the simulation algorithms that are used in this thesis to study the quantum many-body dynamics. The Chebyshev polynomial algorithm and Suzuki-Trotter product formula algorithm to solve the time-dependent Schrödinger equation are explained in detail in Chapter 2. Chapter 3 and Chapter 4 introduce two different random state approaches to explore the properties of large quantum many-body systems, avoiding the prohibitive computational efforts to store and diagonalize huge matrices.

The simulation method is then applied to two different problems. In the second part of the thesis, the electronic transport and optical properties of graphene with different types of disorders are studied. The importance of the next-nearest-neighbor hopping in combination with resonant scatterers disorder is demonstrated. Based on these results, we propose that the different but characteristic features that appear in the calculated electronic transport and optical properties can be used as fingerprints to identify the dominant sources of disorder in graphene.

In the last part of the thesis, we numerically construct a Markovian quantum master equation, which takes the form of the Bloch equation, to describe the dynamics of a spin-1/2 particle interacting with thermal spin bath. In all cases the approximations used to derive a Bloch-type quantum master equation seem justified and it was found that the quantum master equation extracted from the solutions of the time-dependent Schrödinger equation describes these solutions rather well.

Samenvatting

Dit proefschrift bestaat uit drie grote delen. In het eerste deel wordt ingegaan op de theorie achter de simulatie algoritmen die gebruikt worden in dit proefschrift om de quantum dynamica van veeldeeltjes systemen te bestuderen. Het Chebyshev polynoom algoritme en de Suzuki-Trotter productformule algoritme voor het oplossen van de tijdsafhankelijke Schrödinger vergelijking wordt uitvoering behandeld in hoofdstuk 2. In hoofdstuk 3 en hoofdstuk 4 bespreken we twee verschillende methodes gebaseerd op willekeurig gekozen toestanden om de eigenschappen van grote quantum veeldeeltjes systemen te onderzoeken. Het voordeel van deze aanpak is dat het niet nodig is om enorm grote matrices te diagonalizeren zodat de problemen met bestaande computers toch behandeld kunnen worden.

De simulatiemethode wordt vervolgens op twee verschillende problemen losgelaten. In het tweede deel van het proefschrift worden de elektronische transport en optische eigenschappen van grafeen met verschillende soorten van wanorde bestudeerd. Het belang van naaste-naastebuur hoppen in combinatie met resonante verstrooiers wordt gedemonstreerd. Gebaseerd op deze resultaten stellen wij voor dat de verschillende maar karakteristieke kenmerken die verschijnen in de elektronische transport en optische eigenschappen gebruikt kunnen worden als vingerafdrukken voor de dominante bron van wanorde in grafeen.

In het laatste deel van het proefschrift construeren we numeriek een Markov quantum master vergelijking, die de vorm van de Bloch vergelijking aanneemt, om de dynamica van een spin-1/2 deeltje in interactie met een thermisch spinbad te beschrijven. In alle gevallen lijken de benaderingen die gebruikt worden om een Bloch-type quantum master vergelijking af te leiden gerechtvaardigd en blijkt de quantum master vergelijking de oplossing van de tijdsafhankelijke Schrödinger vergelijking vrij goed te beschrijven.

Publications

[1] P. Zhao, H. De Raedt, S. Miyashita, F. Jin, K. Michielsen,
Dynamics of open quantum spin systems: An assessment of the quantum master equation approach,
Physical Review E 94, 022126 (2016);

[2] C. Backets, B. M. Szydlowska, A. Harvey, S. Yuan, V. Vega-Mayoral, B. R. Davies, P.-L. Zhao, D. Hanlon, E. J.G. Santos, M. I Katsnelson, W. J. Blau, C. Gadermaier, J. N. Coleman,
Production of Highly Monolayer Enriched Dispersions of Liquid-Exfoliated Nanosheets by Liquid Cascade Centrifugation,
Acs Nano 10, 1589 (2016);

[3] G. J. Slotman, M. M. van Wijk, P.-L. Zhao, A. Fasolino, M. I. Katsnelson, S. Yuan,
Effect of Structural Relaxation on the Electronic Structure of Graphene on Hexagonal Boron Nitride,
Physical Review Letters 115, 186801 (2015);

[4] P.-L. Zhao, S. Yuan, M. I. Katsnelson, H. De Raedt,
Fingerprints of disorder source in graphene,
Physical Review B 92, 045437 (2015).

Acknowledgements

I received a lot of help and support from all the people around me during my four year PhD study. At the end of my PhD study, I would like to express my gratitude to all those who helped me and were there for me along the way.

First and foremost, I would like to express my deep sense of appreciation to my supervisor, Prof.dr. Hans De Raedt. I am grateful for your faith in my work, and for your excellent guidance and inspiration during my study. I would also like to thank Prof.dr. Shengjun Yuan and Dr. Fengping Jin. They have also been of immense help to me in my research project. I can never finish my PhD degree without their constant discussions and guidance.

Many thanks go to Prof.dr. Petra Rudolf, Prof.dr. Mikhail I. Katsnelson, Prof.dr. Kristel Michielsen, Prof.dr. S. Miyashita, Prof.dr. D.G. Stavenga, Prof.dr. H. Leertouwer, Prof.dr. Jianting Ye and Prof.dr. Yutao Pei. They offered me many discussions and supports in my research study. In addition, I thank my master supervisor, Prof.dr. Xi Chen, who shared with me many valuable opinions about what makes a qualified researcher. I would like to thank my colleagues and co-authors, Dr. Mutia Delina, Drs. H.C. Donker, Drs. N. Mol, Drs. Pascal Freyer, Drs. Guus Slotman, Drs. Edo van Veen, Dr. Jin Yu for the many beneficial discussions and help. Moreover, I thank Iris de Roo-Kwant and Annelien Blanksma for their dedicated care of my daily institute life.

I would like to thank my paranymphs, Lijuan Xing and Hylke C. Donker, for helping me take care of the preparations for the public defense ceremony. I also want to thank the assessment committee, Prof.dr. J.TH.M. De Hosson, Prof.dr. M. A. Novotny and Prof.dr. R.G.E. Timmermans for their careful reading and valuable comments. Moreover, I would like to acknowledge the financial support of China Scholarship Council that made this work possible.

There is a huge list of people that have made my life in Groningen enjoyable and full of good memory. In case I forget to mention some of them that will make me regret later, I will not try to list them individually. Saturday basketball group and Sunday soccer group enriched my life, though I were often absent. It is very

happy to play together with them. A group of friends that certainly deserve a special treatment. Jiquan Wu & Zhonghong Ma, Xiaoming Zhang & Ping Xu, Bin Chen, Pu Yang, Ling Liu, Zhiwei Zhou, Hengxu Song, Qi Liu, Peng Wang, Shengjie Xiao & Baiyu An, Jianjun Tang & Wangli Cheng, Jun Li & Hongyu Wang, Lei Liang & Juan Shan, Yanjun Li & Peipei Wu, Tao Zhang & Wenjun Wang, Yuanze Wang & Jingjing Deng, Zheng Zhang, Haojie Cao, Yanglei Yi, Linyang Li, Boqun Liu, Jing Wu, Jing Liu, Yu Sun, Jinfeng Shao, Xukai Zhang, Weiteng Guo, Rongjing Zhang, Gert, Jamo, Paul, Mehdi Sedighi, Jianming Lu, Qihong Chen, Honghua Fang & Jie Yang, Yi Zhang, Bin Jiang. I wish you all the best in future. Here, I want to express my appreciation to Lijuan. Meeting you was the best incident during my study in Groningen. I really enjoy all the time we spend together.

Finally, my deep and sincere gratitude to my family for their continuous and unparalleled love, help, and support. I am grateful to my sisters and brother for their contribution to our family. I am forever indebted to my parents for giving me the opportunities and experiences that have made me who I am. I have never taken any compliments to heart because deep down inside I know that all of them actually belong to you both. Thanks for everything, father and mother.

Groningen
February 2017